



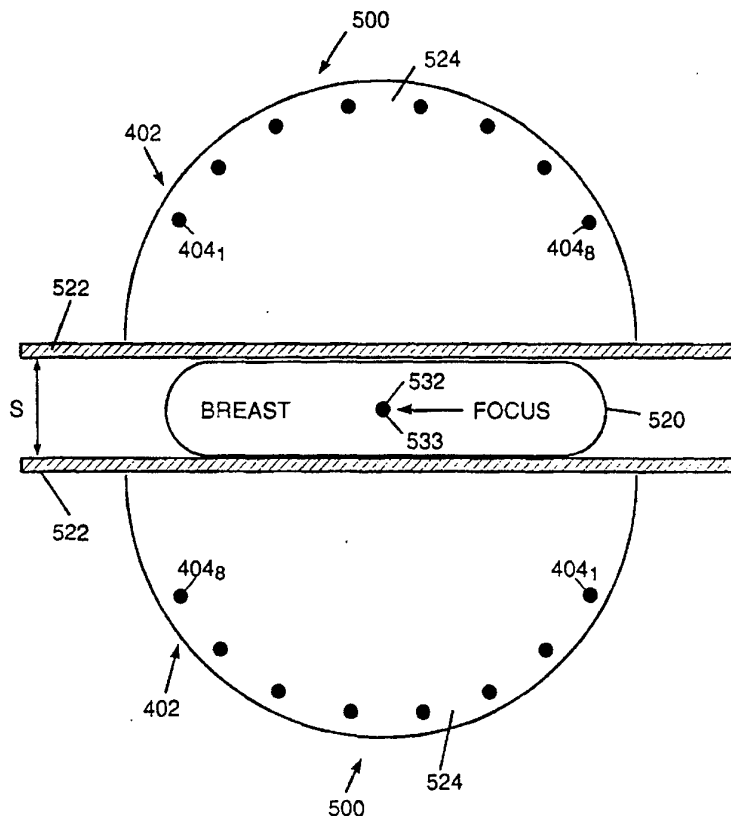
INTERNATIONAL APPLICATION PUBLISHED UNDER THE PATENT COOPERATION TREATY (PCT)

(51) International Patent Classification ⁶ : A61N 5/02	A1	(11) International Publication Number: WO 95/14505 (43) International Publication Date: 1 June 1995 (01.06.95)
(21) International Application Number: PCT/US94/13564 (22) International Filing Date: 22 November 1994 (22.11.94) (30) Priority Data: 08/157,928 24 November 1993 (24.11.93) US (71) Applicant: MASSACHUSETTS INSTITUTE OF TECHNOLOGY [US/US]; 77 Massachusetts Avenue, Cambridge, MA 02139 (US). (72) Inventor: FENN, Alan, J.; 4 Sherman Bridge Road, Wayland, MA 01778 (US). (74) Agent: SMITH, Richard, B.; Palmer & Dodge, One Beacon Street, Boston, MA 02108 (US).	(81) Designated States: CA, JP, European patent (AT, BE, CH, DE, DK, ES, FR, GB, GR, IE, IT, LU, MC, NL, PT, SE). Published <i>With international search report.</i> <i>Before the expiration of the time limit for amending the claims and to be republished in the event of the receipt of amendments.</i>	

(54) Title: MINIMALLY INVASIVE MONOPOLE PHASED ARRAY HYPERTHERMIA APPLICATORS FOR TREATING BREAST CARCINOMAS

(57) Abstract

An RF hyperthermia applicator for inducing a temperature rise in a human female breast for treating carcinomas includes a waveguide applicator having an aperture and a phased-array of monopole electric field radiators coupled to a source of electric field energy for producing electric field radiation output from the waveguide through the aperture. Compression means is used for compressing a human breast to a predetermined thickness. The waveguide is positioned adjacent to the compression means such that the breast is positioned adjacent to the aperture and thereby receives electric field radiation from the waveguide. In another embodiment, at least two waveguide applicators are positioned on opposite sides of the compression means so that the compressed breast is positioned between the opposed apertures of the waveguides. An electric field probe is placed into a target within the breast to assist in focusing the electric field energy into the target.



FOR THE PURPOSES OF INFORMATION ONLY

Codes used to identify States party to the PCT on the front pages of pamphlets publishing international applications under the PCT.

AT	Austria	GB	United Kingdom	MR	Mauritania
AU	Australia	GE	Georgia	MW	Malawi
BB	Barbados	GN	Guinea	NE	Niger
BE	Belgium	GR	Greece	NL	Netherlands
BF	Burkina Faso	HU	Hungary	NO	Norway
BG	Bulgaria	IE	Ireland	NZ	New Zealand
BJ	Benin	IT	Italy	PL	Poland
BR	Brazil	JP	Japan	PT	Portugal
BY	Belarus	KE	Kenya	RO	Romania
CA	Canada	KG	Kyrgyzstan	RU	Russian Federation
CF	Central African Republic	KP	Democratic People's Republic of Korea	SD	Sudan
CG	Congo	KR	Republic of Korea	SE	Sweden
CH	Switzerland	KZ	Kazakhstan	SI	Slovenia
CI	Côte d'Ivoire	LI	Liechtenstein	SK	Slovakia
CM	Cameroon	LV	Latvia	SN	Senegal
CN	China	LK	Sri Lanka	TD	Chad
CS	Czechoslovakia	LU	Luxembourg	TG	Togo
CZ	Czech Republic	LV	Latvia	TJ	Tajikistan
DE	Germany	MC	Monaco	TT	Trinidad and Tobago
DK	Denmark	MD	Republic of Moldova	UA	Ukraine
ES	Spain	MG	Madagascar	US	United States of America
FI	Finland	ML	Mali	UZ	Uzbekistan
FR	France	MN	Mongolia	VN	Viet Nam
GA	Gabon				

-1-

MINIMALLY INVASIVE MONOPOLE PHASED ARRAY HYPERTHERMIA
APPLICATORS FOR TREATING BREAST CARCINOMAS

BACKGROUND OF THE INVENTION

5 The successful treatment of deep-seated malignant tumors within a patient is often a difficult task. The objective of the treatment is to reduce in size or completely remove the tumor mass by one or more modalities available at the treatment facility. Common treatment
10 modalities are surgery, chemotherapy, and x-ray therapy. One treatment modality used alone or in conjunction with one of the above modalities is "tissue heating", or hyperthermia. Hyperthermia can be considered as a form of high fever localized within the body. A controlled
15 thermal dose distribution is required for hyperthermia to have a therapeutic value. Typical localized-hyperthermia temperatures required for therapeutic treatment of cancer are in the 43-45°C range. Normal tissue should be kept at temperatures below 43°C during the treatment. Typically,
20 hyperthermia is induced in the body by radio-frequency (RF) waves, acoustic (ultrasound) waves, or a combination of both. One of the most difficult aspects of implementing hyperthermia, with either RF or ultrasound waves, is producing sufficient heating at depth.

-2-

Multiple-appliator RF hyperthermia arrays are commonly used to provide a focused near-field main beam at the tumor position. Ideally, a focal region should be concentrated at the tumor site with minimal energy delivered to surrounding normal tissue.

In RF hyperthermia systems, the hyperthermia antenna beamwidth is proportional to the RF wavelength in the body. A small focal region suggests that the RF wavelength be as small as possible. However, due to propagation losses in tissue, the RF depth of penetration decreases with increasing transmit frequency. One of the major side-effects in heating a deep-seated tumor with a hyperthermia antenna is the formation of undesired "hot spots" in surrounding tissue. This additional undesired heating often produces pain, burns, and blistering in the patient, which requires terminating the treatment immediately. The patient does not receive anesthetics during the hyperthermia treatment in order to provide direct verbal feedback of any pain. Thus, techniques for reducing hot spots while maximizing energy delivered to the tumor site are desired in hyperthermia treatment.

RF hyperthermia systems with electric field transmitting arrays, i.e., antenna arrays, in the frequency band of 60-2000 MHz have been used to localize heating of malignant tumors within a target body. Phase control alone of the transmitting antennas of such an array has been used to synthesize therapeutic RF radiation patterns within a target body. Theoretical studies of adaptive control of individual antenna phase and power (transmit weights) has been used to maximize the tumor temperature (or RF power delivered to the tumor) while minimizing the surrounding tissue temperature (or RF power

-3-

delivered to the surrounding tissue). Invasive temperature measuring techniques have been used to optimize the radiation pattern within a target body.

One commercially available hyperthermia annular phased-array antenna system is the Model BSD-2000, SIGMA-60 applicator, available from BSD Medical Corporation, Salt Lake City, Utah. This phased-array system fully surrounds the patient, placing the patient at the center of an annular array of dipole transmit antennas. By fully surrounding the patient with an annular phased-array, it is possible to obtain constructive interference (or signal enhancement) deep within the target volume. This hyperthermia system uses a 60 cm array diameter with eight uniformly spaced dipole elements operating over the frequency band 60-120 MHz. The eight dipoles are fed as four active pairs of elements. There are four high-power amplifiers which drive the dipole pairs with up to 500 W average power per channel. Each of the four active channels has an electronically controlled variable-phase shifter for focusing the array. Temperature and electric-field probe sensors (both invasive and non-invasive) are used to monitor the treatment. A cool-water (5-40°C) bolus between the patient and the phased-array is used to prevent excess heating of the skin surface. The water bolus is filled with circulating distilled water, which has a very low propagation loss.

SUMMARY OF THE INVENTION

In accordance with the invention, adaptive nulling and/or focusing with non-invasive or minimally invasive auxiliary probes is used to reduce or enhance the field intensity at selected positions in and around the target

-4-

body while maintaining a desired focus at a tumor thereby avoiding or reducing the occurrences of "hot spots" while enhancing heating of the tumor during ultrasonic or R.F. hyperthermia treatment.

5 In general, in one aspect, the invention features a hyperthermia applicator for inducing a temperature rise in a human female breast for treating carcinomas including a waveguide applicator having an aperture and an electric field radiator coupled to a source of electric field
10 energy for producing electric field radiation output from the waveguide through the aperture. Compression means is used for compressing a human breast to a predetermined thickness. The waveguide is positioned adjacent to the compression means such that the breast is positioned
15 adjacent to the aperture and thereby receives electric field radiation from the waveguide. In another embodiment, at least two waveguide applicators are positioned on opposite sides of the compression means so that the compressed breast is positioned between the
20 opposed apertures of the waveguides.

 In some embodiments, the electric field radiator includes a phased-array of electric field transmit elements. The transmit elements can be monopole antenna elements. The waveguide applicator includes an RF
25 reflecting groundplane surface for mounting the monopole antenna elements, and another parallel RF reflecting groundplane surface positioned such that the monopole antenna elements are between the groundplanes. An RF reflecting screen is mounted perpendicular to the RF
30 groundplane surfaces and behind the monopole antenna elements to reflect RF energy from the monopole antenna elements toward the aperture of the waveguide. The RF

-5-

reflecting screen can be positioned between $1/8$ to $1/2$ wavelength from the monopole antenna elements. The waveguide includes an enclosure surrounding the monopole antenna elements providing a vessel for enclosing a bolus
5 of fluid between the monopole antenna elements and the breast. The vessel can contain a bolus of deionized water.

In other embodiments, the monopole antenna elements are arranged along a circular arc of substantially
10 constant radius. The radius can be substantially the distance from the monopole antenna array to the surface of the breast adjacent an internal target or substantially the distance from the monopole antenna array to a target within the breast. The monopole antenna elements can
15 resonate at between 800 and 1000 MHz.

In still other embodiments, the hyperthermia applicator includes at least one electric field probe for detecting electric field radiation, and a controller coupled to the electric field probe for receiving the
20 detected electric field radiation and controlling the source of electric field energy applied to each phased-array antenna transmit element. The electric field energy from the source is adjusted in response to the detected electric field radiation so that the detected electric
25 field radiation is maximized at the electric field probe. A probe element can be inserted invasively within the breast at the desired focus of the electric field energy. Mammography means can be used for imaging the internal structure of the breast for visualizing placement of the
30 probe element.

In general, in another aspect, the invention features a hyperthermia applicator having electric field radiators

-6-

each coupled to a source of electric radiation through a controllable transmit weighting network to control the phase and amplitude of the electric field radiation transmitted by each radiator. The transmit weighting
5 networks respond to feedback signals from a controller coupled to electric field probes which receive the electric field radiation from the radiators. The controller adjusts the feedback signals in response to the received electric field radiation so that the electric
10 field radiation is minimized at the electric field probes.

Preferred embodiments include a phased array of electric field radiators, and an annular array of electric field radiators for surrounding the target. The electric field probes include probes placed non-
15 invasively around the perimeter of the target where the electric field energy is to be minimized. In one embodiment, the target is modeled as an ellipse and the electric field probes are placed at the front, back, and on both sides of the ellipse.

20 In another aspect, the invention also features a secondary electric field probe, and the controller adjusts the feedback signals in response to the electric field radiation received by the secondary electric field probe so that the electric field radiation is maximized at the
25 secondary probe. Embodiments include placing the secondary probe at the desired focus of the electric field radiation.

In yet another aspect, the invention features the controller performing either a matrix inversion algorithm
30 or a gradient search algorithm to adjust the feedback signals controlling the transmit weighting networks in

-7-

response to the electric field energy received by the electric field probes.

In general, in another aspect, the invention features a hyperthermia applicator for heating a target inside a body, having electric field radiators each coupled to a source of electric radiation through a controllable transmit weighting network to control the phase and amplitude of the electric field radiation transmitted by each radiator. The transmit weighting networks respond to feedback signals from a controller coupled to electric field probes placed outside the body which receive the electric field radiation from the radiators. The controller adjusts the feedback signals in response to the electric field radiation received outside the body so that the electric field radiation is controlled at the target inside the body.

Preferred embodiments include a phased-array of electric field radiators, an annular array of electric field radiators for surrounding the target, and an array of monopole antenna elements for positioning nearby the target.

In preferred embodiments of the monopole array, the monopole antenna elements are perpendicularly mounted to one side of an RF reflecting groundplane. An RF reflecting screen is mounted perpendicular to the groundplane surface behind the monopole antenna elements to reflect RF energy from the monopole antenna elements toward the target. The ground plane includes an aperture for positioning the target on the same side of the ground plane as the monopole antenna elements. An enclosure surrounds the monopole antenna elements and provides a vessel for enclosing a bolus of fluid, such as deionized

-8-

water, between the monopole antenna elements and the body. In other preferred embodiments another ground plane is provided above the monopole antenna elements to form a waveguide between the antenna elements and the target
5 body. Further, multiple waveguides and monopole antenna arrays can be stacked.

In other preferred embodiments of the monopole array, the monopole array antenna elements resonate between 800 and 1000 MHz and are arranged in a circular arc having a
10 radius of between 5 and 20 cm. The body is a cranium and the target is a brain tumor. The radius of the monopole array circular arc is either the distance from the monopole antenna array to the center of the cranium, or to the target tumor.

15 In still other preferred embodiments, the electric field probes are non-invasively placed along the perimeter of the body between the elements of the phased-array and the target. The controller adjusts the feedback signal, with a gradient search or matrix inversion algorithm, to
20 minimize the difference in the electric field detected by adjacent electric field probes and thereby provide uniform electric field radiation into the body.

In yet other preferred embodiments, the electric field probes are formed into an array non-invasively
25 placed between the phased array and the target. The controller adjusts the feedback signal, with a gradient search or matrix inversion algorithm, to provide a particular electric field pattern across the electric field probe array and thereby focus radiation into the
30 target. The electric field probe array elements are placed symmetrically with respect to a bisector line which runs from the target to the phased array to bisect the

-9-

phased array. The controller adjusts the feedback signal to balance the electric field pattern with respect to the bisector line, and to minimize the difference in the electric field detected along the bisector line.

5 Thus, the present invention offers the advantages of allowing effective hyperthermia treatment to be applied to deep-seated tumors within the body while reducing or eliminating hot-spot formation on the surface of the body which interferes with the treatment. Another advantage is
10 that hot spots are eliminated quickly by sensing and adjusting the E-field radiation in the vicinity of the expected hot spot rather than by measuring the temperature rise of the tissue after heating has already occurred. Still another advantage is that the E-field sensing probes
15 may be located on the surface of the target rather than having to be invasively placed within the target body. A further advantage is that the E-field radiation can be focused on a target inside a body using E-field sensing probes non-invasively placed outside the body to maximize
20 heating of the target tissue.

BRIEF DESCRIPTION OF THE DRAWINGS

The foregoing and other objects, features and advantages of the invention will be apparent from the following more particular description of preferred
25 embodiments of the invention, as illustrated in the accompanying drawings in which like reference characters refer to the same parts throughout different views. The drawings are not necessarily to scale, emphasis instead being placed upon illustrating the principles of the
30 invention.

-10-

FIG. 1 is a perspective view of an RF annular array hyperthermia system featuring the adaptive nulling of this invention.

FIG. 2 is a cross-sectional representation of the
5 annular array of FIG. 1.

FIG. 3 is an analytical model of the cross-sectional representation of FIG. 2.

FIG. 4 is a simulated thermal profile of the
analytical model of FIG. 3 without the adaptive nulling of
10 this invention.

FIG. 5 is a simulated thermal profile of the
analytical model of FIG. 3 with the adaptive nulling of
this invention.

FIG. 6 is a schematic diagram of the adaptive
15 hyperthermia array and array controller of FIG. 1.

FIG. 7 is a schematic diagram of an analytical model
of an adaptive array for simulating the hyperthermia array
of FIG. 1.

FIG. 8 is a block diagram detailing the sample matrix
20 inversion algorithm derived from the adaptive hyperthermia
array model of FIG. 7.

FIG. 9 is a block diagram of the sample matrix
inversion algorithm performed by the hyperthermia array
controller of FIG. 6.

FIG. 10 is a scatter diagram of transmit weights used
25 in deriving the gradient search adaptive hyperthermia
algorithm.

FIG. 11 is a diagram showing the derivation of the
gradient search directions.

FIG. 12 is a block diagram of the gradient search
30 performed by the hyperthermia array controller of FIG. 6.

-11-

FIG. 13 is a schematic diagram of the analytical model of FIG. 7 redrawn to simplify derivation of method of moments analysis.

FIG. 14 is a schematic diagram of an equivalent
5 circuit model for simulating an auxiliary probe.

FIG. 15 is a schematic diagram of a thermal conductivity model for simulating hyperthermia heating within a target.

FIG. 16(a) is a block diagram detailing the
10 simulation model of the hyperthermia array of FIG. 1.

FIG. 16(b) is a table of values used in the simulation model of FIG. 16(a).

FIG. 17 is a schematic diagram of the transmit antenna array and auxiliary probe array geometries for the
15 simulation model of FIG. 16(a).

FIG. 18 is a diagram of the simulated E-field for the simulation model of FIG. 16(a) prior to adaptive nulling.

FIG. 19 is a diagram of the simulated profile in 1 dB steps for the E-field of FIG. 18.

FIGS. 20 and 21 are diagrams of the simulated E-field
20 profile of FIG. 19 taken along the x- and z- axes, respectively.

FIG. 22 is a diagram of the simulated E-field for the simulation model of FIG. 16(a) after adaptive nulling.

FIGS. 23 and 24 are diagrams of the simulated E-field
25 of FIGS. 18 and 22 taken along the x- and z- axes, respectively.

FIG. 25(a) is a diagram of the simulated E-field before and after adaptive nulling taken longitudinally in
30 the y direction along the x=15, z=0 cm line of the geometry shown in FIG. 25(b).

-12-

FIG. 26(a) is a diagram of the simulated E-field before and after adaptive nulling taken longitudinally along the y axis ($x=0$, $z=0$ cm) of the geometry shown in FIG. 26(b).

5 FIGS. 27(a) and 27(b) are graphs showing the transmit weight amplitude and phase, respectively, before and after adaptive nulling.

FIG. 28 is a graph showing the channel correlation matrix eigenvalues.

10 FIG. 29 is a diagram of the simulated target temperature profile for the E-field of FIG. 18 prior to adaptive nulling.

FIGS. 30 and 31 are diagrams of the temperature profile of FIG. 29 taken along the x- and z- axes, respectively.

15 FIG. 32 is a diagram of the simulated target temperature profile for the E-field of FIG. 22 after adaptive nulling.

FIGS. 33 and 34 are diagrams of the temperature profile of FIGS. 29 and 32 taken along the x- and z- axes, respectively.

FIG. 35 is a diagram of the simulated target temperature profile for the E-field of FIG. 18 prior to adaptive nulling.

25 FIG. 36 is a diagram of the simulated target temperature profile for the E-field of FIG. 22 after adaptive nulling.

FIGS. 37 and 38 are diagrams of the temperature profile of FIG. 36 taken along the x- and z- axis, respectively.

30 FIG. 39 is a cross-sectional view of an annular phased array hyperthermia system and saline phantom used

-13-

for gathering experimental adaptive nulling and focusing data.

FIG. 40 is a diagram of the E-field amplitude measured at a single null site, the tumor site, and a reference site, versus gradient search iteration for the experimental hyperthermia system and phantom of FIG. 39.

FIG. 41 is a diagram of the simulated E-field power versus gradient search iteration at the single null site of FIG. 40.

FIG. 42 is a cross-sectional view of a beef phantom used in place of the saline phantom in the experimental system of FIG. 39.

FIG. 43 is a diagram of the E-field amplitude measured at a single null site, the tumor site, and a reference site, versus gradient search iteration for the experimental hyperthermia system of FIG. 39 using the beef phantom of FIG. 42.

FIG. 44 is a diagram of the measured temperature versus time at the beef phantom tumor site and the single null site of FIG. 42.

FIG. 45 is a diagram of the E-field amplitude measured at two null sites and the tumor site, versus gradient search iteration for the experimental hyperthermia system and phantom of FIG. 39.

FIG. 46 is a diagram of the E-field amplitude measured at a focus on the surface of the saline phantom versus gradient search iteration for the experimental hyperthermia system and phantom of FIG. 39.

FIG. 47 is a perspective view of an RF monopole array hyperthermia system for treating brain tumors, featuring the adaptive focusing of this invention.

-14-

FIG. 48 is a top-view of the monopole phased array hyperthermia system of FIG. 47

FIG. 49 is a cross-sectional side view of the RF monopole phased array hyperthermia system of FIG. 47.

5 FIG. 50 is a schematic diagram of the monopole phased array hyperthermia system of FIG. 47 and an array controller.

FIG. 51 is a schematic diagram of the monopole phased array geometries for the hyperthermia system of FIG. 47.

10 FIG. 52 is a schematic diagram of the monopole phased array and electric field probe array geometries for the hyperthermia system of FIG. 47.

FIG. 53 is a diagram of a simulated E-field pattern for the monopole phased array geometry of FIG. 52.

15 FIG. 54 is a diagram of the simulated E-field pattern of FIG. 53 taken parallel to the x- axis along the line $z=5.08$ cm.

FIG. 55 is a diagram of the simulated temperature profile for the simulated E-field pattern of FIG. 53.

20 FIG. 56 is a schematic diagram of the monopole phased array hyperthermia system of FIG. 47 with an electric field probe array for generating uniform RF illumination over a large area of a target.

FIG. 57 show the monopole phased array system of FIG. 48 including the addition of a top ground plane surface forming a parallel plate waveguide.

FIGS. 58A shows a cross-sectional view of the wave guide of FIG. 57.

30 FIG. 58B shows a cross-sectional view of an alternative embodiment of the waveguide of FIG. 58A having diverging surfaces.

-15-

FIG. 58C shows a cross-sectional view of another alternative embodiment of the waveguide of FIG. 58A having flared surfaces forming a horn.

FIG. 59 shows a cross-sectional view of another alternative embodiment of the waveguide of FIG. 58A having multiple stacked monopole phased array antennas and associated stacked waveguides.

FIG. 60 is a block diagram of a microwave transmit and receive module for use with the monopole phased array system of FIG. 47.

Figs. 61-63 show an embodiment of a non-invasive RF monopole phased array hyperthermia waveguide applicator for treating malignant breast tumors.

Fig. 64 shows the use of two opposed applicators of Figs. 61-63 to irradiate breast tissue to produce hyperthermia during treatment.

Fig. 65 shows a breast tissue phantom used for measuring radiation patterns generated by the two opposed hyperthermia applicators of Fig. 64 positioned on opposite sides of the breast phantom in a mirrored configuration.

Fig. 66 shows RF energy contours (two dimensional electric field pattern) for the breast phantom of Fig. 65 as determined by an ideal computer simulation based on ray tracing.

Fig. 67 shows measured data taken along the Y axis through the breast phantom of Fig. 65, and its relationship to simulated data calculated by computer along the same axis, shown in Fig. 66.

Figs. 68 and 69 are simulated radiation patterns which show that radiation can be focused at positions within the breast tissue offset from the center of the opposed monopole array.

-16-

Figs. 70 and 71 are simulated radiation patterns which show that a single monopole array applicator can also be used to effectively focus radiation into the target.

5 DETAILED DESCRIPTION OF THE PREFERRED EMBODIMENT

Apparatus

Referring to FIG. 1, there is shown a hyperthermia annular phased-array system 100 having improved "hot spot" characteristics achieved by utilizing the focused near-
10 field adaptive nulling apparatus of this invention. An annular hyperthermia phased-array applicator 102, energized by a hyperthermia array controller 101, has a plurality of dipole transmit antenna elements 104 placed around a patient to be treated, or target body 106. The
15 dipole antenna elements are uniformly disposed around the patient. Each dipole antenna element is oriented parallel to the other dipole antennas and parallel to a longitudinal axis A-A passing through the center of a cylinder defined by applicator 102. The patient is
20 positioned within the hyperthermia phased array applicator 102 such that the deep-seated tumor to be treated 107 is at the approximate center, or focus, of the phased array applicator. A water-bolus 105 is provided between the patient and the phased array applicator to control the
25 temperature of the patient's skin. Phased-array applicator 102 therapeutically illuminates the target body 106 with electric field (E-field) energy radiated by dipole antenna elements 104 focused on tumor 107 deep within the body.

30 An example of a deep-seated tumor is cancer of the prostate. The tumor volume often has a decreased blood flow which aids in heating the tumor, compared to normal

-17-

tissue for which heat is carried away by normal blood flow. In practice, undesired high-temperature regions away from the focus can also occur on the skin and inside the volume of the target body. For example, scar tissue, which has a decreased blood flow rate, will tend to heat up more rapidly than normal tissue having normal blood flow.

In the adaptive hyperthermia array of this invention, electric-field nulls are used to reduce the power delivered to potential hot spots. Computer simulations, described herein, establish that non-invasive field probes, or sensors, 112 placed on the surface of the target can be used to eliminate hot spots interior to the target tissue. With the adaptive hyperthermia phased-array described herein, RF energy nulls are adaptively formed to reduce the electric field energy delivered to these potential hot spots. As will be shown, the energy nulls achieved by the adaptive nulling apparatus of this invention are both invasive to the target, i.e., extend into the target body, and non-invasive to the target, i.e., on the surface of the target.

Referring to FIG. 2, there is shown a schematic cross-sectional representation of an embodiment of an eight-element hyperthermia phased-array applicator 102 of FIG. 1. Phased-array applicator 102 has transmit antennas 104₁ through 104₈, arranged symmetrically surrounding a human body target 106' at the prostate level.

An analytical model of the embodiment of FIG. 2 is shown in FIG. 3. Here, an elliptical phantom target 106 is used to model the prostate-level cross section of the human body 106'. The center 107 of the elliptical phantom models the location of the prostate tumor to receive

-18-

hyperthermia treatment, i.e., the focus of RF energy for the phased array applicator 102. Water bolus 105 is assumed to surround the target body 106, and is treated as a homogeneous medium for analysis purposes.

5 Four auxiliary RF E-field probes, or sensors, 112₁ through 112₄, i.e., receiving antennas, are placed around the perimeter of the target to model non-invasive probes placed on the skin of the human body target. Each auxiliary probe 112₁ through 112₄ has a corresponding null
10 zone 120₁ through 120₄, respectively, centered at each auxiliary probe and extending into the elliptical target region 106. Each null zone indicates an area in which undesired "hot spots" are reduced or eliminated. The width of each null zone is directly related to the
15 strength of each null. The strength of each null (sometimes referred to as the amount of cancellation) is directly related to the signal-to-noise ratio at the probe position (SNR_p). A low SNR_p indicates a large amount of nulling (strong null), and a high SNR_p indicates a small
20 amount of nulling (weak null). The resolution, or minimum spacing, between the focus 107 and any null position is normally equal to the half-power beamwidth of the transmit antenna. Resolution may be enhanced somewhat by using weak nulls whenever the separation between the null and
25 focus is closer than the half-power beamwidth.

Referring to FIG. 4, there is shown the results of a simulation of the thermal distribution inside the target body 106 for the hyperthermia ring array applicator 102 of the analytical model of FIG. 3, without adaptive nulling,
30 transmitting into the target body. For simulation purposes, target body 106 is assumed to be a homogeneous elliptical region, and the RF energy from the array is

-19-

focused at the center of the ellipse 107, simulating the tumor site. No adaptive nulling is used. The contour lines of the thermal distribution represent isotherms having the indicated temperature in degrees Celsius ($^{\circ}\text{C}$), and are spaced at 2°C intervals. The simulation shows that the focus is expected to have a temperature of approximately 46°C , while two undesired "hot spots" 122 and 124 to the left and right of the focus, respectively, are expected to have temperatures of approximately 42°C .

FIG. 5 shows a simulated thermal distribution for the model of FIG. 3 where the adaptive nulling methods of this invention are applied. Comparison of FIG. 5 with FIG. 4 show that the "hot spots" 122 and 124 are essentially eliminated, no new "hot spots" have been produced within the target body, and the peak temperature induced at the focus is still approximately 46°C .

Referring to FIG. 6, a generalized schematic of the non-invasive adaptive-nulling hyperthermia system of FIG. 3 includes hyperthermia transmitting phased array applicator 102 having a plurality of transmitting antenna elements 104_n , where $n=1, \dots, N$, surrounding target body 106 for focusing RF energy at focus 107 within the target body. Phased array applicator 102 is energized by an RF energy source 108 which is distributed to and drives each transmit antenna element 104_n through a corresponding transmit weighting function 110_n , each having a corresponding weight w_n . Each weighting function w_n may affect the gain and phase of the RF energy fed to its corresponding antenna 104_n in the array, i.e., w_n represents a complex weighting function. Each weighting function 110_n may be implemented by a voltage controlled RF amplifier and a voltage controlled RF phase shifter.

-20-

An amplitude control voltage representing the amplitude component of transmit weight w_n is fed to the voltage controlled amplifier, and a phase control voltage representing the phase of transmit weight w_n is fed to the voltage controlled phase shifter.

Target body 106 has a plurality of E-field auxiliary probes 112_m , where $m=1, \dots, N_{aux}$, i.e., receiving antennas, positioned at various locations on the surface of the body for sampling the E-field at each particular location.

Another receiving probe 115 may be placed at the desired focus 107 of the array.

Receiving probes 112_m and 115 each drive an input to an RF receiver 114. The transmit amplitude and phase weights of each weighting function w_n are fed to the receiver 114 through lines 103_n and are used to find the transmit level of each transmit element 104_n . The outputs of receiver 114 represent the auxiliary probe-received complex voltages $v_1, v_2, \dots, v_{N_{aux}}$, the focus probe-received complex voltage v_F , and the transmit level of the phased array. The receiver outputs drive the inputs of a signal processor 116, which applies a nulling algorithm to adjust the weighting functions w_n and thereby null, or minimize, the RF signal received by each receiving probe 112_m , i.e., minimize the SNR_p at each probe.

To generate the desired field distribution in a clinical adaptive hyperthermia system, the receiving probes are positioned as close as possible to the focus (tumor site) and to where high temperatures are to be avoided (such as near the spinal cord and scar tissue).

For an annular array configuration the receiving probes can be located non-invasively on the surface (skin) of the target. Initially, the hyperthermia array is focused to

-21-

produce the required field intensity at the tumor. An invasive probe may be used to achieve the optimum focus at depth. To avoid undesired hot spots, it is necessary to minimize the power received at the desired null positions and to constrain the array transmit weights w_n to deliver a required amount of transmitted or focal region power.

Signal processor 116 performs either a sample matrix inversion (SMI) algorithm or a gradient search algorithm on the signals output from receiver 114 and updates the adaptive array weights w_n (with gain g and phase ϕ) to rapidly (within seconds) form the nulls at the auxiliary probes before a significant amount of target heating takes place. With this adaptive system, it is possible to avoid unintentional hot spots in the proximity of the auxiliary probes and maintain a therapeutic thermal dose distribution at the focus (tumor).

Signal processor 116 may also perform a maximizing algorithm to maximize energy at the focus 107. The focus probe 115 is invasively placed at the desired focus 107, and used to generate a maximum signal, or signal-to-noise ratio (SNR_F), at the tumor site. RF receiver 114 makes an amplitude and phase measurement on the output signal from invasive probe 115 for each transmit antenna element 104_n radiating one at a time. Signal processor 116 processes these measurements and feeds back weight command signals to the transmit weighting functions 110_n to calibrate or phase align the transmit channels to thereby maximize the SNR_F , or RF power, at the invasive focal point probe. If receiver 114 makes amplitude-only measurements from invasive focus probe 115, then a gradient search technique may be applied by the signal processor with all elements

-22-

transmitting simultaneously to maximize the SNR_F at the invasive focal point probe.

Theoretical Formulation of Nulling Algorithms

FIG. 7 shows an analytical model of a hyperthermia
5 phased-array antenna system 200, paralleling the
generalized hyperthermia phased-array antenna system 100
of FIG. 6, illustrating the principles of the near-field
adaptive nulling technique of this invention. The phased-
array antenna system 200 includes a hyperthermia
10 transmitting antenna array 202 having a plurality of
transmitting antennas 204_n , where $n=1, \dots, N$ for focusing
RF energy at a desired focus 207 in the near field of the
antenna. Antenna array 202 is energized by an RF energy
source 208 which drives a power divider 209. Power
15 divider 209 has one output for driving each antenna 204_n a
corresponding transmit weighting function 210_n , each
having a corresponding transmit weight w_n . It is assumed
here that each weighting function w_n may affect the phase
of the RF energy fed to its corresponding antenna 204_n in
20 the array. A calibration E-field probe 212, or focus
probe antenna, is positioned at focus 207 for sampling the
E-field at that location.

It is assumed that the hyperthermia phased-array
antenna 200 is focused (as it normally is) in the near
25 field and that a main beam 220 and possibly sidelobes 222
are formed in the target. In general, phase and amplitude
focusing is possible. It is assumed that phase focusing
alone is used to produce the desired quiescent main beam,
i.e., weighting functions w_n affects only the phase of the
30 RF signal driving each antenna. The signal received by
the calibration probe can be maximized by adjusting the
phase weighting functions w_n so that the observed transmit

-23-

antenna element-to-element phase variation is removed, i.e., all transmit antennas appear to be in-phase when observed from the focus.

One way to achieve phase coherence at the focus in a numerical simulation is to choose a reference path length as the distance from the focus to the phase center 224 of the array. This distance is denoted r_F and the distance from the focus to the n th array transmit antenna element is denoted r_n^F . The voltage received at the calibration probe 212 (located at focus 207) due to the n th array element may be computed using the "method of moments", as described below. To maximize the received voltage at the calibration probe output, it is necessary to apply the phase conjugate of the signal observed at the calibration probe, due to each array transmit antenna element, to the corresponding element at the transmit array. The resulting near-field radiation pattern will have a main beam and sidelobes. The main beam will be pointed at the array focal point, and sidelobes will exist at angles away from the main beam. Auxiliary probes can then be placed at the desired null positions in the quiescent sidelobe region. These sidelobes occur where tissue hot spots are likely to occur, and they are nulled by one of the adaptive nulling algorithms described below.

25 Adaptive Transmit Array Formulation

Considering again the hyperthermia array and probe geometry shown in FIG. 7, the hyperthermia transmit antenna array 202 typically contains N identical transmit antenna elements 204. The number of adaptive channels is denoted M , and for a fully adaptive array $M=N$. The ideal transmit weights w_n (a complex voltage gain vector) are assumed in the computer simulation, with $w =$

-24-

$(w_1, w_2, \dots, w_N)^T$ denoting the adaptive channel weight vector as shown in FIG. 6. (Superscript T means transpose). To generate adaptive nulls, the transmit weights (phase and gain) are controlled by either the Sample Matrix Inversion (SMI) algorithm or a gradient search algorithm. The SMI algorithm has the flexibility to operate in either open- or closed-loop feedback modes; the gradient search algorithm operates only in a feedback mode.

Sample Matrix Inversion (SMI) Algorithm

For the SMI algorithm, the fundamental quantities required to fully characterize the incident field for adaptive nulling purposes are the adaptive channel cross correlations. To implement this algorithm it is necessary to know the complex received voltage at each of the auxiliary probes. For example, the moment-method formulation (described below) allows computation of complex-received voltage at each of the auxiliary probes.

FIG. 8 is a block diagram showing the SMI algorithm applied to the adaptive hyperthermia phased-array of FIG. 7, and the derivation of performance measures to quantify computer simulation results. Four performance measures are used to quantify the computer simulations: electric-field distribution $E(x, y, z)$, channel correlation matrix eigenvalues λ_k , $k=1, \dots, N$, adaptive transmit weights w_a , and interference cancellation C . The calculation of these performance measures is described in detail below.

Assuming a spherical wavefront is incident at an i th probe antenna due to each of the N array transmit antenna elements (radiating one at a time with a unity-amplitude reference signal), the result is a set of probe-received complex voltages denoted $v_1^i, v_2^i, \dots, v_N^i$

-25-

after a gain adjustment 250. The cross correlation R_{mn}^i of the received voltages due to the m th and n th transmit antenna (adaptive transmit channel) at the i th probe is given by

$$R_{mn}^i = E(v_m v_n^*) \quad , \quad (1)$$

5 where $*$ means complex conjugate and $E(\cdot)$ means mathematical expectation. (Note: for convenience, in Equation (1) the superscript i in v_m and in v_n has been omitted.) Because v_m and v_n represent voltages of the same waveform but at different times, R_{mn}^i is also referred
10 to as an autocorrelation function.

In the frequency domain, assuming the transmit waveform has a band-limited white noise power spectral density (as commonly assumed in radar system analysis), Equation (1) can be expressed as the frequency average

$$R_{mn}^i = \frac{1}{B} \int_{f_1}^{f_2} v_m(f) v_n^*(f) df \quad , \quad (2)$$

15 where $B = f_2 - f_1$ is the nulling bandwidth, or bandwidth of frequencies applied by the hyperthermia treatment, and f is the transmit frequency of the hyperthermia array. It should be noted that $v_m(f)$ takes into account the transmit wavefront shape, which is spherical for the hyperthermia
20 application. For the special case of a continuous wave (CW) transmit waveform, as normally used in hyperthermia, the cross correlation reduces to

-26-

$$R_{mn}^i = v_m(f_o) v_n^*(f_o) \quad (3)$$

where f_o is the transmit frequency of the hyperthermia array.

Next, the channel correlation matrix, or interference covariance matrix, denoted R is determined 252. (Note: in
 5 hyperthermia, interference is used to refer to the signals received at the auxiliary probes. The undesired "hot spots" can be thought of as interfering with the therapy.) If there are N_{aux} independent desired null positions or auxiliary probes, the N_{aux} -probe channel correlation matrix
 10 is the sum of the channel correlation matrices observed at the individual probes. That is,

$$R = \sum_{i=1}^{N_{aux}} R_i + I \quad , \quad (4)$$

where R_i is the sample channel correlation matrix observed at the i th probe and I is the identity matrix used to represent the thermal noise level of the receiver for
 15 simulation purposes.

Prior to generating an adaptive null, the adaptive channel weight vector, w , is chosen to synthesize a desired quiescent radiation pattern. When nulling is desired, the optimum set of transmit weights to form an
 20 adaptive null (or nulls), denoted w_a , is computed 254 by

$$w_a = R^{-1} w_q \quad , \quad (5)$$

-27-

where $^{-1}$ means inverse and w_q is the quiescent weight vector. During array calibration, the normalized quiescent transmit weight vector, with transmit element 204₁ radiating, is chosen to be $w_q = (1, 0, 0, \dots, 0)^T$, i.e.,
 5 the transmit channel weight of element 204₁ is unity and the remaining transmit channel weights are zero. Similar weight settings are used to calibrate the remaining transmit elements. For a fully adaptive annular array, focused at the origin in homogeneous tissue, the
 10 normalized quiescent weight vector is simply $w_q = (1, 1, 1, \dots, 1)^T$. Commonly, the weight vector is constrained to deliver a required amount of power to the hyperthermia array or to the tumor. For simplicity in the computer simulation used to analyze the hyperthermia
 15 array, the weights are constrained such that

$$\sum_{n=1}^N |w_n|^2 = 1 \quad , \quad (6)$$

where w_n is the transmit weight for the n th element. It should be noted that in the computer simulations, the electric field due to the normalized weight vector is scaled appropriately to deliver the required amount of
 20 power to the tissue so that a desired focal-region temperature level is achieved after t minutes. The summation of power received at the probes is given by

$$p = w^T R w \quad , \quad (7)$$

-28-

where t means complex conjugate transpose. The signal-plus-noise-to-noise ratio for the auxiliary probe array, denoted SNR_p , is computed as the ratio of the auxiliary probe array output power (defined in Equation (7)) with the transmit signal present, to the probe array output power with only receiver noise present, that is,

$$INR = \frac{w^t R w}{w^t w} \quad (8)$$

Next, the adaptive array cancellation ratio indicative of the null strength, denoted C , is determined. C is defined here as the ratio of the summation of probe-received power after adaptation to the summation of probe-received power before adaptation (quiescent); that is,

$$C = \frac{P_a}{P_q} \quad (9)$$

A large amount of cancellation indicated by a large value for C indicates a strong null, while a small amount of cancellation indicated by a small value for C indicates a weak null. Substituting Equation (7) into Equation (9) yields

$$C = \frac{w_a^t R w_a}{w_q^t R w_q} \quad (10)$$

-29-

Next, the channel correlation matrix defined by the elements in Equations (2) or (3) is Hermitian (that is, $R=R^\dagger$), which, by the spectral theorem, can be decomposed in eigenspace as

$$R = \sum_{k=1}^M \lambda_k \mathbf{e}_k \mathbf{e}_k^\dagger \quad (11)$$

5 where λ_k , $k=1,2,\dots,M$ are the eigenvalues of R , and \mathbf{e}_k , $k=1,2,\dots,M$ are the associated eigenvectors of R . The channel correlation matrix eigenvalues $(\lambda_1, \lambda_2, \dots, \lambda_M)$ are a convenient quantitative measure of the use of the adaptive array degrees of freedom. The amplitude spread
 10 between the largest and smallest eigenvalues is a quantitative measure of the dynamic range of the interference (hot spot) signals. FIG. 9 is a block diagram of the sample matrix inversion algorithm implemented by the signal processor 116 of FIG. 6.
 15 Receiver 114 generates probe-received complex voltage vector $v_1^i, v_2^i, \dots, v_N^i$ for the i th auxiliary probe. The signal processor generates 280 the transmit channel correlations R_{mn}^i defined by equation (3), and sums 282 them to form the channel correlation matrix R defined by
 20 equation (4). Next, the signal processor multiplies 284 the inverse of the channel correlation matrix R^{-1} by the quiescent transmit weight vector w_q to form the new adapted transmit weight vector w_a containing the adapted transmit weights fed back to the transmit weight networks
 25 110_n of FIG. 6.

-30-

Gradient Search Algorithm

Under conditions where only the probe received voltage amplitude is measured, it is appropriate to consider a gradient search algorithm to minimize the interference power at selected positions. The gradient search is used to control the transmit weights w_n iteratively such that the RF signal received by the probe array is minimized. The transmit array weights (gain and phase) are adaptively changed in small increments and the probe array output power is monitored to determine weight settings that reduce the output power most rapidly to a null.

Consider J sets of N transmit weights that are applied to adaptive hyperthermia phased array applicator 102 of FIG. 6. In terms of adaptive nulling, the optimum transmit weight settings (from the collection of J sets of N transmit weights) occur when the SNR_p is minimized. Equivalently, the total interference power received by the auxiliary probe array, denoted p^{rec} , is to be minimized. For notational convenience let a figure of merit F denote either the SNR_p or p^{rec} and employ a gradient search to find the optimum transmit weights to minimize F , that is,

$$F_{opt} = \min(F_j) \quad j=1,2,\dots,J. \quad (12)$$

The transmit weight settings for which F_{opt} occurs yields the closest approximation to the optimal transmit weights determined by using the sample matrix inverse approach described above.

FIG. 10 shows an amplitude and phase scatter diagram for the N complex transmit weights w_n at the j th configuration, i.e., the j th set of weights tried. The

-31-

nth transmit weight in the jth configuration of transmit weights is denoted

$$w_{nj} = A_{nj} e^{j\Phi_{nj}}, \quad (13)$$

where A_{nj} is the transmit weight amplitude distributed over the range A_{min} to A_{max} and Φ_{nj} is the transmit weight phase distributed over the range $-\pi$ to π radians.

Referring also to FIG. 11, it is desired to find the values of amplitude and phase for each of the N transmit weights such that the figure of merit F (SNR_p or p^{rec}) is minimized. When the figure of merit is minimized, adaptive radiation pattern nulls will be formed at the auxiliary probe positions.

Assuming an initial setting of the N transmit weights such as those selected to focus the radiation pattern on a tumor, the weights are adjusted by dithering them until the optimum figure of merit is achieved. It is desired to find the collective search directions for the N transmit weights such that F decreases most rapidly. That is, weights are selected so that the directional derivative is minimized at (A_j, Φ_j) , where A_j and Φ_j are vectors representing the transmit amplitude weights and transmit phase weights, respectively, for the j th configuration.

The directional derivative of F_j is expressed in terms of the amplitude and phase changes of the transmit weights as

-32-

$$D(F_j) = \sum_{n=1}^N \left(\frac{\partial F_j}{\partial A_{nj}} r_{Anj} + \frac{\partial F_j}{\partial \Phi_{nj}} r_{\Phi nj} \right) \quad (14)$$

where ∂ means partial derivative, and r_{Anj} , $r_{\Phi nj}$ are the (A, Φ) directions for which F_j is decreasing most rapidly. The directions r_{Anj} , $r_{\Phi nj}$ are constrained by

$$\sum_{i=1}^N (r_{Anj}^2 + r_{\Phi nj}^2) = 1 \quad (15)$$

It is desired to minimize $D(F_j)$ subject to the above
5 constraint equation.

Using Lagrange multipliers it is possible to construct the Lagrangian function

$$L_j = \sum_{n=1}^N \left(\frac{\partial F_j}{\partial A_{nj}} r_{Anj} + \frac{\partial F_j}{\partial \Phi_{nj}} r_{\Phi nj} \right) + G \left[1 - \sum_{n=1}^N (r_{Anj}^2 + r_{\Phi nj}^2) \right] \quad (16)$$

where G is a constant to be determined. The requirement that L_j be an extremum implies

$$\frac{\partial L_j}{\partial r_{Anj}} = \frac{\partial F_j}{\partial A_{nj}} - 2Gr_{Anj} = 0, n=1, 2, \dots, N \quad (17)$$

10 and

$$\frac{\partial L_j}{\partial r_{\Phi nj}} = \frac{\partial F_j}{\partial \Phi_{nj}} - 2Gr_{\Phi nj} = 0, n=1, 2, \dots, N \quad (18)$$

-33-

or that

$$r_{Anj} = \frac{1}{2G} \frac{\partial F_j}{\partial A_{nj}} \quad (19)$$

and

$$r_{\Phi nj} = \frac{1}{2G} \frac{\partial F_j}{\partial \Phi_{nj}} \quad (20)$$

Squaring equations (19) and (20) and invoking equation (15) yields

$$\sum_{i=1}^N (r_{Anj}^2 + r_{\Phi nj}^2) = 1 = \frac{1}{4G^2} \sum_{n=1}^N \left[\left(\frac{\partial F_j}{\partial A_{nj}} \right)^2 + \left(\frac{\partial F_j}{\partial \Phi_{nj}} \right)^2 \right] \quad (21)$$

5 thus,

$$G = \pm \frac{1}{2} \sqrt{\sum_{n=1}^N \left[\left(\frac{\partial F_j}{\partial A_{nj}} \right)^2 + \left(\frac{\partial F_j}{\partial \Phi_{nj}} \right)^2 \right]} \quad (22)$$

-34-

Substituting this expression for G in equations (19) and (20) gives

$$I_{A_{nj}} = - \frac{\frac{\partial F_j}{\partial A_{nj}}}{\sqrt{\sum_{n=1}^N \left[\left(\frac{\partial F_j}{\partial A_{nj}} \right)^2 + \left(\frac{\partial F_j}{\partial \Phi_{nj}} \right)^2 \right]}} \quad (23)$$

and

$$I_{\Phi_{nj}} = - \frac{\frac{\partial F_j}{\partial \Phi_{nj}}}{\sqrt{\sum_{n=1}^N \left[\left(\frac{\partial F_j}{\partial A_{nj}} \right)^2 + \left(\frac{\partial F_j}{\partial \Phi_{nj}} \right)^2 \right]}} \quad (24)$$

- The minus sign was chosen corresponding to the direction of maximum function decrease. This choice of minus sign in equation (22) enforces nulls in the hyperthermia array radiation pattern. Alternatively, if the positive sign in equation (22) is selected, then the gradient directions can be used to maximize the figure of merit for the purposes of focusing at an invasive probe at the tumor site, i.e., maximize the SNR_F . This may be used, for example, to determine the quiescent transmit weight vector w_q . Thus, two gradient searches may be performed to optimize the radiation pattern of the hyperthermia array.
- The first to produce a peak or focused radiation pattern at the tumor, and the second to form the desired nulls at the auxiliary probes. Furthermore, these two gradient searches may be implemented as a single, combined gradient

-35-

search constrained to maximize the radiation pattern at the focus and minimize the radiation pattern at the desired nulls. The combined gradient search is implemented by minimizing the figure of merit defined as the ratio of the power received at the auxiliary probes to the power received by the probe at the focus.

The partial derivatives

$$\frac{\partial F_j}{\partial A_{nj}}, \frac{\partial F_j}{\partial \Phi_{nj}}; n=1, 2, \dots, N \quad (25)$$

represent the gradient directions for maximum function decrease. Since the figure of merit F cannot be expressed here in analytical form, the partial derivatives are numerically evaluated by using finite differences. Thus, we write

$$\frac{\partial F_j}{\partial A_{nj}} = \frac{\Delta F_{Anj}}{2\Delta A_{nj}} \quad (26)$$

and

$$\frac{\partial F_j}{\partial \Phi_{nj}} = \frac{\Delta F_{\Phi nj}}{2\Delta \Phi_{nj}} \quad (27)$$

where as shown in FIG. 2 the figure of merit differences are

-36-

$$\Delta F_{A_{nj}} = F_j(A_{nj} + \Delta A_{nj}; \Phi_{nj}) - F_j(A_{nj} - \Delta A_{nj}; \Phi_{nj}) \quad (28)$$

and

$$\Delta F_{\Phi_{nj}} = F_j(A_{nj}; \Phi_{nj} + \Delta \Phi_{nj}) - F_j(A_{nj}; \Phi_{nj} - \Delta \Phi_{nj}) \quad (29)$$

and ΔA_{nj} and $\Delta \Phi_{nj}$ are assumed to be small increments.
 We will assume that the increments ΔA_{nj} and $\Delta \Phi_{nj}$ are
 independent of the configuration number and element
 5 number, that is,

$$\Delta A_{nj} = \Delta A \quad (30)$$

and

$$\Delta \Phi_{nj} = \Delta \Phi \quad (31)$$

Substituting equations (26), (27), (30) and (31) in
 equations (23) and (24) gives the desired result for the
 10 search directions

-37-

$$r_{Anj} = - \frac{\frac{\Delta F_{Anj}}{\Delta A}}{\sqrt{\sum_{n=1}^N \left[\left(\frac{\Delta F_{Anj}}{\Delta A} \right)^2 + \left(\frac{\Delta F_{\Phi nj}}{\Delta \Phi} \right)^2 \right]}} \quad (32)$$

and

$$r_{\Phi nj} = - \frac{\frac{\Delta F_{\Phi nj}}{\Delta \Phi}}{\sqrt{\sum_{n=1}^N \left[\left(\frac{\Delta F_{Anj}}{\Delta A} \right)^2 + \left(\frac{\Delta F_{\Phi nj}}{\Delta \Phi} \right)^2 \right]}} \quad (33)$$

Equations (32) and (33) are used to compute the new amplitude and phase settings of the (j+1)th transmit weight configuration according to

$$A_{n,j+1} = A_{nj} + \Delta A r_{Anj} \quad (34)$$

5 and

$$\Phi_{n,j+1} = \Phi_{nj} + \Delta \Phi r_{\Phi nj} \quad (35)$$

In practice, it may be necessary to keep one of the transmit weights fixed (in amplitude and in phase) during the gradient search to guarantee convergence.

FIG. 12 is a block diagram of the gradient search algorithm implemented by the signal processor 116 of FIG. 6. Each of the N transmit antennas 104_n of phased array applicator 102 (FIG. 6) is driven through its

-38-

corresponding weighting network 110_n which applies complex transmit weights w_{nj} at the j th configuration of the weights. The transmit antennas induce a voltage across the i th probe antenna 112_i at the corresponding input to receiver 114 (FIG. 6). Receiver 114 amplifies the signal received from the i th probe by gain a_i to produce voltage amplitude vector $|v_{1j}^i|, |v_{2j}^i|, \dots, |v_{Nj}^i|$ at the receiver output.

The voltage amplitude vector is input to signal processor 116 which performs the gradient search. For any initial configuration ($j=1$) of the transmit weights w_{nj} , the signal processor causes each weight to be dithered by a small amount in amplitude, ΔA_{nj} , and phase, $\Delta \phi_{nj}$. Each transmit weight is dithered independent of the other transmit weights, which remain in their j th configuration state. Received voltage vectors $|v_{1j}^i|, |v_{2j}^i|, \dots, |v_{Nj}^i|$, i.e., are stored and used to calculate the resulting figure of merit F_{nj} 300 for each dithered condition, the figure of merit being the power received by the auxiliary probe array. The figure of merit is a rectangular matrix of dimension $N \times 4$, where the dimensionality of four is due to the plus and minus dithering of both of the amplitude and phase. The figure of merit differences ΔF_{Anj} and $\Delta F_{\phi nj}$ caused by dithering the amplitude and phase, respectively, are calculated according to equations (28) and (29). The gradient search directions r_{Anj} and $r_{\phi nj}$, based upon minimizing the auxiliary probe array received power, are then determined 302 from the figure of merit differences according to equations (32) and (33), respectively. The resulting search directions are used to update 304 transmit weights w_{nj} to the $(j+1)$ th configuration transmit weights $w_{n, (j+1)}$ according to

-39-

equations (34) and (35). The transmit weights $w_{n, (j+1)}$ are sent to update the transmit weighting networks 110_n , and the process is repeated. The final adaptive weight vector w_a is achieved when the $(j+1)$ th transmit weight configuration has converged. Convergence is expected to occur within several hundred iterations depending on the dither step size ΔA and $\Delta \Phi$.

It is understood that other forms of gradient searches exist which can be used to update the transmit weights toward convergence. Another such gradient search approach, where the step sizes ΔA and $\Delta \Phi$ are computed at each iteration, is described by D.J. Farina and R.P. Flam, "A Self-normalizing Gradient Search Adaptive Array Algorithm", IEEE Transactions on Aerospace and Electronic Systems, November 1991, Vol. 27, No. 6, pp 901-905.

COMPUTER SIMULATION OF ADAPTIVE NULLING HYPERTHERMIA Moment-Method Formulation

Referring again to FIG. 8, a method of moments formulation 258 is used to compute the probe-received voltages in Equation (2) due to the transmitting hyperthermia phased-array antenna in an infinite homogeneous conducting medium. The medium is described by the three parameters μ , ϵ , and σ , which are discussed below. The formulation given here is analogous to that developed under array-receiving conditions for an adaptive radar. The software used to analyze a hyperthermia array is based on the receive-array analogy but the theory presented below is given in the context of a transmit array.

An antenna analysis code (WIRES) originally developed by J.H. Richmond is capable of analyzing antenna or radar

-40-

cross section problems. See, J.H. Richmond, "Computer program for thin-wire structures in a homogeneous conducting medium", Ohio State University, ElectroScience Laboratory, Technical Report 2902-12, August 1973; and,

5 J.H. Richmond, "Radiation and scattering by thin-wire structures in a homogeneous conducting medium (computer program description)", IEEE Trans. Antennas Propagation, Vol. AP-22, no. 2, p.365, March 1974. WIRES was modified to analyzing the near-field and far-field adaptive nulling

10 performance of thin-wire phased arrays in free space. A new version of the thin-wire code that can analyze adaptive hyperthermia arrays in an infinite homogeneous conducting medium was written to conduct the adaptive hyperthermia simulation discussed below. The new version

15 of the thin-wire code is attached as Appendix A.

WIRES is a moment-method code that uses the electric field integral equation (EFIE) to enforce the boundary condition of the tangential electric field being zero at the surface of the antenna of interest. The moment-method

20 basis and testing functions used in this code are piecewise sinusoidal.

Appendix B lists sample input and output files for the adaptive hyperthermia simulation. The first data file was used to generate the E-field results for a four

25 auxiliary probe system, and the second data file was used to generate the E-field results for a two auxiliary probe system. The corresponding output files give the values for the array mutual coupling, quiescent and adaptive transmit weights, channel correlation matrix, eigenvalues,

30 and cancellation.

Referring to FIG. 13, there is shown the hyperthermia phased-array antenna system 200 of FIG. 7, redrawn to

-41-

simplify the following method of moments analysis. The RF source 208, power divider 209 and weights 210_n of FIG. 7, are modeled as a plurality of RF signal generators 250_1 through 250_N , feeding its corresponding transmit antenna element 204_1 through 204_N . Each generator 250_1 through 250_N has a corresponding amplitude and phase weight denoted by w_1 through w_N , and a known output impedance Z_L . The j th probe 226 (i.e., the same as the i th probe 226 of FIG. 7, with different notation) is modeled as a dipole antenna having an overall length L_p and an open-circuit voltage $v_j^{o.c.}$ induced by the RF energy transmitted from the antenna array 200.

The open-circuit voltage at the j th probe antenna 226 is computed from the array terminal currents and from Z_n^j , the open-circuit mutual impedance between the n th array element and the j th probe antenna. Let $v_{n,j}^{o.c.}$ represent the open-circuit voltage at the j th probe due to the n th transmit-array element. Here, the j th probe can denote either the focal point calibration probe (calibration probe 212 of FIG. 7) or one of the auxiliary probes used to null a sidelobe. The number of auxiliary probes is denoted by N_{aux} .

Referring also to FIG. 14, the j th probe 226 is modeled as a voltage source 260, having an output voltage $v_j^{o.c.}$, driving a first impedance 262, representing the input impedance Z_{IN} of the j th probe, in series with a second impedance 264, representing the termination impedance Z_r of the j th probe. The j th probe receive current i_j^{rec} flows through these two impedances. The output voltage of the j th probe v_j^{rec} appears across the termination impedance Z_r .

-42-

Referring again to FIG. 13, next, let \mathbf{Z} denote the open-circuit mutual impedance matrix (with dimensions $N \times N$ for the N -element array). The open-circuit mutual impedance between array elements 204_m and 204_n is denoted $Z_{m,n}$. It is assumed that multiple interaction between the hyperthermia array and the auxiliary probe can be neglected. Thus, the hyperthermia array terminal current vector \mathbf{i} can be computed in terms of the transmit weights \mathbf{w} as

$$\mathbf{i} = [\mathbf{Z} + \mathbf{Z}_L \mathbf{I}]^{-1} \mathbf{w} \quad (36)$$

Next, let $Z_{n,j}$ be the open-circuit mutual impedance between the j th probe and the n th array element. The induced open-circuit voltage $v_{n,j}^{o.c.}$ at the j th receive probe, due to the n th array element transmit current i_n , can then be expressed as

$$v_{n,j}^{o.c.} = Z_{n,j}^j \cdot i_n \quad (37)$$

In matrix form, the induced open-circuit probe-voltage matrix $\mathbf{v}_{probe}^{o.c.}$ is

$$\mathbf{v}_{probe}^{o.c.} = \mathbf{Z}_{probe,array} \mathbf{i} \quad (38)$$

or

-43-

$$V_{probe}^{o.c.} = Z_{probe, array} [Z + Z_L I]^{-1} W \quad (39)$$

where $Z_{probe, array}$ is a rectangular matrix of order $N_{aux} \times N$ for the open-circuit mutual impedance between the probe array and the hyperthermia array. Note that the j th row of the matrix $Z_{probe, array}$ is written as $(Z_1^j, Z_2^j, \dots, Z_N^j)$, where $j=1, 2, \dots, N_{aux}$. The receive voltage matrix is then computed by the receiving circuit equivalence theorem for an antenna. The receive-antenna equivalent circuit is depicted in FIG. 14, where it is readily determined that

$$V_{probe}^{rec} = V_{probe}^{o.c.} \frac{Z_r}{Z_{in} + Z_r} \quad (40)$$

10 where Z_{in} is the input impedance of the probe. It should be noted that the V_{probe}^{rec} matrix is a column vector of length N_{aux} and V_j^{rec} is the j th element of the matrix. The probe-receive current matrix is given by

$$I_{probe}^{rec} = V_{probe}^{o.c.} \frac{1}{Z_{in} + Z_r} \quad (41)$$

15 The j th element of the column vector I_{probe}^{rec} is denoted I_j^{rec} , $j=1, 2, \dots, N_{aux}$. Finally, the power received by the j th probe is

-44-

$$p_j^{rec} = \frac{1}{2} \operatorname{Re}(v_j^{rec} \cdot i_j^{rec*}) \quad (42)$$

where Re means real part. Substituting Equations (40) and (41) into Equation (42) yields

$$p_j^{rec} = \frac{1}{2} |v_j^{o.c.}|^2 \frac{\operatorname{Re}(Z_r)}{|Z_{in} + Z_r|^2} \quad (43)$$

The total interference power received by the auxiliary probe array is given by

5

$$p^{rec} = \sum_{j=1}^{J_{aux}} p_j^{rec} \quad (44)$$

The incident electric field E is related to the open-circuit voltage $v^{o.c.}$ by the effective height h of the probe antenna as

$$v^{o.c.} = hE \quad (45)$$

10 If the length L_p of the probe antenna 226 is approximately 0.1 λ or less, the current distribution is triangular and the effective height is $h = 0.5L_p$. Thus, for a short-dipole probe the open-circuit voltage can be expressed as

-45-

$$V^{o.c.} = \frac{L_p}{2} E \quad (46)$$

It then follows from Equation (46) that the E field for a short-dipole probe at position (x, y, z) is given by

$$E(x, y, z) = \frac{2V^{o.c.}(x, y, z)}{L_p} \quad (47)$$

Finally, the quiescent and adapted E-field radiation patterns are computed using the quiescent and adapted weight vectors w_q and w_a , respectively, in Equations (39) and (47). The moment-method expansion and testing functions are assumed to be sinusoidal. The open-circuit mutual impedances in Equation (39) between thin-wire dipoles in a homogeneous conducting medium are computed based on subroutines from the moment-method computer code developed by J.H. Richmond. In evaluating Z_n^j for the j th auxiliary probe, double precision computations are used.

As mentioned previously, the array is calibrated (phased focused) initially using a short dipole at the focal point. To accomplish this numerically, having computed V_{focus}^{rec} , the transmit array weight vector w will have its phase commands set equal to the conjugate of the corresponding phases in V_{focus}^{rec} . Transmit antenna radiation patterns are obtained by scanning (moving) a dipole probe with half-length l in the near-field and computing the receive probe-voltage response.

The received voltage matrix for the j th probe (denoted V_j^{rec}) is computed at K frequencies across the

-46-

nulling bandwidth. Thus, $v_j^{rec}(f_1), v_j^{rec}(f_2), \dots, v_j^{rec}(f_K)$ are needed. For the purposes of this computer simulation, the impedance matrix is computed at K frequencies and is inverted K times. The probe channel correlation matrix elements are computed by evaluating Equation (2) numerically, using Simpson's rule numerical integration. For multiple auxiliary probes, the channel correlation matrix is evaluated using Equation (4). Adaptive array radiation patterns are computed by superimposing the quiescent radiation pattern with the weighted sum of auxiliary-channel-received voltages.

Wave Propagation in Conducting Media

To gain insight into the effect of a lossy medium, e.g., the target body, on the propagation of an electromagnetic wave, it is useful to review certain fundamental equations which govern the field characteristics. In a conducting medium, Maxwell's curl equations in time-harmonic form are

$$\nabla \times H = J + j\omega\epsilon E \quad (48)$$

and

$$\nabla \times E = -j\omega\mu H \quad (49)$$

where E and H are the electric and magnetic fields, respectively, J is the conduction current density, $\omega = 2\pi f$ is the radian frequency, ϵ is the permittivity of the medium, and μ is the permeability of the medium. The permittivity is expressed as $\epsilon = \epsilon_r \epsilon_0$, where ϵ_r is the

-47-

dielectric constant (relative permittivity) and ϵ_0 is the permittivity of free space. Similarly, $\mu = \mu_r \mu_0$, where μ_r is the relative permeability and μ_0 is the permeability of free space. For a medium with electrical conductivity σ , J and E are related as

$$J = \sigma E \quad (50)$$

Substituting Equation (50) into Equation (48) yields

$$\nabla \times H = (\sigma + j\omega\epsilon) E \quad (51)$$

From Equations (48) and (49), the vector wave equation in terms of E is derived as

$$\nabla^2 E - \gamma^2 E = 0 \quad (52)$$

It is readily shown that

$$\gamma = \pm \sqrt{j\omega\mu(\sigma + j\omega\epsilon)} = \pm j\omega\sqrt{\mu\epsilon} \sqrt{1 - j\frac{\sigma}{\omega\epsilon}} \quad (53)$$

- 10 The quantity $\sigma/\omega\epsilon$ is referred to as the loss tangent. It is common to express the complex propagation constant as

-48-

$$\gamma = \alpha + j\beta \quad (54)$$

where α is the attenuation constant and β is the phase constant. The constants α and β are found by setting Equation (53) equal to Equation (54) and then squaring both sides, equating the real and imaginary parts, and
 5 solving the pair of simultaneous equations, with the result

$$\alpha = \frac{\omega\sqrt{\mu\epsilon}}{\sqrt{2}} \left[\sqrt{1 + \left(\frac{\sigma}{\omega\epsilon}\right)^2} - 1 \right]^{1/2} \quad (55)$$

and

$$\beta = \frac{\omega\sqrt{\mu\epsilon}}{\sqrt{2}} \left[\sqrt{1 + \left(\frac{\sigma}{\omega\epsilon}\right)^2} + 1 \right]^{1/2} \quad (56)$$

The wavelength λ in the lossy dielectric is then computed from

$$\lambda = \frac{2\pi}{\beta} \quad (57)$$

10 The intrinsic wave impedance η is given by

$$\eta = \sqrt{\frac{j\omega\mu}{\sigma + j\omega\epsilon}} = \sqrt{\frac{\mu}{\epsilon}} \frac{1}{\sqrt{1 - j\frac{\sigma}{\omega\epsilon}}} \quad (58)$$

-49-

The instantaneous power density of the electromagnetic field is given by Poynting's vector, denoted P ,

$$P = \frac{1}{2} E \times H^* \quad (59)$$

which has units of (W/m^2) . The time-average power flow density is equal to the real part of the complex Poynting's vector. The time-average power dissipation per unit volume P_d (W/m^3) is derived from Maxwell's equations, with the result

$$P_d = \frac{1}{2} E \cdot J^* = \frac{1}{2} \sigma |E|^2 \quad (60)$$

The specific absorption rate (SAR) is the power dissipated or absorbed per unit mass (W/kg) of the medium (tissue), or

$$SAR = \frac{P_d}{\rho} = \frac{\sigma}{2\rho} |E|^2 \quad (61)$$

where ρ is the density of the medium in kg/m^3 .

It is convenient to have a simple equation for computing the propagation loss between any two points in the near field of an isolated transmitting antenna. Thus,

-50-

mutual coupling effects are ignored for the time being. Consider a time-harmonic source radiating a spherical wave into an infinite homogeneous conducting medium. For an isotropic radiator, and suppressing the $e^{j\omega t}$ time dependence, the electric field as a function of range r can be expressed as

$$E(r) = E_o \frac{e^{-\gamma r}}{r} \quad (62)$$

where E_o is a constant.

For a source at the origin, the amplitude of the electric field at range r_1 is given by

$$|E(r_1)| = E_o \frac{e^{-\alpha r_1}}{r_1} \quad (63)$$

10 and at range r_2 by

$$|E(r_2)| = E_o \frac{e^{-\alpha r_2}}{r_2} \quad (64)$$

The total propagation loss between ranges r_1 and r_2 is found by taking the ratio of Equations (64) and (63), or

$$\frac{|E(r_2)|}{|E(r_1)|} = \frac{r_1}{r_2} e^{-\alpha(r_2-r_1)} \quad (65)$$

-51-

The field attenuation A_α in dB from range r_1 to range r_2 due to the lossy dielectric is simply

$$A_\alpha = 20 \log_{10} (e^{-\alpha(r_2 - r_1)}) \quad (66)$$

Similarly, the $1/r$ attenuation loss A_r in dB is

$$A_r = 20 \log_{10} \frac{r_1}{r_2} \quad (67)$$

Thermal Modeling of an Inhomogeneous Target

5 A thermal analysis computer program called the transient thermal analyzer (TTA), developed by Arthur D. Little, Inc., has been used to accomplish the thermal modeling of homogeneous muscle tissue surrounded by a constant-temperature water bolus.

10 The TTA program uses the finite-difference technique to solve a set of nonlinear energy balance equations. Consider a system of interconnected nodes that model an inhomogeneous volume for which the temperature T_i of the i th node is to be determined. The heat-balance equation,
15 which is solved by TTA, is expressed as

$$\sum_{i=1}^N Q_{i,j} - P_i(t) + M_i \frac{dT_i}{dt} = 0 \quad (68)$$

-52-

where $Q_{i,j}$ is the net outward heat flow from node i in the direction of node j , $P_i(t)$ is the power into node i at time t , and M_i is the thermal mass (mass times specific heat) of node i .

5 FIG. 15 shows an electric circuit analog 400 which is used to model the two-dimensional thermal characteristics of the material volume 402 which simulates the target body as a plurality of uniformly distributed nodes 406 spaced Δl apart. With reference to the i th node 406 _{i} , but
 10 applying generally to the other nodes, power P_i in watts is delivered 404 _{i} to the i th node. Capacitor 408 _{i} , having thermal capacitance denoted C_i (with units Joules/°C), is used to model the thermal capacitance at the i th node. Resistor 410 _{ij} , having heat resistance denoted $R_{i,j}$ (with
 15 units °C/W), is used to model the heat resistance between i th node 406 _{i} and the j th node 406 _{j} .

With a spacing of Δl between nodes (assuming cubic cells), the values of $R_{i,j}$, C_i and P_i are computed as

$$R_{i,j} = \frac{1}{k_{i,j} \Delta l} \quad (69)$$

where $k_{i,j}$ is the thermal conductivity (with units W/m°C)
 20 between nodes i and j ;

$$C_i = \rho_i C_{pi} (\Delta l)^3 \quad (70)$$

where C_{pi} is the specific heat at the i th node and ρ_i is the density (kg/m³) at the i th node; and

-53-

$$P_i = (SAR)_i \rho_i (\Delta l)^3 \quad (71)$$

where $(SAR)_i$ is the SAR for the i th node, which is given by

$$(SAR)_i = \frac{\sigma_i}{2\rho_i} |E_i|^2 \quad (72)$$

where σ_i is the electrical conductivity of the i th node and $|E_i|$ is the magnitude of the electric field delivered by the hyperthermia array to the i th node. It should be noted that in substituting Equation (72) into Equation (71), the density ρ_i cancels. Thus, an equivalent approach to computing the power delivered to the i th node is written in terms of the time-average power dissipated per unit volume of the i th node (denoted P_{di}) as

$$P_i = P_{di} (\Delta l)^3 \quad (73)$$

FIG. 16 is a block diagram showing how TTA is used in the hyperthermia simulation described herein. First, the method of moments 500, controlled by the SMI nulling algorithm 502, is used to compute the electric field radiation pattern throughout a homogeneous region, simulating muscle tissue, inside an annular phased array 501. These E-field simulations assume that the signal received by a short-dipole probe within the region is due

-54-

to a transmitting phased array embedded in an infinite homogeneous lossy dielectric (muscle tissue).

The resulting E-Field power distribution is then read 504 into the TTA program 506, which computes the
5 temperature distribution inside an elliptical muscle-tissue target surrounded with a constant-temperature water bolus 507. Because the RF wavelengths in the target and water bolus are similar, the E-field simulations are believed to give a reasonable
10 approximation to the field distribution inside the elliptical target. The computed temperature distribution is output 508 from the TTA for further analysis or display.

The E-field calculation in the assumed infinite
15 homogeneous medium introduces additional field attenuation not present in a clinical hyperthermia system with an annular array transmitting through a water bolus into a patient. As mentioned earlier, the water bolus has very little RF propagation loss. In addition, the transmit
20 array weights are normalized according to Equation (6). Thus, no attempt is made to compute the absolute E-field strength in volts/meter in the elliptical target. Instead, the peak power in the elliptical target is adjusted (by a scale factor) to produce a desired maximum
25 focal-region temperature (T_{max}) after t minutes. It should be noted that an approximate absolute scale factor could be computed by making an initial computer simulation with an infinite homogeneous water bolus and then matching the target boundary field to the infinite homogeneous muscle
30 tissue simulation.

The computer simulation model is related, in part, to the hyperthermia annular phased-array antenna system shown

-55-

in FIG. 1. The simulated array is assumed to have a 60-cm array diameter with eight uniformly spaced dipole elements which operate over the frequency band 60-120 MHz. The eight elements of the array are assumed to be fully
5 adaptive, whereby seven independent nulls can be formed while simultaneously focusing on a tumor.

It is further assumed for the purpose of this simulation that the adaptive radiation pattern null-width characteristics in a homogeneous target are similar to the
10 characteristics observed in an inhomogeneous target. The null-width characteristics are directly related to the RF wavelength, and, only a 5 percent change in wavelength occurs between the assumed muscle tissue and water bolus. With this assumption, the transmit array may be simulated
15 as embedded in homogeneous tissue, which allows direct use of the thin-wire moment-method formulation discussed above.

After computing the two-dimensional E-field distribution in the homogeneous medium, we then consider
20 only an elliptical portion of the homogeneous region and use the ellipse as the homogeneous target. In the thermal analysis, the elliptical target is surrounded with a constant 10°C water bolus. The E-field amplitude is scaled to produce a 46°C peak temperature, at time $t=20$
25 minutes, at the center of the elliptical phantom. The initial temperature of the phantom is assumed to be 25°C (room temperature).

All computer simulations assume a 120 MHz operating frequency with initially four auxiliary nulling probes,
30 i.e., $N_{aux}=4$. The parameters used in the electrical and thermal analyses are summarized in Table 1. These parameters are for a frequency of 100 MHz, but is assumed

-56-

that similar values of the parameters will exist at 120 MHz. It should be noted that although the relative dielectric constants of phantom muscle tissue and distilled water are very similar, the electrical

5 conductivities are vastly different. The relevant thermal characteristics---density, specific heat, and thermal conductivity---are very similar for phantom muscle tissue and distilled water.

SIMULATION RESULTS

10 Electric Field for Array in Homogeneous Tissue

Substituting the values $f=120$ MHz, $\sigma=0.5$ S/m, and $\epsilon_r=73.5$ into Equation (53) yields $\gamma_m = 10.0 + j23.8$ for the muscle tissue. With $\beta_m = 23.8$ radians/m, the wavelength in the phantom muscle tissue is $\lambda_m=26.5$ cm.

15 The attenuation constant for the muscle tissue is $\alpha_m=10.0$ radians/m. Similarly, for distilled water $\gamma_w = 0.0021 + j22.5$, so the wavelength is $\lambda_w=27.9$ cm. The attenuation constant for the distilled water medium is $\alpha_w=0.0021$ radians/m. The propagation loss in the phantom muscle

20 tissue is $20\log_{10}e^{-10.0}$, or -0.87 dB/cm. Similarly, the propagation loss in the distilled water is found to be -0.0002 dB/cm. Thus, the total loss due to propagation through 15 cm of distilled water is 0.003 dB. For 15 cm of muscle tissue the corresponding loss is 13.1 dB. The

25 wave impedance in the muscle tissue is computed from Equation (58) as $\eta_m = 33.9 + j14.2 \Omega$, and similarly in the distilled water $\eta_w = 42.1 + j0.004 \Omega$.

FIG. 17 shows the geometry used in the simulations, which parallels the array shown in FIG. 3. A

30 60-cm-diameter ring phased array applicator 102 of eight perfectly conducting center-fed dipoles, 104₁ through

-57-

104₈, uniformly surrounds a fictitious elliptical target zone 106 with major axis 30 cm and minor axis 20 cm. The length of each dipole array element 104_n at 120 MHz in the infinite homogeneous muscle tissue is $\lambda/2$, or 13.25 cm.

- 5 The array focus 107 is assumed at the origin ($x=0$, $y=0$, $z=0$) and four auxiliary short-dipole probes, 112₁ through 112₄, with length 1.27 cm (0.05λ) are positioned at (x,y,z) coordinates at (15 cm, 0, 0), (-15 cm, 0, 0), (0, 0, 10 cm), and (0, 0, -10 cm), respectively, i.e., the
10 auxiliary E-field probes are located every 90° in azimuth on the perimeter of the target. In rectangular coordinates, each dipole is oriented along the \hat{y} direction and the feed terminals of each dipole are located at $y=0$.

- The moment-method computer simulations were run on a
15 Sun 3/260 workstation. The total CPU time for a complete moment-method run is 19.2 minutes. This CPU time includes computing the quiescent and adaptive radiation patterns on a 41 by 41 grid of points. The CPU time without radiation pattern calculations is 33 seconds.

- 20 FIG. 18 shows the two-dimensional radiation pattern in the plane $y=0$, before nulling, at 120 MHz with uniform amplitude and phase illumination. The calculated data are collected on a 41 by 41 grid of points over a square region, with side length 76.2 cm, centered at the focus
25 107. The spacing between data points is 1.905 cm, or 0.072λ , and the contour levels are displayed in 10-dB steps. The E-field data are computed for the case of a 1.27-cm short-dipole observation probe. The positions of the eight dipole radiators 104₁ through 104₈ are clearly
30 evident by the -20 dB contours surrounding each element. The radiation pattern is symmetric because of the symmetry of the array and the assumed homogeneous medium.

-58-

FIG. 19 shows finer contour levels (1-dB steps) for the quiescent radiation pattern of FIG. 18. Here, it is evident that the focused main beam of the ring array is increasing in amplitude as the observation point moves
5 closer to the focus. Away from the main beam region, the pattern amplitude is seen to increase as the observation position moves toward the array perimeter.

FIG. 20 shows the quiescent radiation pattern of FIG. 18 cut at $z=0$. The large amplitude that occurs at ± 30 cm,
10 i.e., at the position of the phased array applicator 102, is due to the E-field probe's close proximity to the transmitting elements 104₁ and 104₅. The large attenuation that occurs from the array diameter to the focus is due to the $1/r$ attenuation loss and the loss in
15 the uniform homogeneous muscle tissue. FIG. 21 shows the radiation pattern of FIG. 18 cut at $x=0$. Here, the pattern is identical to the pattern of FIG. 20 due to the symmetry of the array. In both FIGS. 20 and 21 the boundary of the fictitious elliptical target zone 106 is
20 indicated. The target zone of FIG. 20 is larger than that of FIG. 21 since the major axis of elliptical target 106 lies along the x-axis, and the minor axis of target 106 lies along the z-axis.

The increasing radiation pattern amplitude near the
25 left and right sides of the elliptical target of FIG. 20 is shown to produce hot spots in the thermal distribution. Because the top (anterior) and bottom (posterior) of the elliptical target of FIG. 21 are not as strongly illuminated as to the left and right sides of the
30 elliptical target of FIG. 20, no quiescent hot spots occur at the top or bottom.

-59-

Further, FIG. 20 shows that the ring-array half-power beamwidth in the target region is approximately 13 cm, or approximately one-half the wavelength (26.5 cm) in the phantom muscle tissue. The adaptive nulling resolution or
5 closest allowed spacing between a strong adaptive null and the main beam has been shown to be equal to the half-power beamwidth of the antenna. Thus, the closest allowed null position is 13 cm from the focus. Since the target width is 30 cm across the major axis, two nulls can be formed at
10 ($x=\pm 15$ cm, $z=0$) at the left and right side of the target without disturbing the focus. However, if two strong nulls are formed at the posterior and anterior ($x=0$, $z=\pm 10$ cm) of the target the focus will be compromised. In practice, the water bolus surrounding the target would
15 restrict the placement of short-dipole probes 112_n to the surface of the target. Thus, only weak nulls can be formed at ($x=0$, $z=\pm 10$ cm) so that the focus will not be affected by the adaptive nulling process. That is, the effect of the two minor axis nulls is to keep the $z=\pm 10$ cm
20 E-field from increasing beyond the quiescent values.

Next, adaptive radiation patterns are computed with four auxiliary dipole probes 112_1 through 112_4 positioned as shown in FIG. 17. The value of the receiving gain for auxiliary dipole probes 112_1 and 112_2 is adjusted to
25 produce a SNR > 35 dB. This amount of SNR results in greater than 35 dB of nulling in the direction of auxiliary dipole probes 112_1 and 112_2 . In contrast, the gain values for auxiliary dipole probes 112_3 and 112_4 are turned down to produce about a 3 dB SNR. Thus, only about
30 3 dB of nulling will occur at probe positions 112_3 and 112_4 as the adaptive algorithm reduces the interference to the noise level of the receiver. The reason for choosing

-60-

these null strengths will become apparent with the data that follow.

FIG. 22 shows the two-dimensional radiation pattern after nulling with four auxiliary probes 112₁ through 112₄. Two strong adaptive nulls at $x=\pm 15$ cm occur as expected, and weak nulling occurs at $z=\pm 10$ cm, also as expected.

The two strong nulls in the $z=0$ cut are quantified in FIG. 23, where greater than 35 dB of interference nulling or pattern reduction occurs at $x=\pm 15$ cm. The peak level at the focus 107 is adjusted to 0 dB for both the quiescent and adaptive patterns. Two weak adaptive nulls are seen in the $x=0$ radiation pattern cut shown in FIG. 24. The weak nulls in effect in the adaptive patterns reduce variation from the quiescent radiation pattern.

FIG. 25(a) shows the two-dimensional radiation pattern before and after nulling taken longitudinally along a line parallel to the y -axis and passing through probe 112₁ as shown in FIG. 25(b), i.e., $x=15$ cm, $z=0$. This radiation pattern clearly shows that a strong adaptive null also extends in the y direction from the E-field probe being nulled.

FIG. 26(a) shows the two-dimensional radiation pattern before and after nulling taken along the y -axis and passing through the focus 107 as shown in FIG. 26(b), i.e., $x=0$, $z=0$. This radiation pattern clearly shows that the E-field at the focus remains virtually the same in the y direction before and after adaptive nulling at the E-field probes 112₁ through 112₄.

FIG. 27(a) shows the transmit array amplitude weights before (solid line) and after (broken line) nulling, and FIG. 27(b) shows the transmit array phase weights before

-61-

(solid line) and after (broken line) nulling. As shown, the adaptive transmit weights exhibit a 5-dB dynamic range in FIG. 27(a).

FIG. 28 shows the channel correlation matrix eigenvalues before (solid line) and after (broken line) nulling. There are two large eigenvalues, λ_1 and λ_2 , and two weak (non-zero) eigenvalues, λ_3 and λ_4 , shown in FIG. 28. These eigenvalues are directly associated with the two high-SNR auxiliary probes 112₁ and 112₂, and the two weak-SNR auxiliary probes 112₃ and 112₄, respectively. Note that the 0-dB level in FIG. 28 is equal to the receiver noise level. The probe-array output power before and after adaptive nulling is 31.4 dB and 0.9 dB, respectively, as calculated from equation (10). This difference in power before and after nulling indicates that the adaptive cancellation is -30.5 dB.

Temperature Distribution in Elliptical Phantom

To simulate the temperature distribution in the target body resulting from the calculated E-fields, the transient thermal analysis (TTA) software is used to compute the temperature distribution in an elliptical phantom surrounded with a constant-temperature water bolus. The 41 X 41 two-dimensional E-field radiation pattern data of FIGS. 18 through 24 are used as the power source for the thermal node network. Two node spacings are considered. First, the node spacing $\Delta x = \Delta z = \Delta l = 1.905$ cm (coarse grid) is used to obtain thermal data. Then, the node spacing is decreased by a factor of two to $\Delta l = 0.9525$ cm (fine grid) to check convergence. The coarser spacing is shown to be adequate.

The scale factors used to convert the normalized E-field distributions to a power level that induces a 46°C

-62-

peak temperature at $t=20$ minutes are 94.1 dB and 96.0 dB for the quiescent and adaptive patterns, respectively. These scale factors are determined empirically. From Equations (68) through (73) and the parameter values given in Table 1, all resistors $R_{i,j}$ in the phantom muscle tissue had a value of 96.5°C/W and all resistors $R_{i,j}$ in the water bolus had a value of 87.2°C/W. The value of the capacitors C_i in the phantom muscle tissue is 23.6 J/°C. Capacitors are not used in the water-bolus region in the input to the transient thermal analysis software. Instead, a constant temperature of 10°C is enforced at each water-bolus node. With a 41 X 41 grid, a total of 3280 resistors and 1681 capacitors are used in the thermal simulation. The CPU time required to compute this temperature distribution is under four minutes. FIG. 29 shows the two-dimensional temperature distribution produced at time $t=20$ minutes in the elliptical phantom muscle tissue target 106 without adaptive nulling. To generate FIG. 29, the power source used in the transient thermal analysis is the quiescent radiation pattern given in FIG. 18. The initial temperature (at time $t=0$) is 25°C. Notice the occurrence of two hot spots 122 and 124 on the left and right sides of the elliptical phantom, respectively. The peak temperature at focus 107 is 46°C, which is achieved by scaling the normalized quiescent E-field as described earlier. The two hot spots 122 and 124 are quantified in the $z=0$ temperature pattern cut shown in FIG. 30, and have a peak temperature at each hot spot of approximately 41°C. The temperature profile for $x=0$ in FIG. 31 shows no hot spots. As any undesired hot spot is a potential source for compromising the therapy

-63-

session, adaptive nulling is used to reduce the sidelobes corresponding to the hot spots.

FIG. 32 shows the simulated two-dimensional thermal distribution at time $t=20$ minutes, with adaptive nulling at four auxiliary probes 112_1 through 112_4 in effect. The focal-spot diameter at focus 107 with adaptive nulling is equivalent to the focal-spot diameter before adaptive nulling, shown in FIG. 29. Hot spots on the left and right sides of the target 106 are eliminated. FIG. 33 shows a comparison of the temperature distribution before (solid line) and after (broken line) nulling along the major axis ($z=0$) of the target ellipse 106. Similarly, FIG. 34 shows the temperature distribution before (solid line) and after (broken line) nulling along the minor axis ($x=0$) of the target ellipse 106.

The convergence of the previous thermal simulations was verified by increasing the density of E-field observation probe positions by a factor of two, with a new spacing between points of 0.9525 cm, still with a 41 X 41 grid. The ring array operates as before at 120 MHz, and there are four auxiliary probes 112_1 through 112_4 laid out as shown in FIG. 17. As the auxiliary positions are the same, the adaptive weights and channel correlation matrix eigenvalues in FIGS. 27 and 28, respectively, remain the same. From the parameter values in Table 1, all resistors $R_{i,j}$ in the finer-grid muscle-tissue phantom had a value of 193.0°C/W and all resistors $R_{i,j}$ in the water bolus had a value of 174.4°C/W . The value of the capacitors C_i in the phantom muscle-tissue is $2.95 \text{ J}/^\circ\text{C}$. Again, a constant temperature of 10°C is enforced at each water-bolus node. The E-field scaling factors to raise the focal-point temperature to 46°C before and after nulling are 76.5 dB

-64-

and 78.4 dB, respectively. The finer-grid two-dimensional thermal distributions before and after nulling are shown in FIGS. 35 and 34, respectively. Although the temperature contours are smoother, the general agreement
5 between these patterns and the coarser-grid patterns in FIGS. 29 and 32 are evident. Similarly, one-dimensional thermal pattern cuts with the finer grid are shown in FIGS. 37 (x axis) and 38 (z axis), and good agreement with the coarse-grid patterns of FIGS. 33 and 35, respectively,
10 is observed. In particular, the finer detail in FIG. 37 shows that the hot spots 122 and 124 are at approximately 42°C compared to 41°C observed for the coarse grid of FIG. 33. Thus, convergence of the coarse-grid thermal patterns is demonstrated.

15 Elliptical Array

An elliptical phased-array hyperthermia applicator, having a 70 cm major axis and a 60 cm minor axis, was also analyzed by computer simulation. The computer simulation parameters were the same as those applied to the analysis
20 of the annular array. Generally, the computer simulations show that reduced hot spot temperatures are observed along the major axis of the elliptical phantom, without adaptive nulling, while small increases in hot spot temperatures occur along the minor axis. Certain tumor geometries may
25 be heated more efficiently with an elliptical array than with an annular array.

EXPERIMENTAL RESULTS

Experimental data have been gathered from a commercial annular phased-array hyperthermia system
30 modified to perform a gradient search algorithm to produce an adaptive null (or focus) at one or more auxiliary E-field probe positions. The results confirm that a strong

-65-

null can be formed at the surface of the target body without significantly affecting the power delivered at the focus of the hyperthermia system.

FIG. 39 shows a cross-sectional view of the experimental system 700, which is a modified BSD-2000 SIGMA-60 annular phased-array hyperthermia applicator, available from BSD Medical Corporation, Salt Lake City, Utah. The annular array antenna 702 of the system is 59 cm in diameter and includes eight uniformly spaced dipole antennas 704₁ through 704₈, excited with a four channel transmitter at 100 MHz. Each of the four transmit channel signals are distributed by separate coaxial cables from the hyperthermia controller (not shown) to a two-way power divider having two outputs. The two outputs of each two-way power divider drive a pair of dipole antenna elements through a pair of coaxial cables.

A cylindrical phantom target body 706 is supported by a patient sling 705 which centrally locates the phantom within the annular array so that the longitudinal axes of the phantom and the annular array correspond to each other. Phantom target 706 is a 28 cm diameter X 40 cm long polymer bottle filled with saline solution (0.9% NaCl), which simulates a human subject. A deionized water-filled bladder 705 provides a water bolus between the annular array and the target phantom.

Single Adaptive Null

Three E-field probes are used to monitor the amplitude of the E-field at various sites in and around the phantom for this experiment. The first E-field probe 715 (BSD Medical Corp. Model EP-500) is located inside the phantom at the center, or focus, 707 of the array which simulates the tumor site. This probe monitors the

-66-

amplitude of the E-field at the tumor site as the null is formed at the null site. The second E-field probe 720 (BSD Medical Corp. Model EP-100) is taped onto the outside surface of the phantom at the desired null location which
5 simulates an E-field probe taped to a patient's skin. The probe is used to monitor the amplitude of the E-field at the null site as the null is formed by the gradient search algorithm. The third E-field probe 721 (BSD Medical Corp. Model EP-400) is taped onto the outside surface of the
10 phantom diametrically opposite the location of the null site probe 720. This probe is used to monitor the amplitude of the E-field away from the null and focus sites and provides an E-field amplitude reference for the experiment.

15 The transmit array amplitude and phase control software and the electric field probe monitoring software supplied with the BSD-2000 system were modified to incorporate a gradient search feedback routine for adaptive nulling and adaptive focusing. Pascal source
20 code listings and sample output of the adaptive nulling and focusing gradient search feedback routines are attached hereto as Appendices C and D, respectively.

Fig. 40 graphically illustrates the results of this experiment, showing the measured E-field probe amplitude, in dB, versus the gradient search iteration number. The
25 dB values are obtained by computing $10\log_{10}(\text{probe output signal})$ and normalizing the resulting values to 0 dB at iteration 0. It is evident from this graph that the gradient search formed a strong E-field amplitude null at
30 the null site, on the order of -15 to -20 dB with respect to the reference site, in less than 50 iterations. (The apparent rise in the E-field amplitude at the null site

-67-

between iterations 45 and 50 is most likely due to noise associated with the convergence calculations).

Furthermore, the measured E-field amplitude at the tumor site was reduced by no more than -5 dB with respect to the initial reference level. Fig. 41 shows a graphic illustration of the power, in dB, calculated at the null site versus gradient search iteration. It is evident from this graph that the gradient search causes the null site power to monotonically decrease with each iteration, achieving an approximately 12 dB reduction in power within 50 iterations.

It should be noted that for at least the first 30 iterations of the gradient search, there is good agreement between the computer simulations, presented above, and these experimental measurements. After approximately 30 iterations, however, the results of the computer simulations differ from the experimental measurements. One reason for this difference is that the computer simulations herein described do not attempt to accurately model all the characteristics of the BSD-2000 system used for the experiments. For example, the simulations do not account for phase shifter non-linearities, A/D convertor errors, or D/A convertor errors associated with the system which will affect the experimental measurements, especially at the relatively low signal levels present after 30 iterations. Thus, it is not expected that the computer simulations and the experimental results will necessarily behave the same where the signals or computations are most affected by measurement system noise.

-68-

Single Adaptive Null- Beef Phantom

Referring to Fig. 42, in another experiment, a single adaptive null was produced in a beef phantom 706' used in place of the saline phantom 706 of Fig. 39 to better simulate human tissue. Beef phantom 706' was a 24 lbs. hind leg cut having a front face width of 38 cm, a front face height of 23 cm and a thickness of 15 cm. The E-field probe positions used with the beef phantom are analogous to the E-field probe positions used with the saline phantom. That is, the first E-field probe 715' (BSD Medical Corp. Model EP-500) is located inside the beef phantom at the center, or focus, 707' of the array which simulates the tumor site. This probe monitors the amplitude of the E-field at the tumor site as the null is formed at the null site. The second E-field probe 720' (BSD Medical Corp. Model EP-100) is taped onto the outside surface of the beef phantom at the desired null location which simulates an E-field probe taped to a patient's skin. This probe is used to monitor the amplitude of the E-field at the null site as the null is formed by the gradient search algorithm. The third E-field probe 721' (BSD Medical Corp. Model EP-400) is taped onto the outside surface of the beef phantom diametrically opposite the location of the null site probe 720'. This probe is used to monitor the amplitude of the E-field away from the null and focus sites and provides an E-field amplitude reference for the experiment.

Fig. 43 graphically illustrates the results of the beef phantom experiment, showing the measured E-field probe amplitude, in dB, versus the gradient search iteration number. Again, the dB values are obtained by computing $10\log_{10}(\text{probe output signal})$ and normalizing the

-69-

resulting values to 0 dB at iteration 0. It is evident from this graph that the gradient search formed a strong E-field amplitude null at the null site 720', on the order of -18 to -20 dB with respect to the reference site, in less than 50 iterations. Furthermore, the E-field amplitude at the tumor site was reduced by no more than -2 dB with respect to the initial reference level. It should be noted that these results are very similar to the results obtained with the saline phantom (Fig. 40).

Fig. 44 shows a comparison between the temperature rise at the beef phantom tumor site 707' and the null site 720' during nulling. A thermocouple probe was located at each of the tumor and null sites, and the RF power was applied in four intervals of 15 minutes power on and 5 minutes power off for a total experiment time of 80 minutes. The gradient search performed 10 iterations during the 15 minute power on portion of each interval. Temperature measurements were taken during the 5 minute power off portion of each interval, i.e., one measurement for each 10 iterations. The experimental data shows that the tumor site was initially at about 26°C and the null site was initially at about 27°C before applying RF power. After 40 minutes (30 minutes power on and 10 minutes power off) the temperature of the tumor site has risen 4°C to about 30°C, while the null site has risen only 1°C to about 28°C. After 80 minutes (60 minutes power on and 20 minutes power off) the temperature of the tumor site has risen 8°C to about 34°C, while the temperature of the null site has risen only 3°C to about 30°C. Thus, an approximate differential of about 4°C is attained between the tissue temperature of a deep-seated target and the

-70-

temperature of a single surface null site in a beef phantom.

Two Adaptive Nulls

In another experiment, two adaptive nulls on the surface of the saline-filled cylindrical phantom were generated and measured. This experiment used the same configuration as shown in Fig. 39 with the one E-field probe 715 (BSD Medical Corp. Model EP-500) located inside the phantom 706 at the center, or focus, 707 of the array simulating the tumor site. Two E-field probes 720 and 721 (BSD Medical Corp. Model EP-100) were located on the outside surface of the phantom at diametrically opposite positions representing the two non-invasive null sites. Probe 715 monitored the E-field amplitude at the tumor site while probes 720 and 721 monitored the E-field amplitude at the null sites.

FIG. 45 graphically illustrates the results of this experiment, showing the measured E-field probe amplitude, in dB, versus the gradient search iteration number. Again, the dB values are obtained by computing $10\log_{10}(\text{probe output signal})$ and normalizing the resulting values to 0 dB at iteration 0. It is evident from this graph that the gradient search formed two strong adaptive E-field amplitude nulls at the null sites, on the order of -10 to -20 dB with respect to the reference site, in about 50 iterations. In particular, at iteration number 50 the null strength at probe 720 (probe site 2) is approximately -18.0 dB and the null strength at probe 721 (probe site 3) is approximately -11.8 dB. Furthermore, the E-field amplitude at the tumor site 715 (probe site 1) was held

-71-

close to a constant value (0 dB) throughout the 50 iterations.

Adaptive Focusing

In another experiment, adaptive phase focusing was used to maximize the E-field amplitude at a selected location different from focus 707 of the saline-filled cylindrical phantom 706 of FIG. 39. In this case, the selected focus site was at E-field probe 720 (BSD Medical Corp. Model EP-100) located on the outside surface of the cylindrical phantom.

FIG. 46 graphically illustrates the results of this experiment, showing the measured E-field probe amplitude, in dB, versus the gradient search iteration number for 30 iterations. Again, the dB values are obtained by computing $10\log_{10}(\text{probe output signal})$ and normalizing the resulting values to 0 dB at iteration 0. The initial phase weights applied to the transmit elements of the array were equal, nominally producing an E-field focused at the center of the array 707. The gradient search was used to adjust the phases of the array transmit weights to maximize the E-field amplitude at probe site 720, i.e., refocus the array at probe 720. The transmit weight amplitudes were held constant over the 30 iterations. As shown, the gradient search converged in about 10 iterations and the power at probe 720 increased by about 0.9 dB compared to its initial value. This result demonstrates that adaptive focusing can be used successfully to optimize the peak power delivered to a tumor site.

30 Clinical Application

-72-

A modified BSD-2000 Sigma 60 system can be used as a clinical adaptive hyperthermia system for implementing the adaptive nulling and focusing techniques of this invention. An unmodified BSD-2000 hyperthermia system
5 uses four transmit channels to energize the eight transmit elements (in pairs) of the annular array, and eight EP-400 (or EP-100) non-invasive E-field probes to monitor clinical hyperthermia treatments. The eight E-field probes can provide feedback signals to the controller
10 performing the adaptive nulling and/or focusing algorithms. Theoretically, three independent adaptive nulls (and/or peaks) can be formed by adaptively adjusting the phases and gains of the four transmit channels. Any three of the eight E-field probes can provide the feedback
15 signals required to produce a null (or peak) at the corresponding probe.

Various treatment protocols are possible for selecting desired null sites, depending on the particular patient and case history. One protocol would place the
20 eight E-field probes around the circumference of the patient to measure the E-field strength at each probe before nulling and thereby identify the strongest electric fields on the surface of the patient indicating potentially serious hot spots. Adaptive nulling would
25 then be applied to minimize the electric field at the three probes having the strongest electric fields before nulling. Alternatively, if the patient can localize a painful hot spot during treatment, adaptive nulling would be applied to minimize the electric field at the E-field
30 probe closest to the identified hot spot.

The number of adaptive nulls required will vary with patient and pathology. In some situations it is possible

-73-

that more than three independent adaptive nulls will be required to achieve a therapeutic thermal distribution in the patient. In such a case, an extension of the four transmit channel BSD-2000 system to an eight transmit
5 channel configuration will allow up to seven independent adaptive nulls and an adaptive focus to be formed.

MONOPOLE ARRAY EMBODIMENT

FIGS. 47-49 show an embodiment of a non-invasive RF
10 monopole phased-array hyperthermia system 400 for treating malignant brain tumors. Hyperthermia system 400 features a monopole phased-array transmit antenna 402 having a plurality of monopole transmit antenna elements 404 placed in proximity to the cranium 406 of a patient to be treated
15 for a malignant brain tumor 407. Hyperthermia system 400 also features improved focusing characteristics through using one or more non-invasive electric field probes 412 placed on or near the patient's cranium, in conjunction with the near-field adaptive focusing and nulling
20 apparatus and methods of this invention.

Monopole phased-array 402 is used to therapeutically heat the brain tumor 407, typically located 1-3 cm below the skin surface of the cranium 406, by adaptively focusing the RF electric field energy radiated by the
25 monopole radiator elements 404 into the tumor 407. In practice, it is dangerous, and often impossible, to invasively place an E-field probe into the brain tumor site to facilitate adaptive focusing of the RF energy into the tumor. "Hot spots" are not typically a problem with
30 the monopole hyperthermia array described since the side lobes generated by a phased-array in this near-field geometry are much lower than those generated by the

-74-

annular phased-array described above. Thus, the monopole phased-array receives its major benefit by applying the adaptive focusing of this invention to more precisely focus energy into the tumor site. However, the adaptive
5 nulling of this invention may also be used if "hot spots" do develop through the use of the monopole array.

The monopole phased array antenna 402 is mounted inside an water-tight enclosure 430 having a generally circular top and bottom surface 432 and 434, respectively,
10 and a cylindrical or conical side surface 436 connecting the top and bottom surfaces. The enclosure is made from non-conductive plastic material, such as plexiglas, but may also be fashioned from any material which acts as an electrical insulator and will not interfere with the RF
15 radiation patterns generated by the monopole phased-array inside the enclosure.

The bottom surface 434 has a central elliptical aperture 438 which accommodates a portion of the patient's cranium 406 to allow tumor 407 to be disposed within the
20 interior of enclosure 430 adjacent to the monopole phased-array 402. A flexible silicone rubber membrane 440 covers the aperture to maintain the water-tight integrity of the enclosure. The enclosure 430 can be filled with chilled de-ionized water 442 for cooling the patient's skin during
25 hyperthermia treatment. The de-ionized water can be temperature controlled and circulated through the enclosure 430 to maximize the cooling effect.

Bottom surface 434 also includes an RF conducting ground plane 444 mounted co-planar with the bottom surface
30 and which acts as an RF reflector for monopole antenna elements 404. This ground plane may be fashioned out of a metal sheet, metal foil, metal mesh, or any other RF

-75-

conductive material which can be fashioned to cover the area of bottom surface 434. The ground plane may also be imbedded into the bottom surface by, for instance, laminating the ground plane between two layers of
5 insulating material.

The monopole radiator elements 404 are each mounted perpendicularly onto bottom surface 434 so that they may be energized from outside the enclosure, yet remain insulated from the ground plane 444. In one preferred
10 embodiment, each monopole radiator element 404 is a $1/4$ wavelength long straight wire radiator threadably attached on one end into a connector mounted onto surface 434 and insulated from ground plane 444. It is understood that another form of a monopole antenna element, other than a
15 straight wire radiator, can also be used. For instance, helical monopole, conical monopole, and sleeve monopole antenna elements are also appropriate for use as monopole array elements of the present invention.

Each monopole element is energized through a coaxial
20 cable fed through the bottom surface 434 to the connector. The bottom surface may also be provided with extra monopole connectors which allow repositioning of the monopole radiator elements within the enclosure. Repositioning allows the user to change the geometry of
25 the monopole phased-array antenna as well as position the antenna adjacent to the tumor location to maximize the therapeutic effect.

An RF reflecting screen 446 (FIGS. 48 and 49) can be placed behind the monopole antenna elements 404 to direct
30 more of the radiated RF energy toward the cranium, i.e., energy which would otherwise be lost through the side of the water-tight enclosure. Reflecting screen 446 is

-76-

typically positioned in the water bolus approximately $1/4$ wavelength behind the monopole antenna elements and has a cylindrical reflecting surface extending perpendicularly from the ground screen to a height of approximately twice the wavelength of the radiated energy. Alternatively, the reflecting surface of the screen can be curved toward the target to further enhance radiation of the target. The reflecting screen is constructed from high frequency RF conducting mesh which allows water to freely flow through it, and is electrically connected to the ground screen using good high frequency RF construction practices.

Each monopole radiator element 404 is configured as a $1/4$ wavelength radiator to resonate at approximately 915 MHz which is effective for heating tumors 1 to 3 cm, or more, beneath the surface of the patient's skull. The monopole phased-array can include a varying number of radiator elements spatially arranged in a variety of patterns. The spacing between the monopole antenna elements is typically between $1/2$ to 1 wavelength. Furthermore, the number and location of the non-invasive electric field probes 412 can also vary depending on the hyperthermia focusing patterns desired.

In the adaptive hyperthermia monopole phased-array of this invention, non-invasive E-field probes are used in conjunction with the adaptive focusing apparatus and techniques of this invention to maximize the RF power delivered to the tumor site inside the cranium. Computer simulations, presented herein, show that the optimum focused (e.g., with an invasive E-field probe) phased array can produce an RF energy pattern with maximum electric field strength at the tumor site and no undesired hot spots within the cranial target.

-77-

With the adaptive hyperthermia monopole phased-array described herein, RF energy peaks are adaptively formed to maximize the electric field energy delivered to the target focus. As shown, the focused energy peak achieved by the adaptive focusing apparatus of this invention is invasive
5 to the cranial target extending into the tumor region.

Referring to FIG. 50, the adaptive-focusing monopole phased-array hyperthermia system of this invention can be described in terms corresponding to the generalized
10 annular phased-array system schematic diagram of FIG. 6. Specifically, monopole transmit elements 404_n of hyperthermia transmitting antenna array 402 correspond respectively to the dipole transmit elements 104_n of annular phased array applicator 102 of FIG. 6.

15 Furthermore, the plurality of E-field auxiliary probes 412_m , correspond to the E-field probes 112_m of FIG. 6. It is apparent that the monopole phased-array hyperthermia system herein described does not take advantage of an electric field probe placed at the tumor 407, analogous to
20 the receiving probe 115 used with the annular phased array applicator 102 of FIG. 6, to maximize the focus radiated energy into the tumor. Use of a probe at the focus would in most cases require a surgical procedure to invasively place the probe within the patient's brain.

25 The receiver 114, signal processor 116, RF source 108, and weighting functions 110_n (FIG. 6) operate with the monopole array as described above with regard to the annular array, except that the signal processor 116 performs an adaptive focusing algorithm described below, which is related to the adaptive nulling algorithm. That
30 is, signal processor 116 performs either a sample matrix inversion (SMI) algorithm or a gradient search algorithm

-78-

on the signals output from receiver 114 and updates the adaptive array weights w_n (with gain g and phase ϕ) to rapidly (within seconds) focus energy at the tumor 407.

Referring to FIGS. 51 and 52, there is shown an
5 analytical model of an embodiment of an eight-element, 915
MHz hyperthermia monopole phased-array 402 of FIG. 47.
Phased-array 402 has transmit antennas 404_1 through 404_8 ,
arranged adjacent to an elliptical phantom target 406
representing the cross section of the human cranium at the
10 tumor level. The focus 407 of the elliptical phantom
models the location, approximately 2.0 cm below the
surface of the cranium, of the brain tumor to receive
hyperthermia treatment, i.e., the focus of RF energy for
the phased array 402. Water bolus 442 is assumed to
15 surround the target body 406, and is treated as a
homogeneous medium for analysis purposes.

The monopole radiator elements 404_1 through 404_8 are
arranged as a 120° circular arc array of uniformly spaced
elements having a constant radius of 12.7 cm relative to
20 the geometric center of the cranium C, i.e., at $x = 0.0$
cm, $z = 0.0$ cm. The tumor site, or focus 407 of the RF
energy, is assumed to be at $x = 0.0$ cm, $z = 5.08$ cm for
simulation purposes. (In an alternative preferred
embodiment the monopole array elements form a circular arc
25 having a geometric center at focus 407 (target) rather
than at the center of the cranium C. This has the
advantage that less phase focusing should be required to
maximize the energy delivered to the focus, and thus the
required number of gradient search iterations is reduced.)

30 Six auxiliary RF E-field probes, or sensors, 412_1
through 412_6 (i.e., receiving antennas) are placed on and
near the perimeter of the elliptical target to model non-

-79-

invasive E-field probes placed on and near the skin of the cranial target. Auxiliary probes 412_1 , 412_2 , and 412_3 are uniformly spaced in an arc row, between the arc array and the cranial target, having a constant radius of approximately 4.0 cm relative to the desired focus 407. Auxiliary probes 412_4 , 412_5 and 412_6 are placed on the target skin adjacent to focus 407. Specifically, the first arc row of electric field probes 412_1 through 412_3 may be denoted as probes L_1 , M_1 , and R_1 , respectively, and the row of electric field probes 412_4 through 412_6 may be denoted as probes L_2 , M_2 , and R_2 , respectively. The electric field probes are arranged so that corresponding probes on the two rows are located along a radial line extending from the desired focus at tumor site 407 and are spaced $1/4$ to $1/2$ wavelength apart. That is, probe pair (L_1, L_2) is located along radial r_L , probe pair (M_1, M_2) is located along radial r_M and, probe pair (R_1, R_2) is located along radial r_R .

The gains and phases of the monopole elements are adaptively adjusted as described below to focus the energy output from the monopole phased-array into the tumor site 407 located several centimeters below the surface of the cranium. From the phased-array geometry of Fig. 52 it is observed that an electric field focused at tumor 407 will be balanced and symmetric with respect to the line $x=0$. Furthermore, the electric field is attenuated in the water bolus external to the cranium in the direction away from the transmit array. To achieve a focus interior to the cranium at the tumor site 407 it is assumed that the amplitude difference between the electric field adjacent to the skin surface of the cranium and the field approximately one quarter wavelength exterior to the skin

-80-

surface of the cranium must be constrained to a desired value. This desired value is typically a minimum to avoid "hot spots" on the skin surface. Similarly the amplitude of the electric field in the transverse direction should
 5 be balanced to minimize the electric field variation between the left and right electric field probes with respect to the middle electric field probes, i.e., maintain electric field symmetry with respect to the x-axis. The electric field differences in the radial
 10 direction may be denoted by

$$\Delta A_{L12} = |A_{L1} - A_{L2}| \quad , \quad (74)$$

$$\Delta A_{M12} = |A_{M1} - A_{M2}| \quad , \quad (75)$$

$$\Delta A_{R12} = |A_{R1} - A_{R2}| \quad . \quad (76)$$

where A denotes the amplitude of the electric field measured by the specified field probe, \hat{p} is a unit vector in the radial direction which bisects the transmit monopole array and \hat{t} is a transverse unit vector as shown
 15 in FIG. 52. The electric field differences in the transverse direction for the first row may be denoted by

$$\Delta A_{LM1} = |A_{L1} - A_{M1}| \quad , \quad (77)$$

and,

$$\Delta A_{RM1} = |A_{R1} - A_{M1}| \quad , \quad (78)$$

-81-

and the electric field differences in the transverse direction for the second row may be denoted by

$$\Delta A_{LM2} = |A_{L2} - A_{M2}| \quad , \quad (79)$$

and,

$$\Delta A_{RM2} = |A_{R2} - A_{M2}| \quad . \quad (80)$$

A figure of merit F can be defined as

$$F = \alpha (\Delta A_{L12} + \Delta A_{M12} + \Delta A_{R12}) + \Delta A_{LM1} + \Delta A_{RM1} + \Delta A_{LM2} + \Delta A_{RM2} \quad , \quad (81)$$

5 where α is a scale factor used to adjust the effect of the electrical field gradient caused by attenuation in the radial direction between the phased-array antenna and the target. The figure of merit F involves seven constraints which are easily taken into account by the eight transmit
10 element phased-array described. The gradient search algorithm described above is used to minimize the figure of merit F .

FIG. 53 shows a simulated two-dimensional quiescent radiation pattern in the plane $y=0$ for the eight element
15 monopole arc array of FIG. 52 operating at 915 MHz before adaptive focusing, i.e., with uniform amplitude and phase illumination. This radiation pattern was calculated using the moment-method described above, and the calculations assume an infinite homogeneous conducting medium
20 simulating phantom brain tissue, i.e., $\epsilon_r=50.0$, $\sigma=1.3$. The focus of the array is at $x=0.0$, $z=5.0$ cm. The

-82-

positions of the eight monopole radiators 404₁ through 404₈ are clearly evident by the -10 dB contours surrounding each element. The radiation pattern is symmetric because of the symmetry of the array and the
5 assumed homogeneous medium.

FIG. 54 shows the quiescent radiation pattern of FIG. 53 cut at $z=5.0$ cm, which is through the tumor site 407 assumed to be at $x=0.0$, $z=5.0$ cm. The focused main beam is centered at $x=0.0$ as desired. The half-power beamwidth
10 is approximately 2.0 cm, which is close to $1/2$ wavelength for the full ring array.

FIG. 55 shows a simulated two-dimensional thermal pattern expected for the quiescent radiation pattern of FIG. 53 at time $t=20$ minutes. This simulation assumes
15 that the elliptical phantom brain tissue is surrounded by a 10°C constant temperature water bolus and that the initial temperature of the brain tissue phantom is 25°C.

FIG. 56 shows a configuration of the monopole phased-array hyperthermia system of this invention configured to
20 uniformly heat a large intra-cranial tumor target 407'. In this case, a set of auxiliary E-field probes 412 are uniformly spaced along the skin surface of the cranium between the monopole radiator elements 404 and the tumor site 407'. Here, seven E-field probes 412₁ through 412₇
25 are used, denoted P_1 through P_7 respectively, but the quantity of probes required will vary according to the tumor size and location. The gains and phases of the monopole elements are adaptively adjusted to uniformly distribute the electric field energy at the E-field probes
30 412₁ through 412₇. From the geometry of FIG. 56 it is observed that a uniform electric field at the E-field

-83-

probes will produce a substantially uniform electric field inside tumor 407' to induce uniform heating of the tumor.

To achieve a uniform electric field distribution across all the E-field probes, and thus uniform heating of the tumor 407', the amplitude difference between any two adjacent E-field probes on the skin surface of the cranium must be minimized. The electric field differences between adjacent E-field probes may be written as

$$\Delta A_{P12} = |A_{P1} - A_{P2}| \quad , \quad (82)$$

$$\Delta A_{P23} = |A_{P2} - A_{P3}| \quad , \quad (83)$$

$$\Delta A_{P34} = |A_{P3} - A_{P4}| \quad , \quad (84)$$

$$\Delta A_{P45} = |A_{P4} - A_{P5}| \quad , \quad (85)$$

$$\Delta A_{P56} = |A_{P5} - A_{P6}| \quad , \quad (86)$$

and,

$$\Delta A_{P67} = |A_{P6} - A_{P7}| \quad , \quad (87)$$

10 where A denotes the amplitude of the electric field measured by the specified field probe. A figure of merit F may be defined as

$$F = \Delta A_{P12}^2 + \Delta A_{P23}^2 + \Delta A_{P34}^2 + \Delta A_{P45}^2 + \Delta A_{P56}^2 + \Delta A_{P67}^2 \quad . \quad (88)$$

The figure of merit F involves six constraints on measured differences and an additional constraint on total power
15 radiated by the transmit array, all of which are easily

-84-

taken into account by the eight transmit element phased-array described. The gradient search algorithm described above is used to minimize the figure of merit F and thereby achieve a uniform electric field distribution across the E-field probes.

It should be noted that this approach for achieving a uniform electric field distribution to effect uniform heating within a large mass is not limited to the monopole array heating of a brain tumor, and for example can be similarly implemented with the annular phased-array hyperthermia applicator of FIG. 1 for uniformly heating a large mass in other areas of the body.

FIGS. 57 and 58A show an alternative preferred embodiment of the monopole phased array applicator 400 of FIG. 48 including the addition of a top ground plane surface 450 positioned above the monopole antenna elements 404_n and extending from the reflecting screen 446 toward the target body parallel to ground plane surface 442. The top ground plane surface 450 combines with ground plane surface 442 to form a parallel plate waveguide region 452 between the monopole antenna elements and the target body 406. The spacing between the parallel plates (i.e., between surfaces 442 and 450) can be used to adjust the radiation pattern in the direction perpendicular to the parallel plates. The spacing between the parallel plates is typically between 1/2 and 5 wavelengths. FIGS. 58B and 58C show alternative preferred embodiments of the parallel plate waveguide of FIG. 58A having non-parallel waveguide surfaces, and flared waveguide surface forming a horn, respectively.

FIG 59 shows a preferred embodiment of a stacked waveguide phased array applicator having multiple stacked

-85-

parallel plates 450, 454, and 456 forming respective stacked waveguide regions 452, 458, and 460, each having a corresponding set of monopole phased array antenna elements 404_n , $404_n'$, $404_n''$.

5 FIG. 60 shows a block diagram of a preferred embodiment of a 915 MHz transmit and receive (T/R) module 800 for use with the monopole phased array hyperthermia system 400 (FIG. 47), specifically for use in transmit amplifier/phase shift network 110 of FIG. 50. Generally,
10 the T/R module 800, as well as the monopole hyperthermia system 400, is not restricted to operate at 915 MHz, and is adaptable for operation anywhere within the industrial, scientific, medical (ISM) frequency band of 902 to 928 MHz.

15 The transmit function of the T/R module 800 is used to energize a monopole transmit antenna element 404_n (FIG. 50) of the monopole hyperthermia array 402 with a 915 MHz signal, having controlled phase and gain, for the purposes of heating the target 407. Each monopole transmit antenna
20 element 404_n of the array 402 is connected to a corresponding T/R module and therefore the quantity of T/R modules required depends on the quantity of monopole antenna elements 404_n in the array.

 With regard to the generation of the 915 MHz transmit
25 signal, having controlled phase and gain, a tunable oscillator 802, tunable from 180 to 206 MHz, is used to produce a transmit signal having a 193 MHz center frequency. The 193 MHz transmit signal is input to a dual-stage voltage-variable attenuator 804 which covers an
30 attenuation range of 0 to -40 dB (-60 dB off state) determined by a 12 bit analog control voltage. The other port of mixer 808 is driven with a constant frequency 1108

-86-

MHz phase-controlled signal generated by a phase-controlled local oscillator 810.

Phase-controlled local oscillator 810 is excited with a 277 MHz signal generated by a fixed frequency local oscillator 812. The output of the 277 MHz local oscillator 812 is input to a voltage-variable phase shifter which shifts the phase of the 277 MHz signal from 0 to 90°, determined by a 12 bit analog control voltage. The phase-shifted 277 MHz signal is input to a X4 frequency multiplier 816 which quadruples the signal to 1108 MHz and extends the phase control range to 0 to 360°. The output of the frequency multiplier passes through a 1108 MHz bandpass filter 818, having a 50 MHz bandwidth, to remove undesired harmonics. The 1108 MHz output of the bandpass filter is then amplified to saturation by an amplifier 820 to produce a relatively constant input power to the input port of mixer 808 independent of the commanded phase shift.

The upconverted, gain and phase-controlled 915 MHz signal output from mixer 808 passes through a 915 MHz bandpass filter 822, having a 50 MHz bandwidth, to remove undesired harmonics generated in mixer 808. The output signal of bandpass filter 822 passes through another T/R switch 824 which, when in the transmit position (T), connects the bandpass filter output signal to drive the input of a power amplifier 826 having an average CW output power of up to, or greater than, 100 watts. The output signal of the power amplifier 826 passes through another T/R switch 828 which, when in the transmit position (T), connects the amplified 915 MHz transmit signal to the input of another 915 MHz bandpass filter 830, having a 50 MHz bandwidth, which removes unwanted harmonics generated

-87-

in the power amplifier. Finally, the 915 MHz transmit signal output from bandpass filter 830 is connected by a transmission line 832 to a monopole antenna element 404_n of the monopole hyperthermia array 402.

5 The receive function of the T/R module 800 can be used for passive microwave radiometry for non-invasively sensing the temperature of the target tissue 407 (FIG. 50) with the monopole antenna elements 404_n of array 402. To operate in a non-invasive microwave radiometry mode, the
10 transmit power is turned off as desired for a period of several seconds during which the elements of the monopole hyperthermia array act as passive receive antennas.

In this case, the three T/R switches 806, 824, and 828 are set to the receive (R) position. The 915 MHz
15 center-frequency passive signal received by the monopole antenna element 404_n is filtered by bandpass filter 830, amplified by a low-noise amplifier 834, and again filtered by bandpass filter 822. The output of bandpass filter 822 is mixed with the 1108 MHz controlled-phase local
20 oscillator signal by mixer 808, the output of which is input to a lowpass filter 836. Lowpass filter 836 has a 350 MHz high frequency cutoff which provides a 193 MHz center frequency receive signal for input to a second mixer 838. A variable frequency local oscillator, tunable
25 over a 150-176 MHz range, has an output signal tuned to 163 MHz which is amplified by an amplifier 841 and input to another port of mixer 838 to mix with the 193 MHz center frequency receive signal. The output of mixer 838 contains a 30 MHz center frequency receive signal which is
30 input to a 30 MHz bandpass filter 842, having a 5 MHz bandwidth, to remove unwanted out of band signals. The filtered 30 MHz center frequency receive signal is then

-88-

passed through a voltage controlled 0 to -40 dB attenuator 844 whose output signal 846 is controlled by a 12 bit analog voltage level.

The 30 MHz center frequency receive signal 846 can be
5 analyzed with a commercial network analyzer, such as a Hewlett Packard 8510 analyzer, or can be combined with the output of the other T/R modules (i.e., receive signals from the other monopole antenna elements) in a commercial analog power combiner at the 30 MHz frequency.

10 Alternatively, the 30 MHz receive signal 846 can be mixed with a 28.5 MHz local oscillator and downconverted to a baseband offset frequency of 1.5 MHz. The resulting baseband signal is lowpass filtered with a cutoff frequency of 2.0 MHz, and sampled with a high speed
15 digital to analog convertor at 4.5 MHz (i.e., above the Nyquist sampling limit for the bandlimited signal). The frequency spectrum of the baseband signal is then computed using digital signal processing techniques (see, J.R. Johnson, et al., "An Experimental Adaptive Nulling
20 Receiver Utilizing the Sample Matrix Inversion Algorithm with Channel Equalization", IEEE Transactions on Microwave Theory and Techniques, Vol. MTT-39, No. 5, pp. 798-808, May 1991). It should further be noted that the T/R module 800 can be used as a receiver 114 (FIG. 50) for the E-
25 field probes 412 if the low-noise amplifier 834 is bypassed.

MONOPOLE ARRAY FOR TREATMENT OF BREAST CARCINOMAS

Figs. 61-63 show an embodiment of a minimally
invasive RF monopole phased array hyperthermia waveguide
30 applicator 500 for treating malignant breast tumors. Hyperthermia applicator 500 features a monopole phased array transmit antenna 402 having a plurality of monopole

-89-

transmit antenna elements 404_n mounted through a conducting ground plane 502. Applicator 500 includes a second conductive ground plane 504 mounted parallel to ground plane 502 and above monopole antenna elements 404.

- 5 A conducting backscreen 506 is uniformly spaced from monopole antenna elements 404_n and connects ground plane 502 to ground plane 506 to form a waveguide around phased array antenna 402. Together, ground planes 502, 504, and conducting backscreen 506 form a semi-cylindrical
- 10 waveguide applicator having an aperture 508 through which RF energy from monopole phased array transmit antenna 402 is directed.

- In the embodiment of applicator 500 shown in Figs. 61-63, phased array transmit antenna 402 includes, eight
- 15 monopole transmit elements $404_1 - 404_8$ spaced 2.54 cm apart along 120° of a circular arc 514 having a constant radius $R_a = 8.66$ cm. The monopole array is configured as a phased array antenna radiating coherently at 915 MHz, with the length of each monopole element is 1.27 cm (0.34
- 20 λ). Conducting backscreen 506 traverses a semicircular arc, spaced from monopole antenna elements 404_n , having a constant radius $R_b = 9.32$ cm. This geometry results in a backscreen- to-monopole spacing of 0.66 cm (0.18λ). The length of each monopole element 404_n is 1.27 cm (0.34λ)
- 25 and the monopole cylindrical wire diameter is 0.13 cm. The parallel ground plane spacing between ground plane 502 and ground plane 506 is 2.5 cm. These dimensions result a waveguide aperture 508 having width $w = 18.6$ cm and height $h = 2.5$ cm.

- 30 Fig. 64 shows the use of two applicators 500 to irradiate breast tissue to produce hyperthermia during treatment. The breast to be treated 520 is compressed

-90-

between two compression plates 522 spaced a distance
s = 4.0 to 5.0 cm apart, which is compatible with typical
mammography systems. An electric field probe 533, which
is the minimally invasive element of the applicator, can
5 be placed in the breast at the target 532 to assist in
focusing the energy from the monopole phased array
transmit antennae 402 into the target (as describe above),
e.g., by adjusting the phases of the monopole transmit
elements 404_n to maximize the energy received at the
10 electric field probe 533. A temperature probe can also be
used in conjunction with (or possibly in place of) the
electric field probe 533 for controlling the temperature
rise in the breast tissue. Additional electric field
probes and/or temperature sensors can be use in and around
15 the breast to further refine the hyperthermia heating
pattern generated by the applicators.

The monopole transmit elements 404_n are impedance
matched to the breast tissue by filling the applicator
waveguide cavity 524 surrounding the monopole transmit
20 elements 404_n of each applicator with low loss (0.3 dB/cm)
distilled water (dielectric constant $\epsilon_r = 80$, electrical
conductivity $\sigma = 0.19$ S/m, and wavelength $\lambda = 3.7$ cm at
915 MHz). The applicator can be made watertight with a
solid dielectric or flexible bolus covering the aperture.
25 Compression plates 522 are made from materials such as
plexiglass which has a low dielectric constant and low
electrical conductivity which is essentially transparent
to microwave energy.

The 915 MHz minimally invasive monopole phased-array
30 applicators of this invention can be used for heating
tumors in the female breast in an equipment configuration
similar to standard mammography systems and apparatus.

-91-

The hyperthermia treatment geometry involves the patient lying on a table in a prone position with the breast to be irradiated hanging through an opening in the table. This geometry is the same used in a typical needle biopsy procedure on the breast where a compression device is used in performing x-ray imaging (i.e., mammography).

The compressed breast tissue geometry is desirable for several major reasons. First, compressing the breast tissue to the range of about 4.0 to 5.0 cm allows more effective penetration of electric field energy into the breast for microwave heating of the tissue. In this case, the required depth of focusing in the tissue is only typically 2.0 to 2.5 cm. Second, the compression helps standardize the equipment used in treating patients. That is, a single applicator design could treat a wide range of breast sizes. Third, the compression device is very similar to that used in digital mammography breast biopsy equipment, leading to adaptation of the biopsy equipment for breast hyperthermia using the applicators of this invention. Thus, imaging techniques used for breast biopsy could also be used in accurately locating the tumor regions in the breast for visualization of the placement in the breast tissue of the electric field probe(s) and/or temperature sensor(s) of this invention.

Fig. 65 shows a breast phantom 530 used for measuring radiation patterns generated by two opposed hyperthermia applicators 500 positioned on opposite sides at the breast phantom 530 in a mirrored configuration. Breast phantom 530 was constructed as a box made from Lexan material having wall thicknesses of 0.3 cm, an inside dimension of 30 cm height, 30 cm length, and 4 cm width, which is equivalent to the expected compression thickness of the

-92-

compressed breast tissue. Breast phantom 530 is filled with liquid for simulating the dielectric characteristics of breast tissue at 915 MHz, and is composed of methanol, water, and salt, and has a relative dielectric constant of $\epsilon_r = 42$ and electrical conductivity of $\sigma = 0.7$ S/m, which was confirmed by dielectric probe measurements. At 915 MHz, the wavelength in the phantom tissue is calculated to be $\lambda = 5.0$ cm. The complex propagation constant is $\gamma = 20.1 + j126.0$ rad/m which gives an attenuation of 1.8 dB/cm. Complex wave impedance for the phantom is calculated to be $\eta = 56.0 + j8.9$ ohms. Transmit elements 404_n were coherently excited with 915 MHz RF energy to focus the energy at a desired focal point 532 located at a depth of 2 cm centered between the applicators 500.

Fig. 66 shows RF energy contours for the breast phantom of Fig. 65 as determined by an ideal computer simulation based on ray tracing. This contour shows the two dimensional electric field pattern established in the phantom in one dB increments over a 4 cm x 4 cm area, centered at focus 532 of the phantom. The computer simulated hyperthermic heating region is approximately 2.0 cm x 1.8 cm based on the 50% (-3 dB) specific absorption rate (SAR) level. This focused electric field pattern can be moved to a desirable region within the breast by means of the adaptive focusing techniques discussed above, or by placement of an invasive electric field probe at the appropriate focus location.

Fig. 67 shows measured data taken along the Y axis through the breast phantom of Fig. 65, and its relationship to simulated data calculated by computer along the same axis, shown in Fig. 66. In experiments used to gather these measurements, the monopole feed

-93-

cables were phased adjusted manually, with an invasive electric field probe placed inside the phantom at focus 532, to help produce a focused electric field at the desired position. The measured electric field radiation pattern versus depth along the Y axis shown in Fig. 67 shows a focused beam with peak radiation at approximately 2 cm depth, with lower electric field intensity at the surface of the breast. In the measured data, the beam width for SAR values greater than 50% indicated that a heating region approximately 2 cm long can be expected in the Y (depth) dimension. Near the left and right surfaces of the phantom, the small differences between the electric field measurements and simulated calculations are expected, due to the amplitude and phase errors present in the experimental set up of the microwave feed network driving the applicators and in the invasive electric field probe alignment within the phantom. Thus, the measurements are in good agreement with the ideal monopole phased array simulated data.

It should also be noted that the adaptive focusing and nulling techniques described in this application can be used with invasive and/or non-invasive RF probes to help tailor the generated RF energy profiles as desired. Furthermore, whereas a single monopole phased array can be electronically focused in azimuth, stacked monopole arrays (such as those shown in Fig. 59) can also be used to provide focusing and beam shaping in elevation. It should also be noted that frequencies other than 915 MHz can also be used.

Figs. 68 and 69 are simulated radiation patterns which show that radiation can be focused at positions within the breast tissue offset from the center 532

-94-

applicators 500 of the opposed monopole array. Figs. 70 and 71 show that a single monopole array applicator 500 can also be used to effectively focus radiation into the target, albeit with a pattern that achieves maximum energy density closer to the surface of the target tissue, rather than in the center of the target tissue.

EQUIVALENTS

While this invention has been particularly shown and described with references to preferred embodiments thereof, it will be understood by those skilled in the art that various changes in form and details may be made therein without departing from the spirit and scope of the invention as defined by the appended claims. For instance, although the hyperthermia systems described herein are with respect to a particular range of RF frequencies, the invention is applicable to hyperthermia systems operating from low frequencies to microwave frequencies. Some of the methods and techniques described herein are also applicable to ultrasound hyperthermia systems. It is also understood that larger or smaller numbers of antenna elements and electric field probes may be used with similar results. The invention is also applicable to non-medical hyperthermia systems, such as those used for industrial heating.

-95-

CLAIMS

1. A hyperthermia applicator for inducing a temperature rise in a human breast, comprising
a waveguide comprising an aperture and an electric field radiator coupled to a source of electric field energy for producing electric field radiation output from the waveguide through the aperture; and
compression means for compressing a human breast to a predetermined thickness, the waveguide being adapted to be disposed such that the compressed breast is positioned to receive electric field radiation from the waveguide.
2. The apparatus of Claim 1, wherein the electric field radiator comprises a phased-array of electric field transmit elements.
3. The apparatus of Claim 2, wherein the phased-array of electric field transmit elements comprises an array of monopole antenna elements.
4. The apparatus of Claim 3, wherein the waveguide comprises
a first RF reflecting groundplane surface for mounting the monopole antenna elements, wherein the monopole antenna elements are perpendicularly mounted to the same side of the RF reflecting ground plane,
a second RF reflecting groundplane surface disposed substantially parallel to the first RF reflecting groundplane such that the monopole antenna

-96-

elements are positioned between the first and second RF reflecting groundplanes, and

an RF reflecting screen mounted substantially perpendicular to the first and second RF groundplane surfaces and behind the monopole antenna elements to reflect RF energy from the monopole antenna elements toward the aperture of the waveguide.

5. The apparatus of Claim 4 wherein the RF reflecting screen is positioned between $1/8$ to $1/2$ wavelength from the monopole antenna elements.
6. The apparatus of Claim 4 wherein the waveguide comprises an enclosure surrounding the monopole antenna elements providing a vessel for enclosing a bolus of fluid between the monopole antenna elements and the breast.
7. The apparatus of Claim 6 wherein the vessel comprises a bolus of deionized water.
8. The apparatus of Claim 3 wherein the monopole antenna elements are arranged along a circular arc of substantially constant radius.
9. The apparatus of Claim 8 wherein the radius is substantially the distance from the monopole antenna array to the surface of the breast adjacent an internal target.

-97-

10. The apparatus of Claim 8 wherein the radius is substantially the distance from the monopole antenna array to a target within the breast.
11. The apparatus of Claim 3 wherein the monopole antenna elements resonate at between 800 and 1000 MHz.
12. The apparatus of Claims 2 further comprising
at least one electric field probe for detecting electric field radiation; and
a controller coupled to the electric field probe for receiving the detected electric field radiation and generating a respective feedback signal for controlling the source of electric field energy applied to each phased-array antenna transmit element, and for adjusting the feedback signal in response to the detected electric field radiation so that the detected electric field radiation is maximized at the electric field probe.
13. The apparatus of Claim 12, wherein the electric field probe comprises at least one probe element disposed invasively within the breast at the desired focus of the electric field energy.
14. The apparatus of Claim 13, further comprising mammography means for imaging the internal structure of the breast.
15. A hyperthermia applicator for inducing a temperature rise in a human breast, comprising

-98-

a first waveguide comprising a first aperture and a first electric field radiator coupled to a source of electric field energy for producing electric field radiation output from the first waveguide through the first aperture;

a second waveguide comprising a second aperture and a second electric field radiator coupled to a source of electric field energy for producing electric field radiation output from the second waveguide through the second aperture;

compression means for compressing a human breast to a predetermined thickness, the first and second waveguides being adapted to be disposed on opposite sides of the compression means such that the compressed breast is positioned to receive electric field radiation from the first and second waveguides.

16. The apparatus of Claim 15, wherein the first and second electric field radiators each comprise a phased-array of electric field transmit elements.
17. The apparatus of Claim 16, wherein the phased-array of electric field transmit elements comprises an array of monopole antenna elements.
18. The apparatus of Claim 17, wherein the first and second waveguides each comprise
 - a first RF reflecting groundplane surface for mounting the monopole antenna elements, wherein the monopole antenna elements are perpendicularly mounted to the same side of the RF reflecting ground plane,

-99-

a second RF reflecting groundplane surface disposed substantially parallel to the first RF reflecting groundplane such that the monopole antenna elements are positioned between the first and second RF reflecting groundplanes, and

an RF reflecting screen mounted substantially perpendicular to the first and second RF groundplane surfaces behind the monopole antenna elements to reflect RF energy from the monopole antenna elements toward the aperture of the corresponding waveguide.

19. The apparatus of Claim 18 wherein the RF reflecting screen is positioned between $1/8$ to $1/2$ wavelength from the monopole antenna elements.
20. The apparatus of Claim 18 wherein said first and second waveguides each comprise an enclosure surrounding the monopole antenna elements providing a vessel for enclosing a bolus of fluid between the monopole antenna elements and the breast.
21. The apparatus of Claim 20 wherein the vessel comprises a bolus of deionized water.
22. The apparatus of Claim 17 wherein the monopole antenna elements are arranged along a circular arc of substantially constant radius.
23. The apparatus of Claim 22 wherein the radius is substantially the distance from the monopole antenna

-100-

array to the surface of the breast adjacent a target within the breast.

24. The apparatus of Claim 22 wherein the radius is substantially the distance from the monopole antenna array to the target within the breast.
25. The apparatus of Claim 17 wherein the monopole antenna elements resonate at between 800 and 1000 MHz.
26. The apparatus of Claims 16 further comprising
at least one electric field probe for detecting electric field radiation; and
a controller coupled to the electric field probe for receiving the detected electric field radiation and generating a respective feedback signal for controlling the source of electric field energy applied to each phased-array antenna transmit element, and for adjusting the feedback signal in response to the detected electric field radiation so that the detected electric field radiation is maximized at the electric field probe.
27. The apparatus of Claim 26, wherein the electric field probe comprises at least one probe element disposed invasively within the breast at the desired focus of the electric field energy.
28. The apparatus of Claim 27, further comprising mammography means for imaging the internal structure of the breast.

-101-

29. A method for inducing a temperature rise in a human breast, comprising the steps of:

compressing a human breast to a predetermined thickness;

positioning adjacent the breast a waveguide comprising an aperture and an electric field radiator coupled to a source of electric field energy for producing electric field radiation output from the waveguide through the aperture;

irradiating the breast with electric field radiation output from the waveguide aperture to raise the internal temperature of the breast tissue.

30. The method of Claim 29, further comprising the steps of:

inserting an electric field probe, for detecting electric field radiation, into the breast at the desired focus of the electric field energy;

detecting the electric field radiation with the electric field probe; and

generating a feedback signal for controlling the source of electric field energy applied to the electric field radiator in response to the detected electric field radiation so that the detected electric field radiation is maximized at the electric field probe.

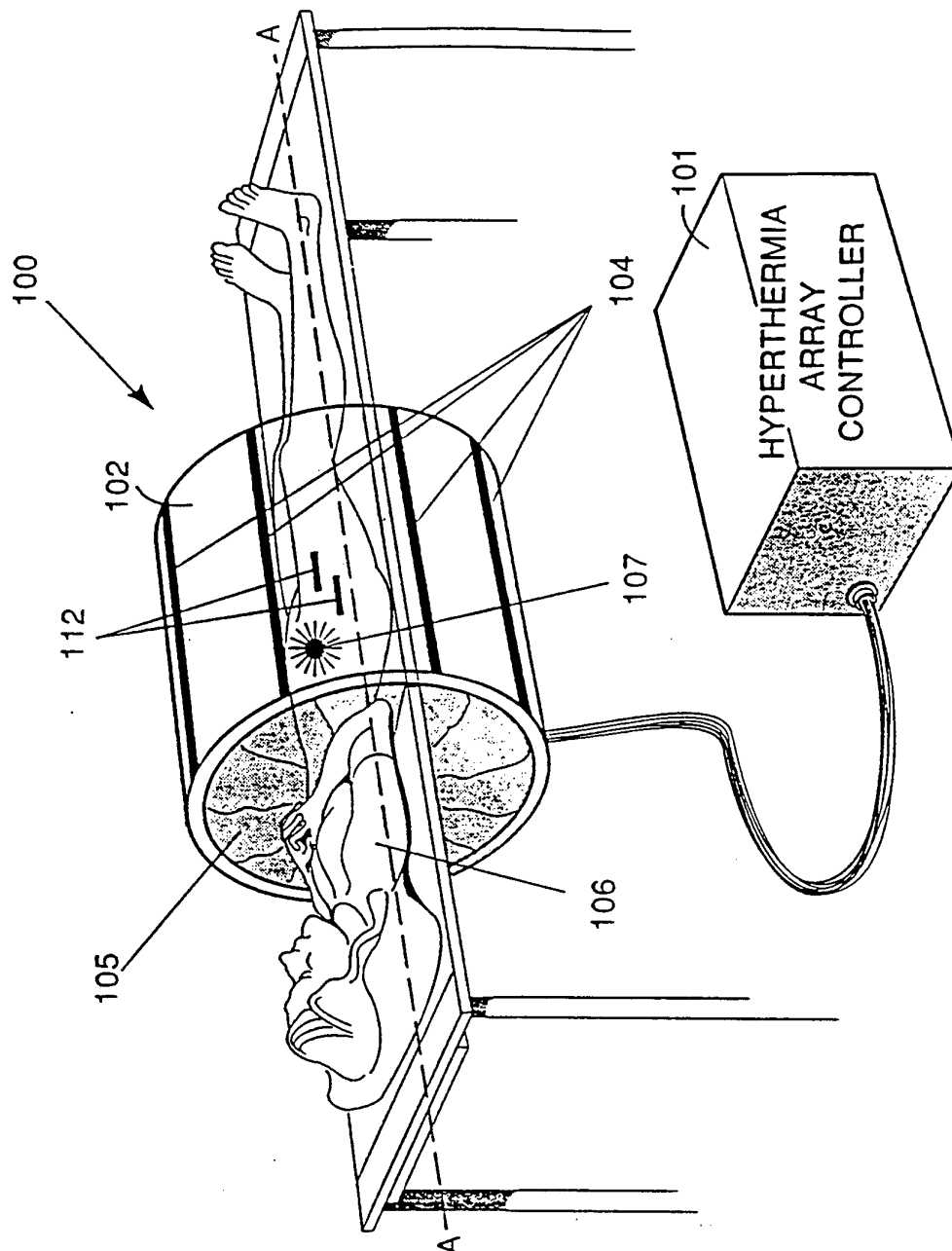


Fig. 1

2/69

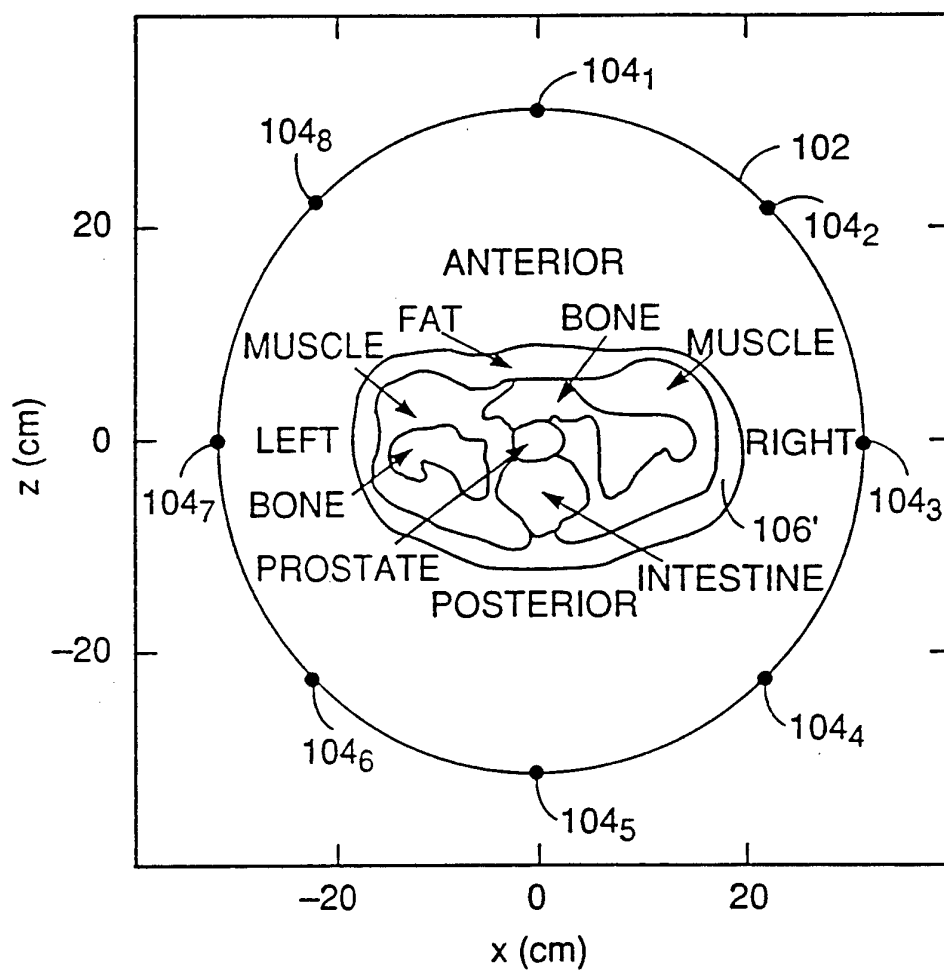


Fig. 2

3/69

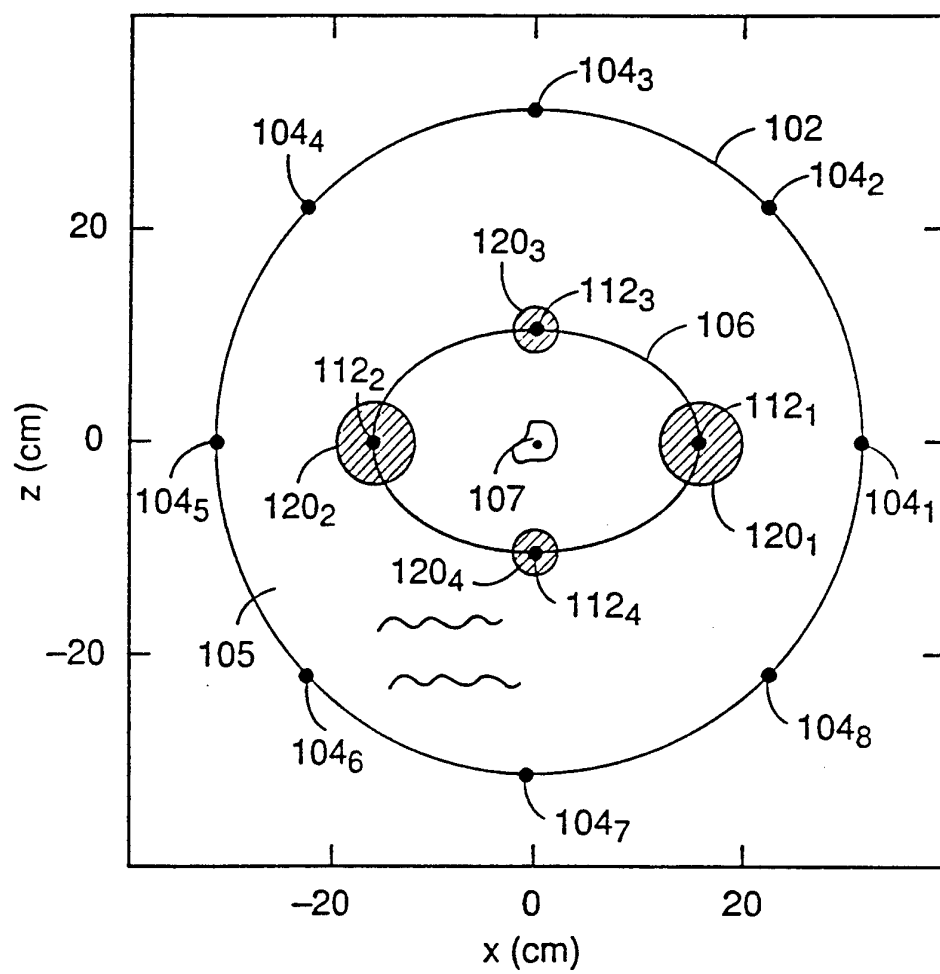


Fig. 3

4/69

8-ELEMENT RING ARRAY
60-cm ARRAY DIAMETER
120-MHz OPERATION
FOCUSED AT (0,0)
 $t = 20$ min

$T(x,z)$
BEFORE NULLING,
 $\Delta l = 0.9525$ cm
 $T_{MAX} = 46^{\circ}\text{C}$
 25°C (Initial)

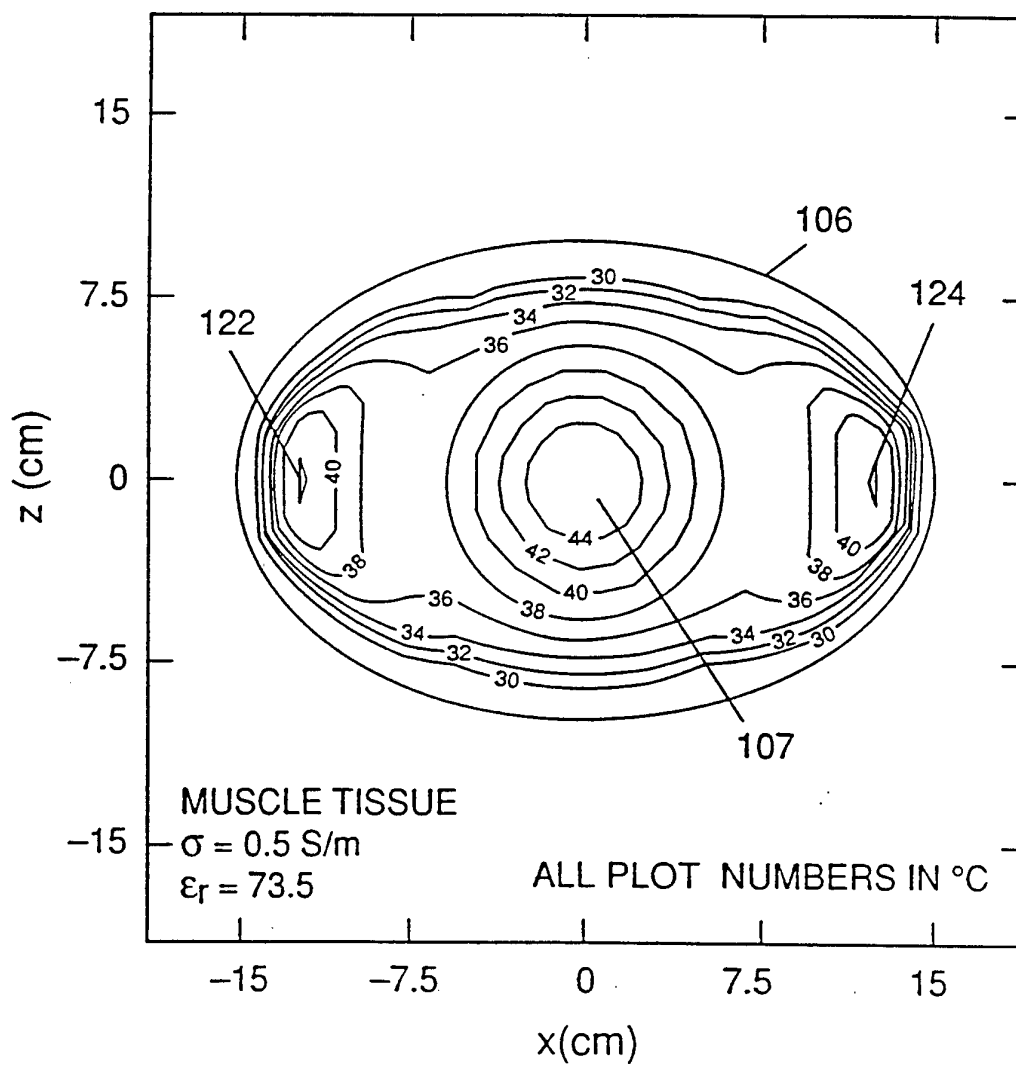


Fig. 4

5/69

8-ELEMENT DIPOLE RING ARRAY
 60-cm ARRAY DIAMETER
 120-MHz OPERATION
 FOCUSED AT (0,0)
 $t = 20$ min
 4 AUXILIARIES

$T(x,z)$
 AFTER NULLING,
 $\Delta l = 0.9525$ cm
 $T_{MAX} = 46^{\circ}\text{C}$
 25°C (Initial)

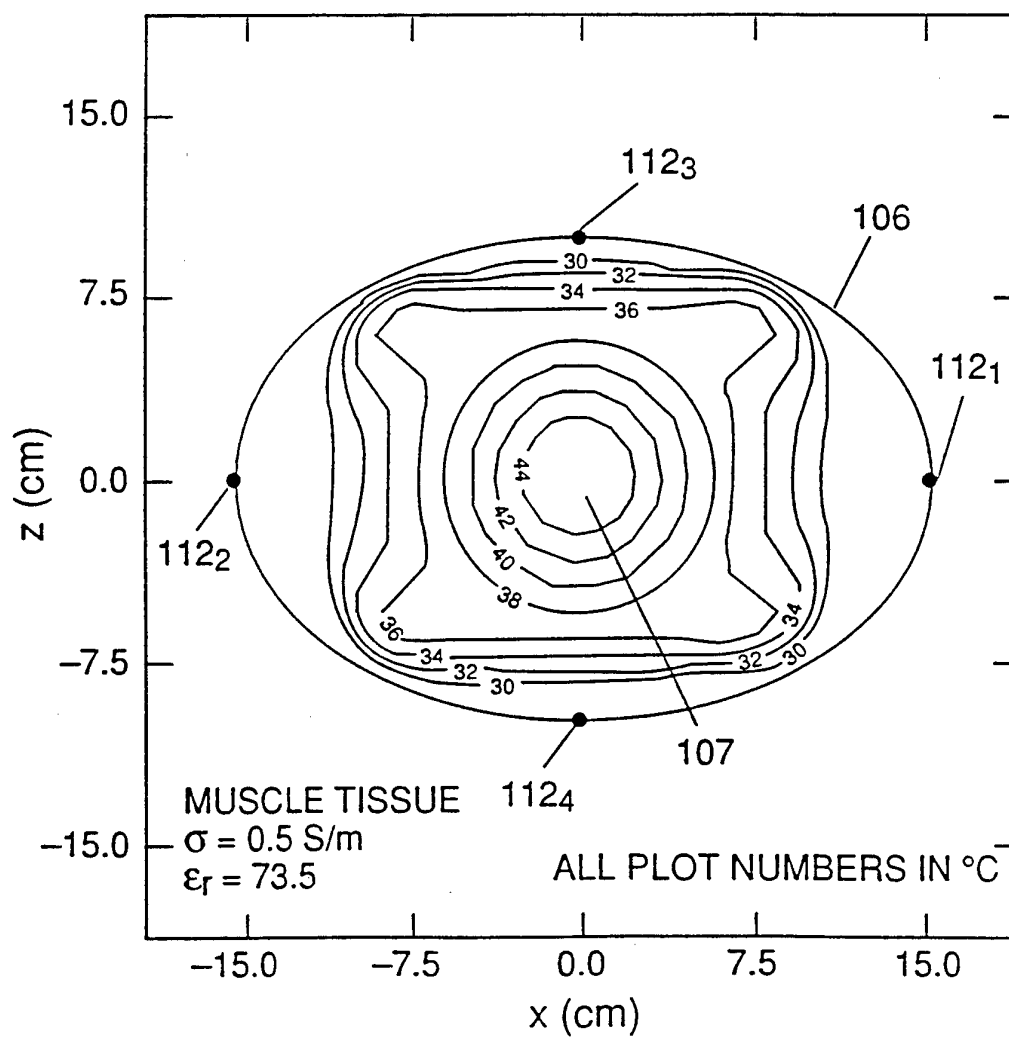


Fig. 5

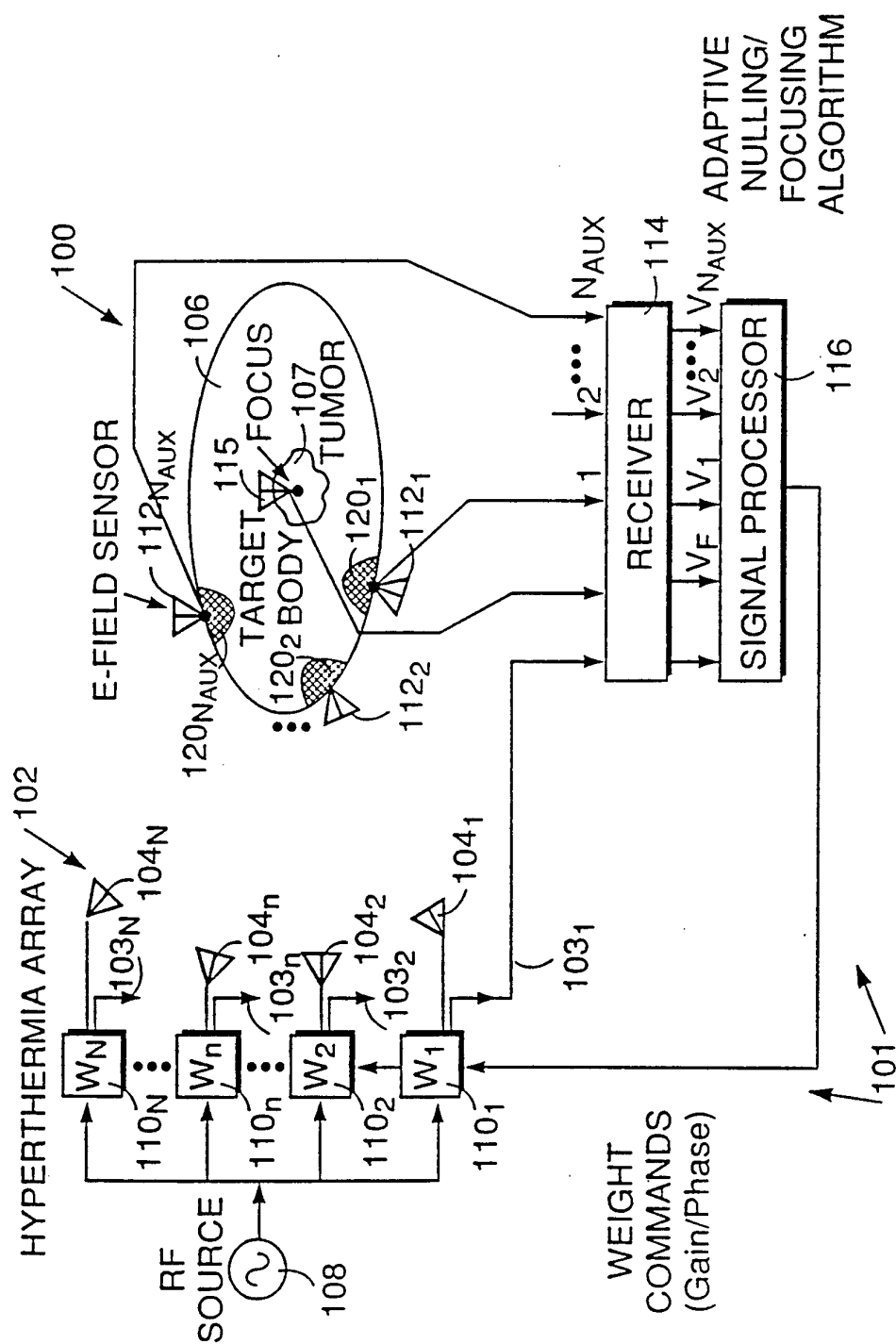


Fig. 6

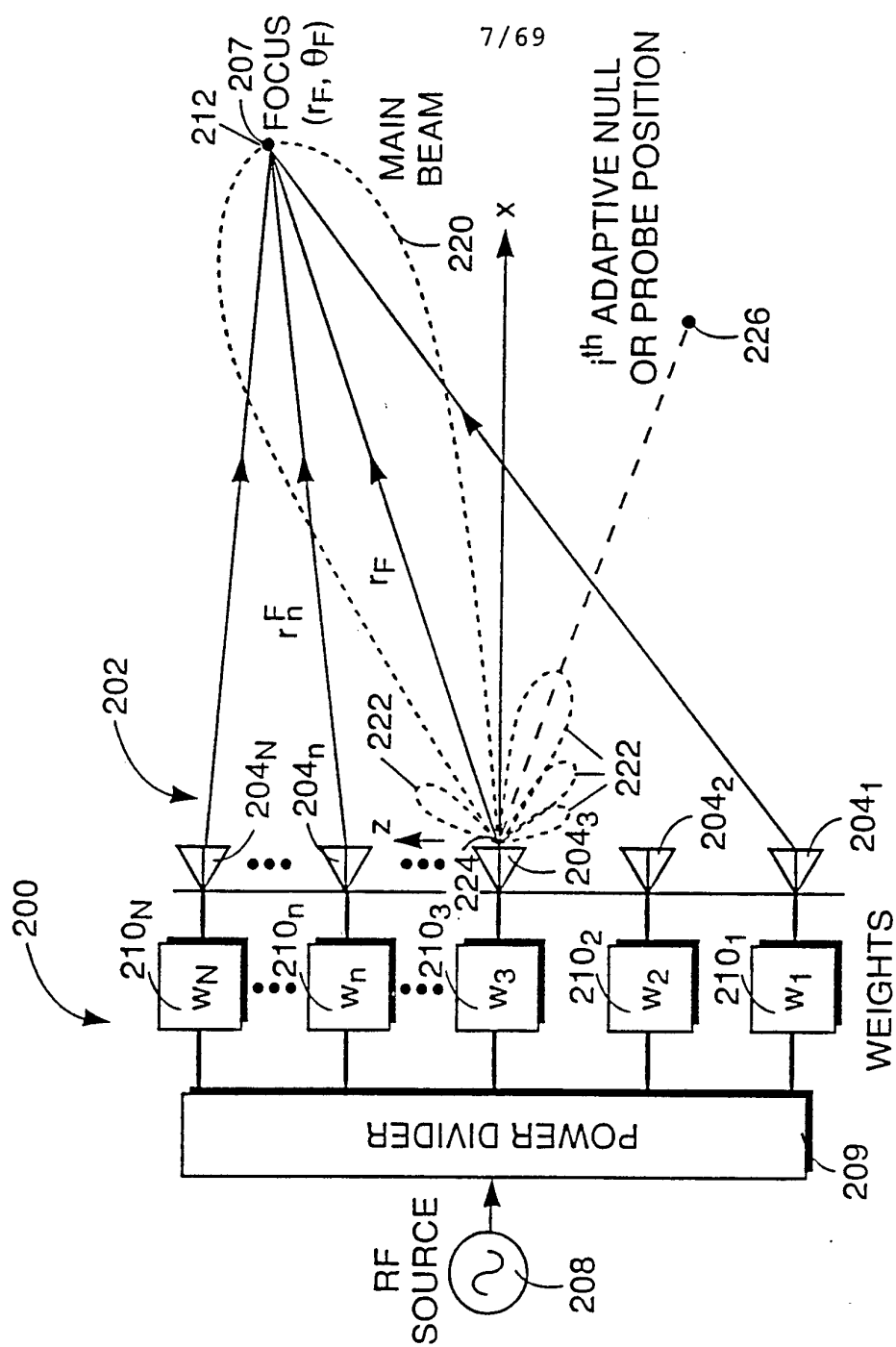


Fig. 7

8/69

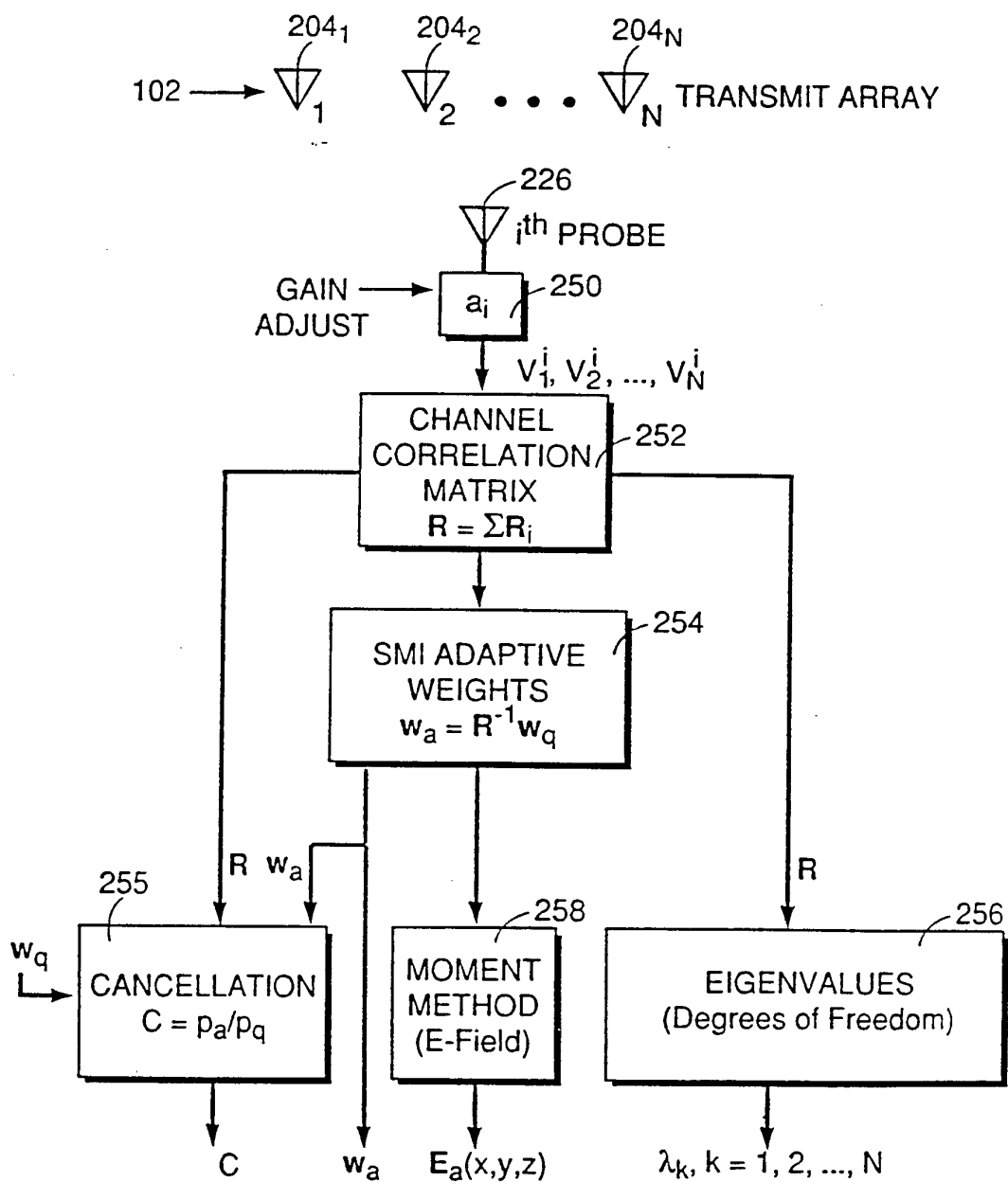


Fig. 8

9/69

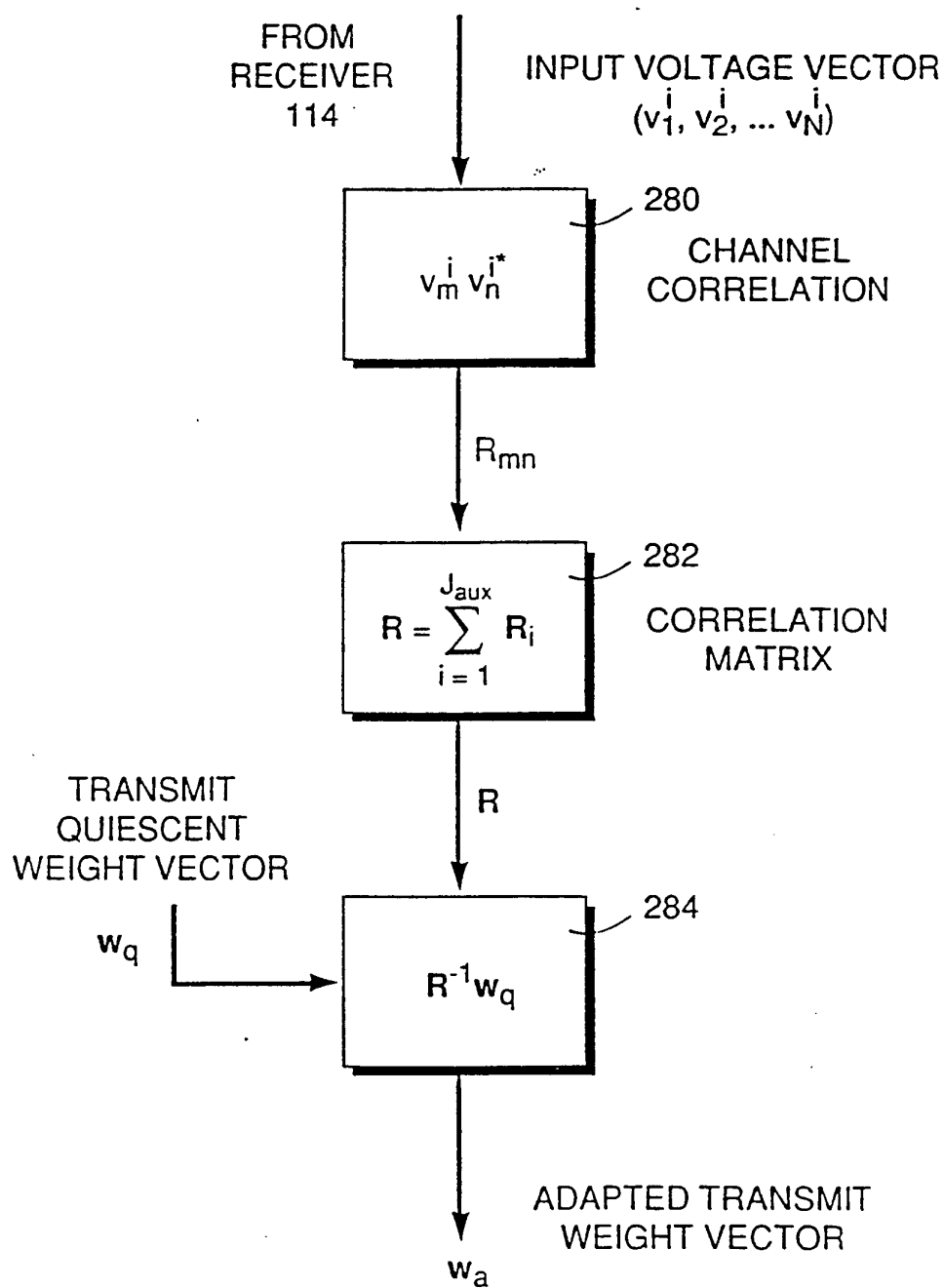


Fig. 9

10/69

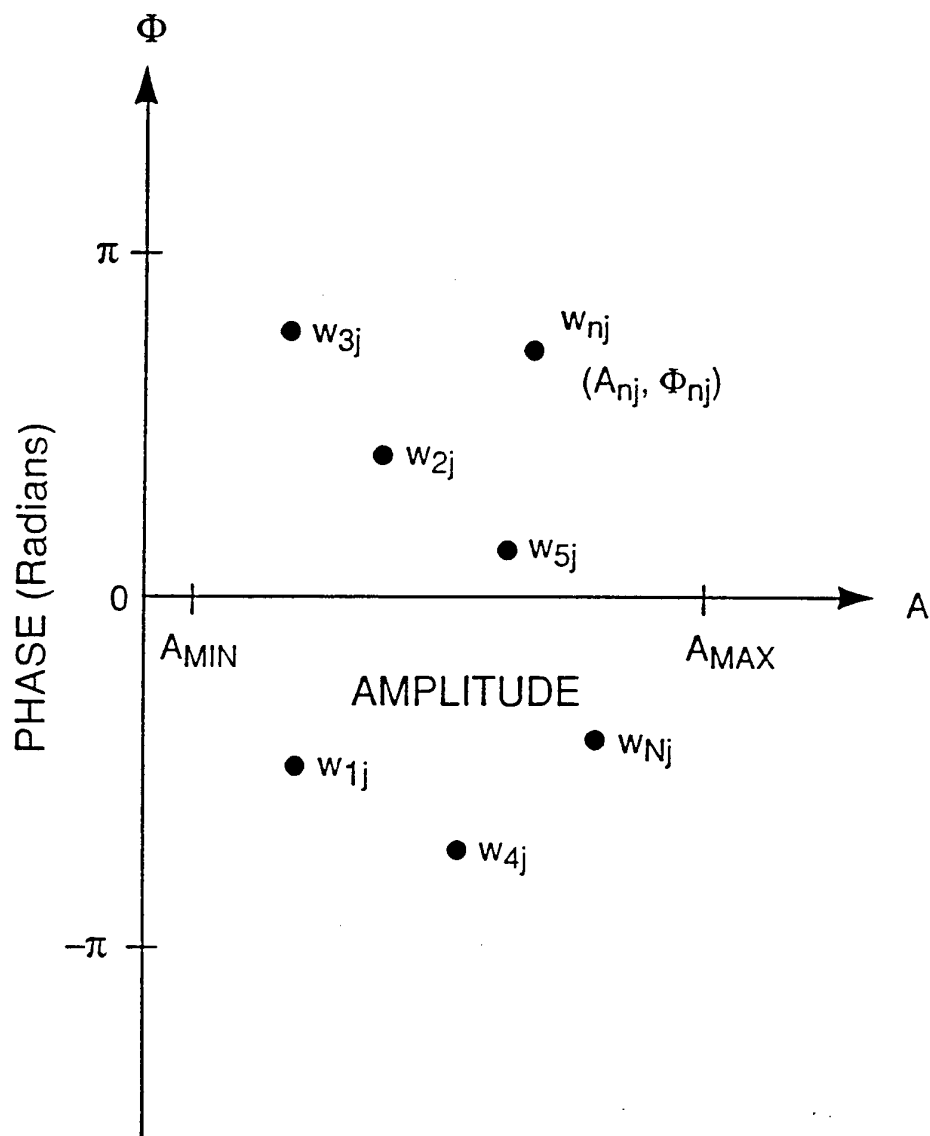


Fig. 10

11/69

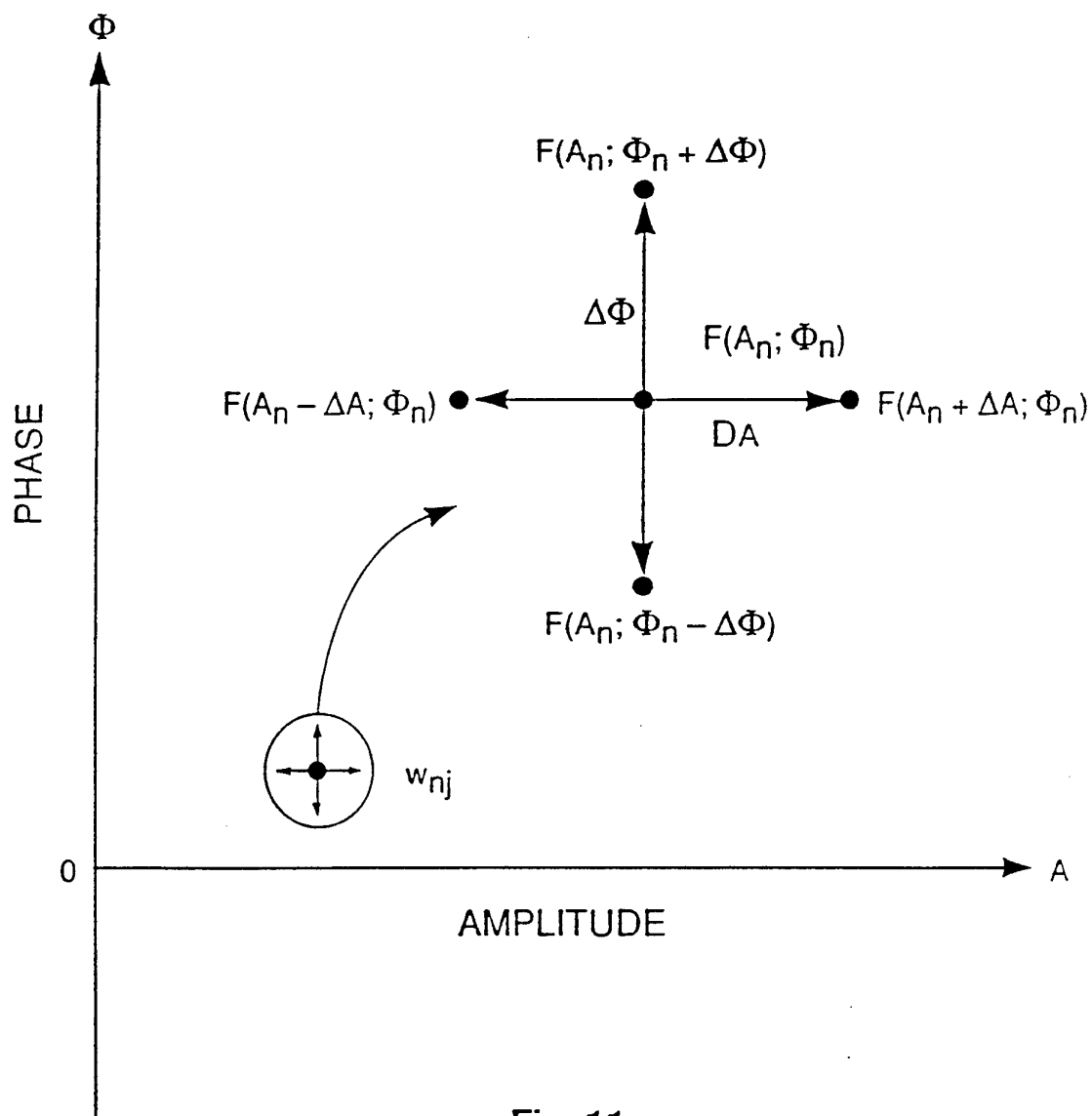


Fig. 11

12/69

GRADIENT SEARCH SYSTEM BLOCK DIAGRAM

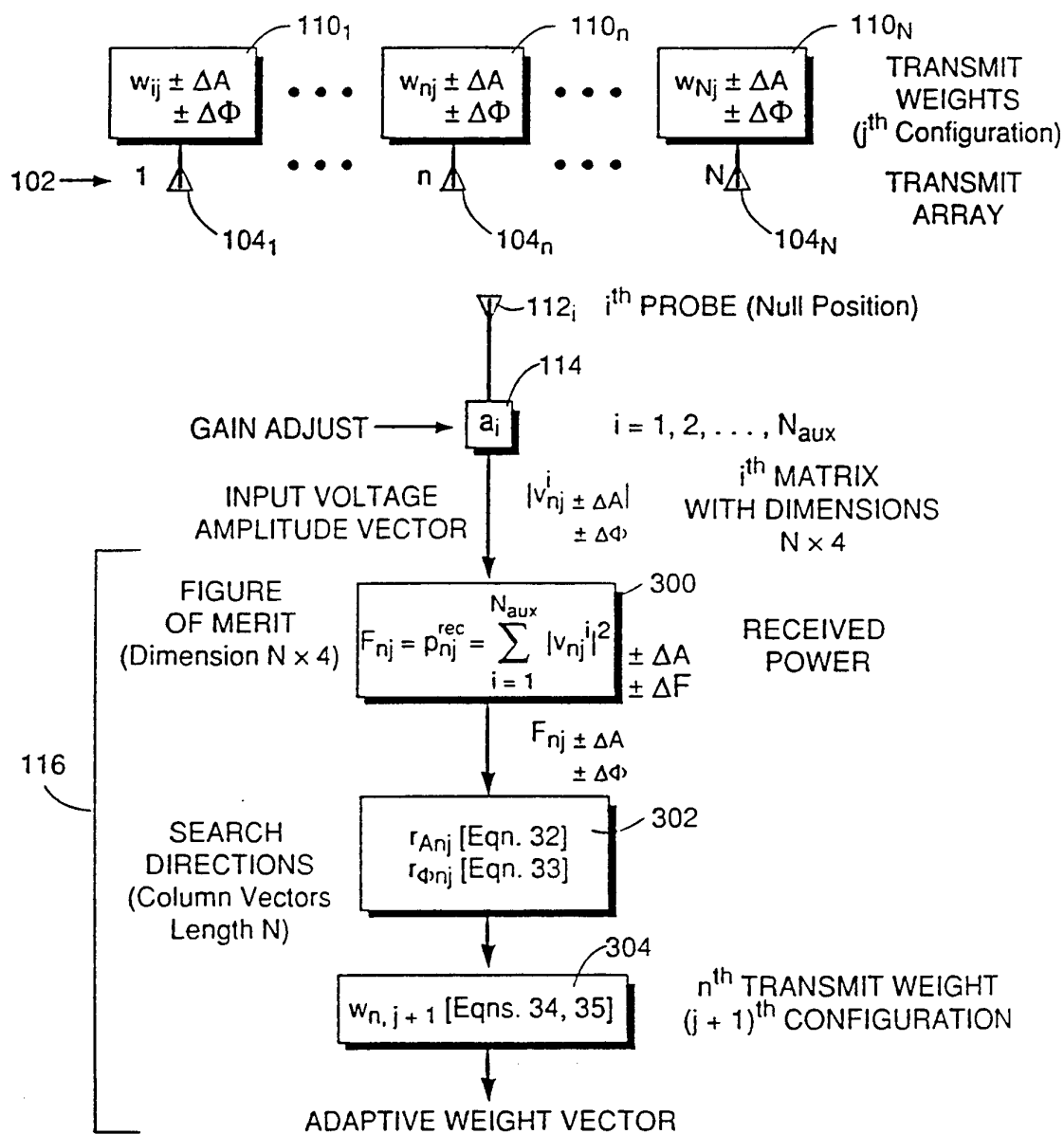


Fig. 12

13/69

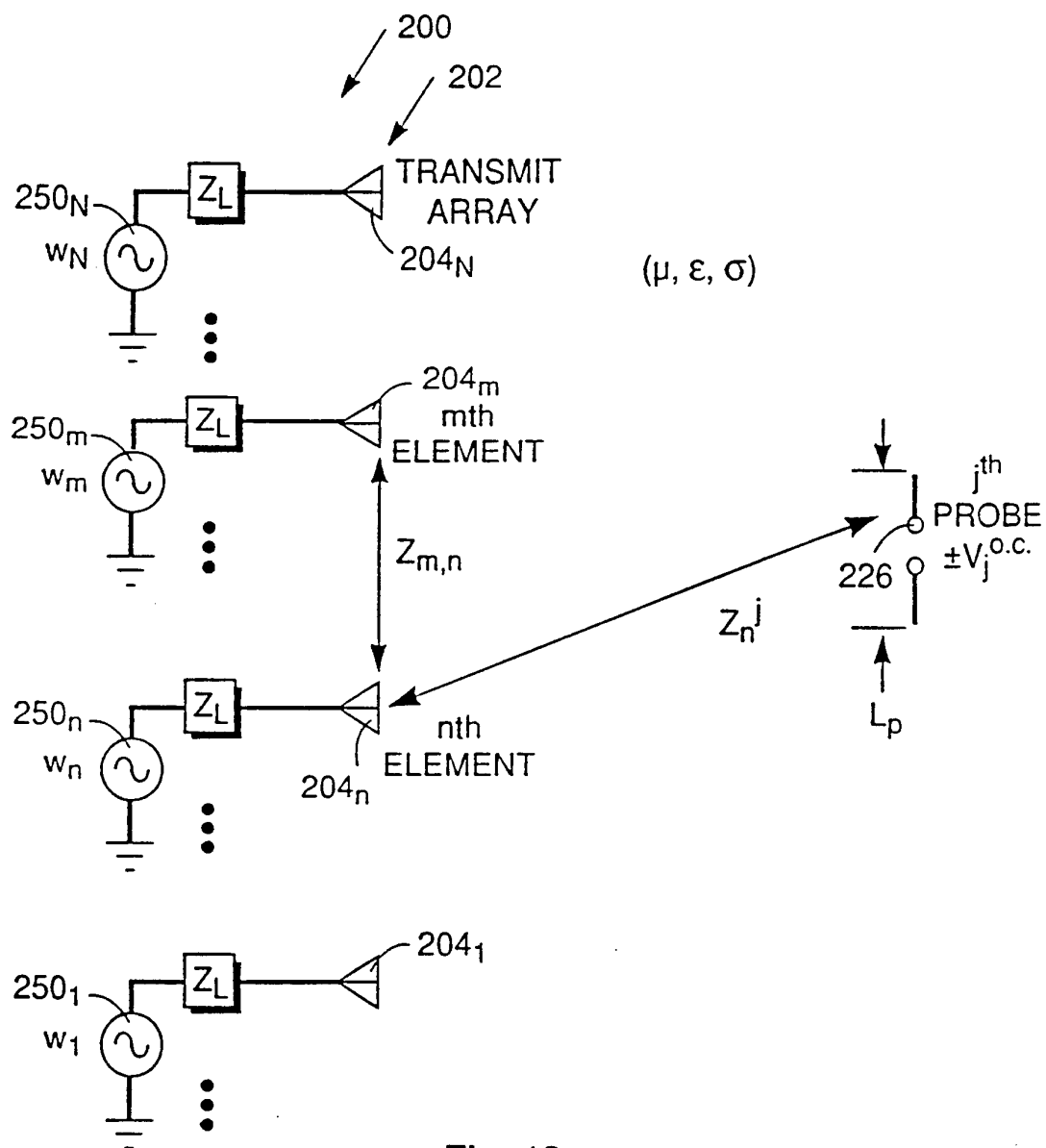


Fig. 13

14/69

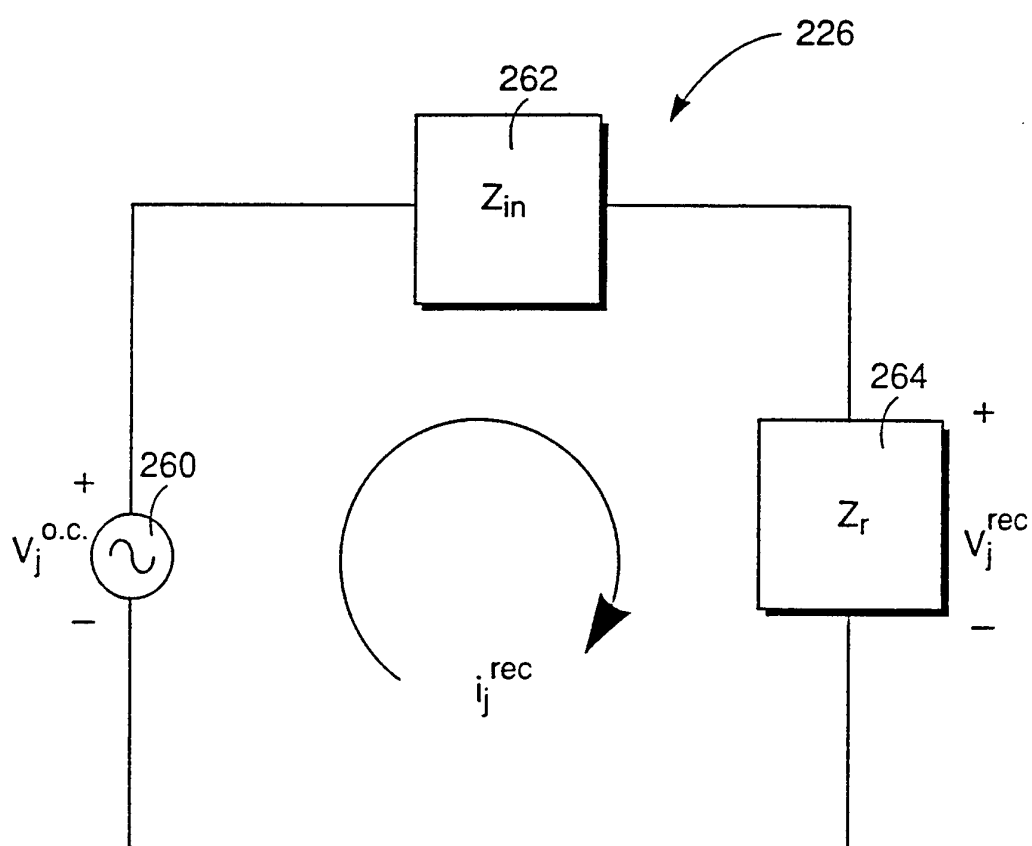
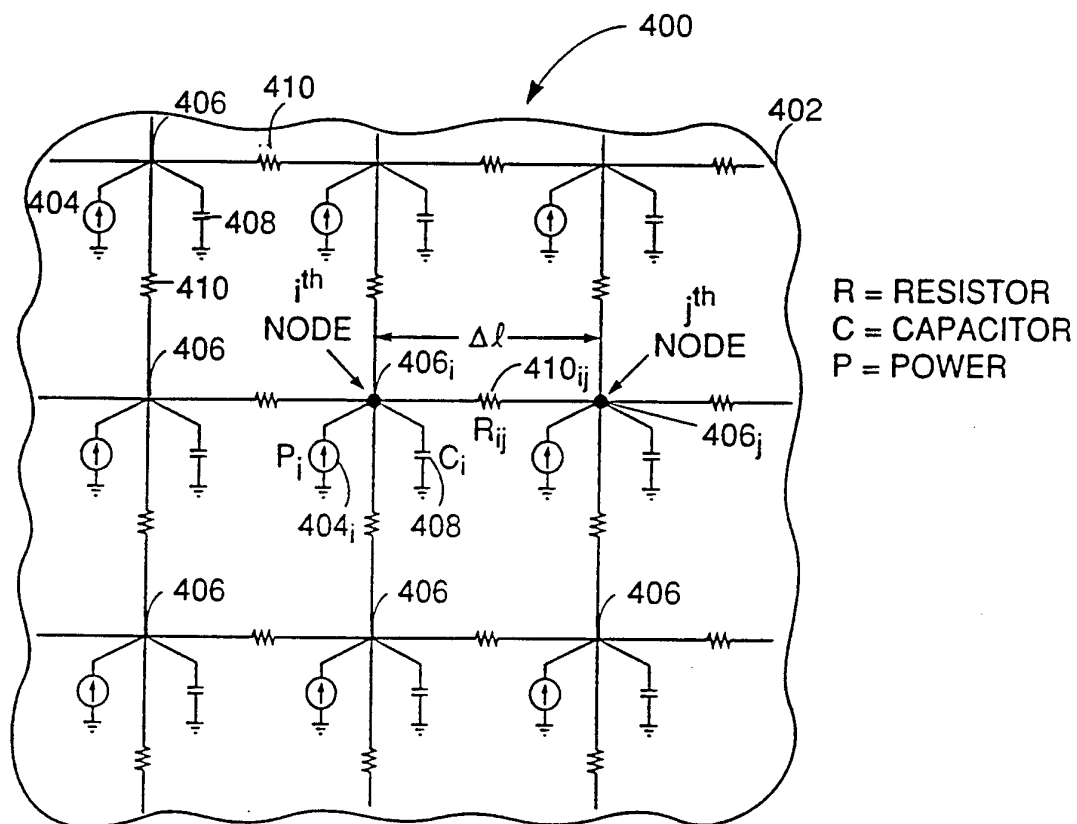


Fig. 14

15/69



$$R = \frac{1}{k\Delta l} [^{\circ}\text{C} / \text{W}], k = \text{THERMAL CONDUCTIVITY}$$

$$C = \rho C_p (\Delta l)^3 [\text{J}/^{\circ}\text{C}], \rho = \text{DENSITY}, C_p = \text{SPECIFIC HEAT}$$

$$P = \text{SAR } \rho (\Delta l)^3 [\text{W}], \text{SAR} = \frac{\sigma}{2\rho} |E|^2 (\text{Specific Absorption Rate})$$

σ = ELECTRICAL CONDUCTIVITY

$|E|$ = MAGNITUDE OF ELECTRIC FIELD

Fig. 15

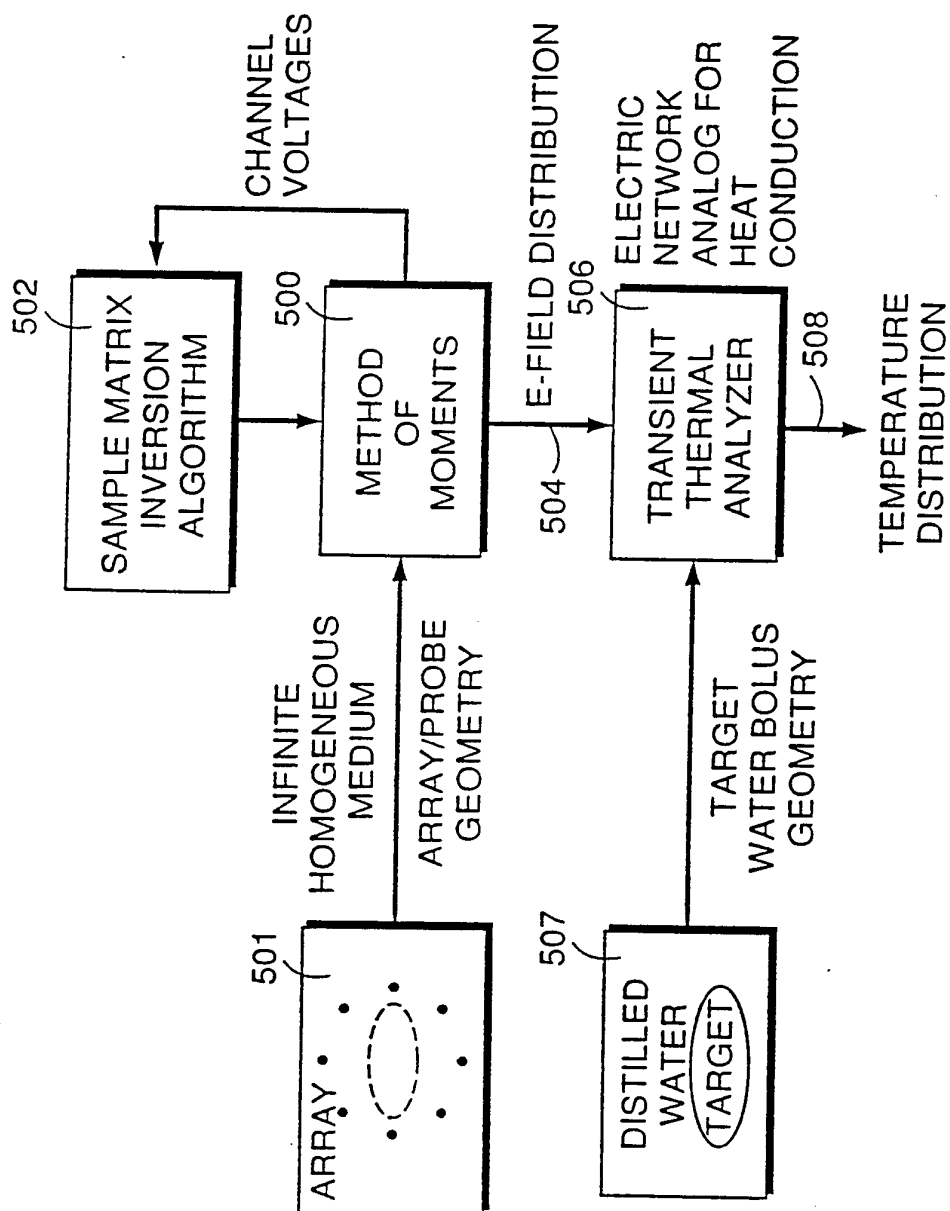


Fig. 16(a)

PARAMETER	PHANTOM MUSCLE TISSUE	DISTILLED WATER
DIELECTRIC CONSTANT @ 100 MHz	73.5	80.0
ELECTRICAL CONDUCTIVITY @ 100 MHz	0.5 S/m	0.0001 S/m
DENSITY	970.0 kg/m ³	1000.0 kg/m ³
SPECIFIC HEAT	3516.0 J/kg °C	4200.0 J/kg °C
THERMAL CONDUCTIVITY	0.544 W/m °C	0.6019 W/m °C

Table 1

Fig. 16(b)

18/69

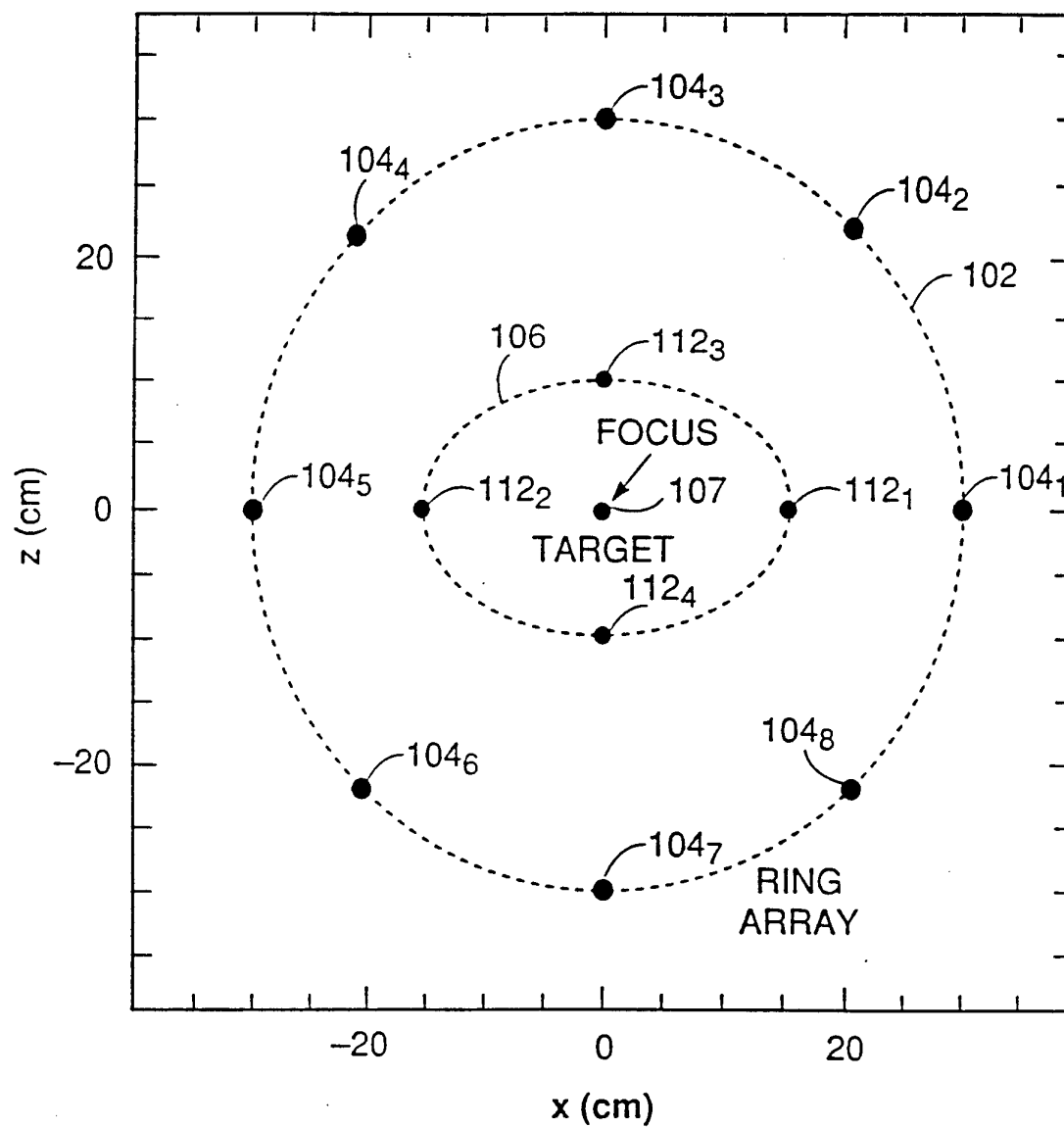


Fig. 17

19/69

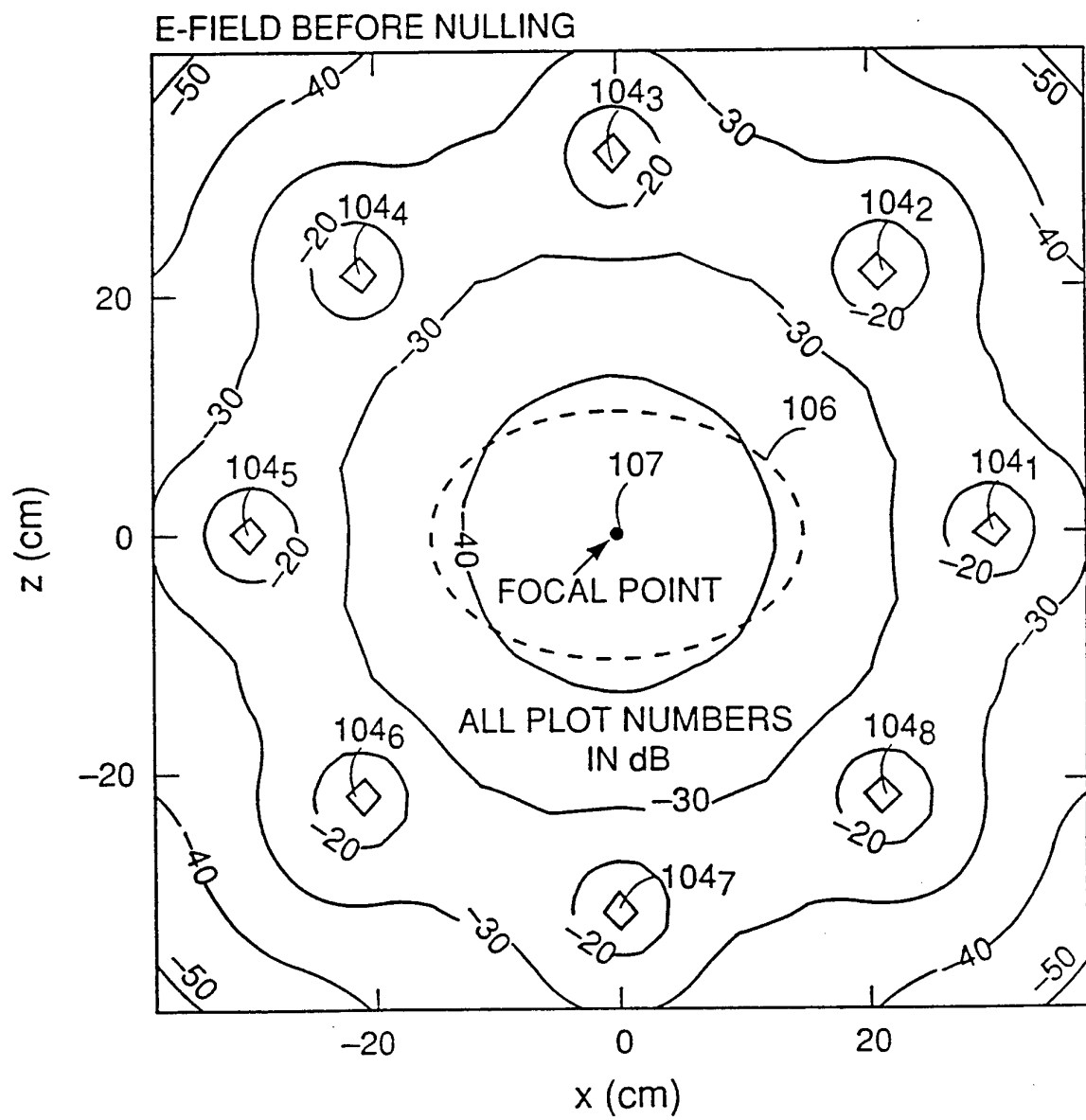


Fig. 18

20/69

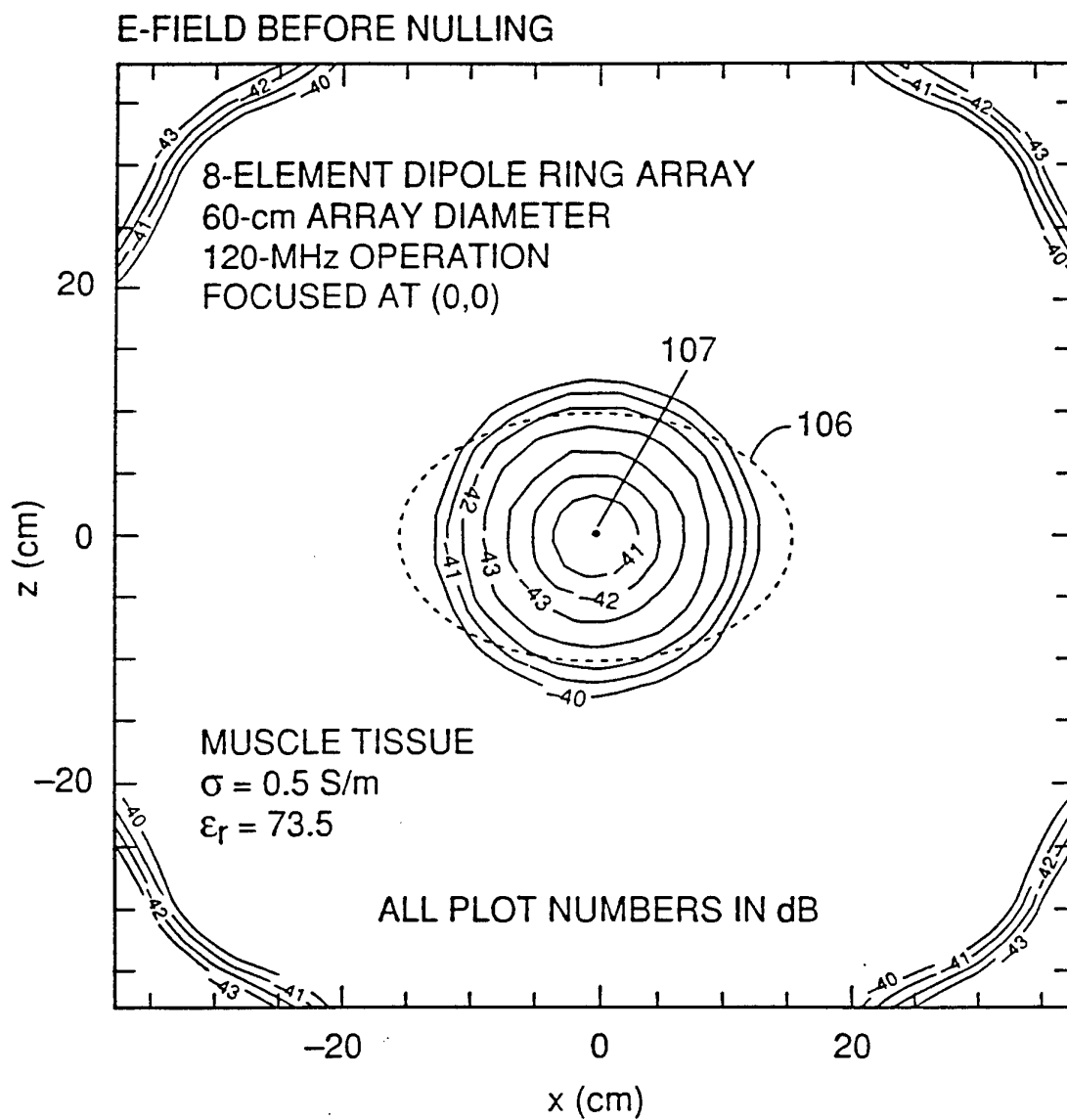


Fig. 19

21/69

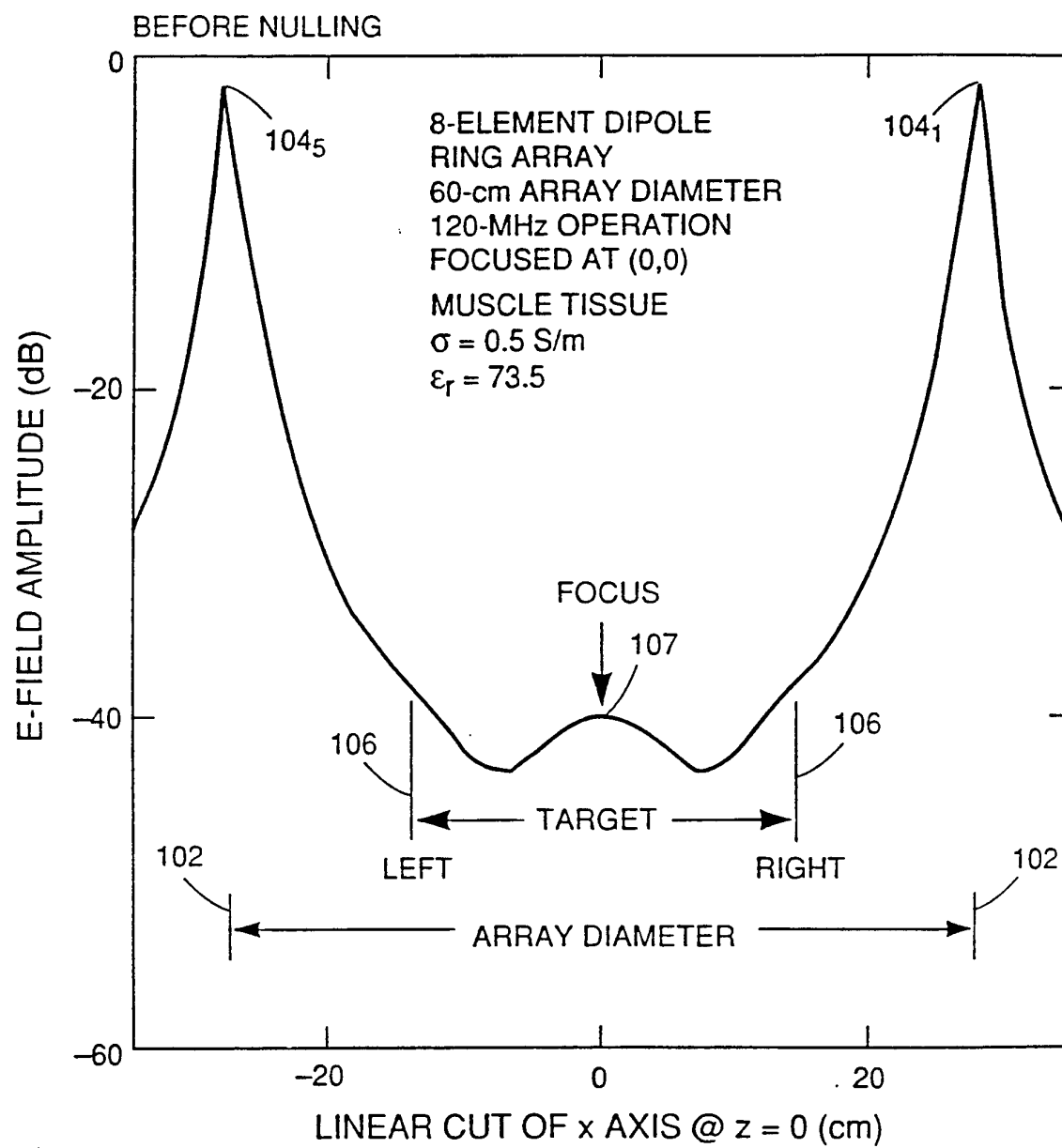


Fig. 20

22/69

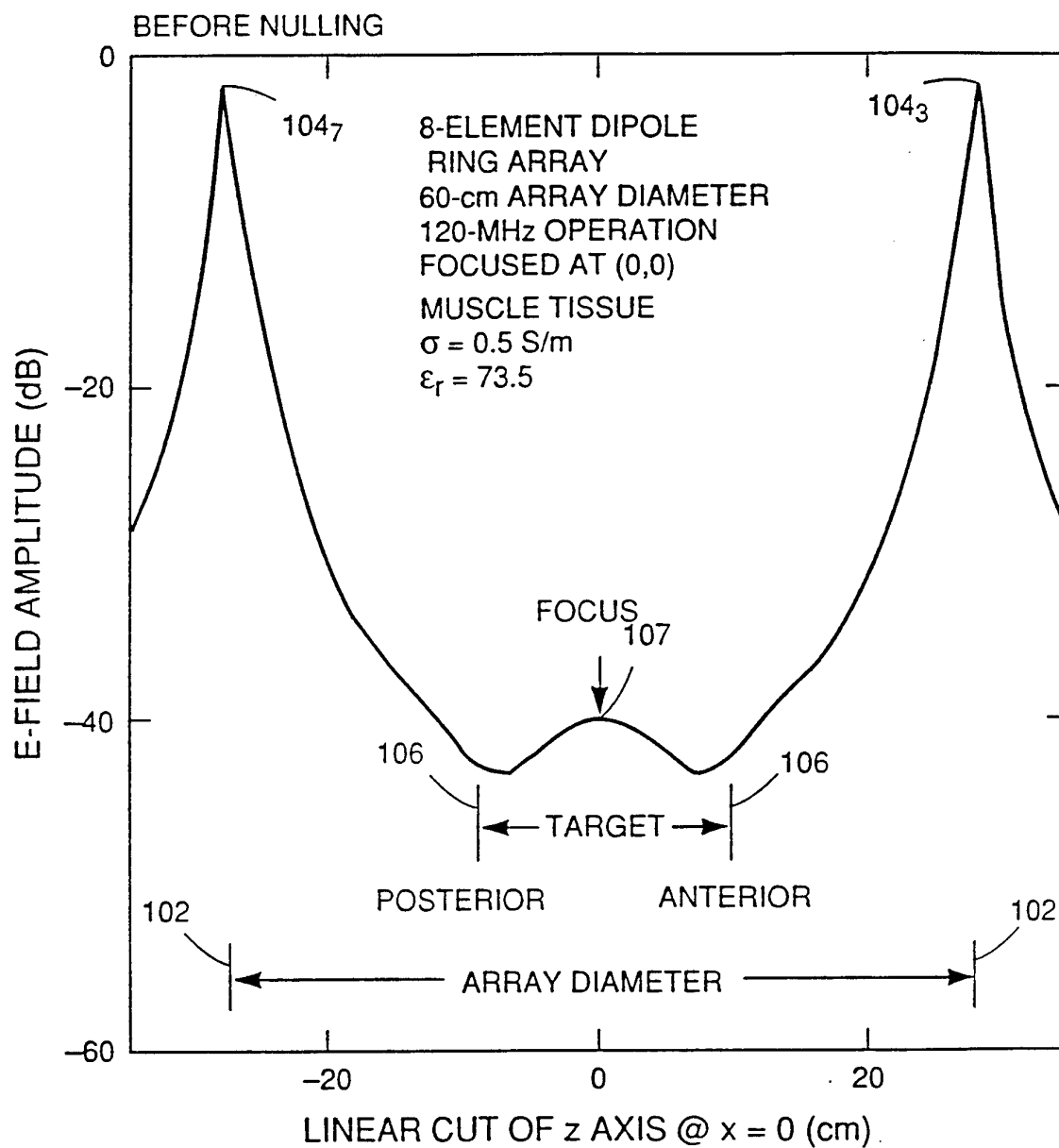


Fig. 21

23/69

E-FIELD AFTER NULLING; 4 AUXILIARIES

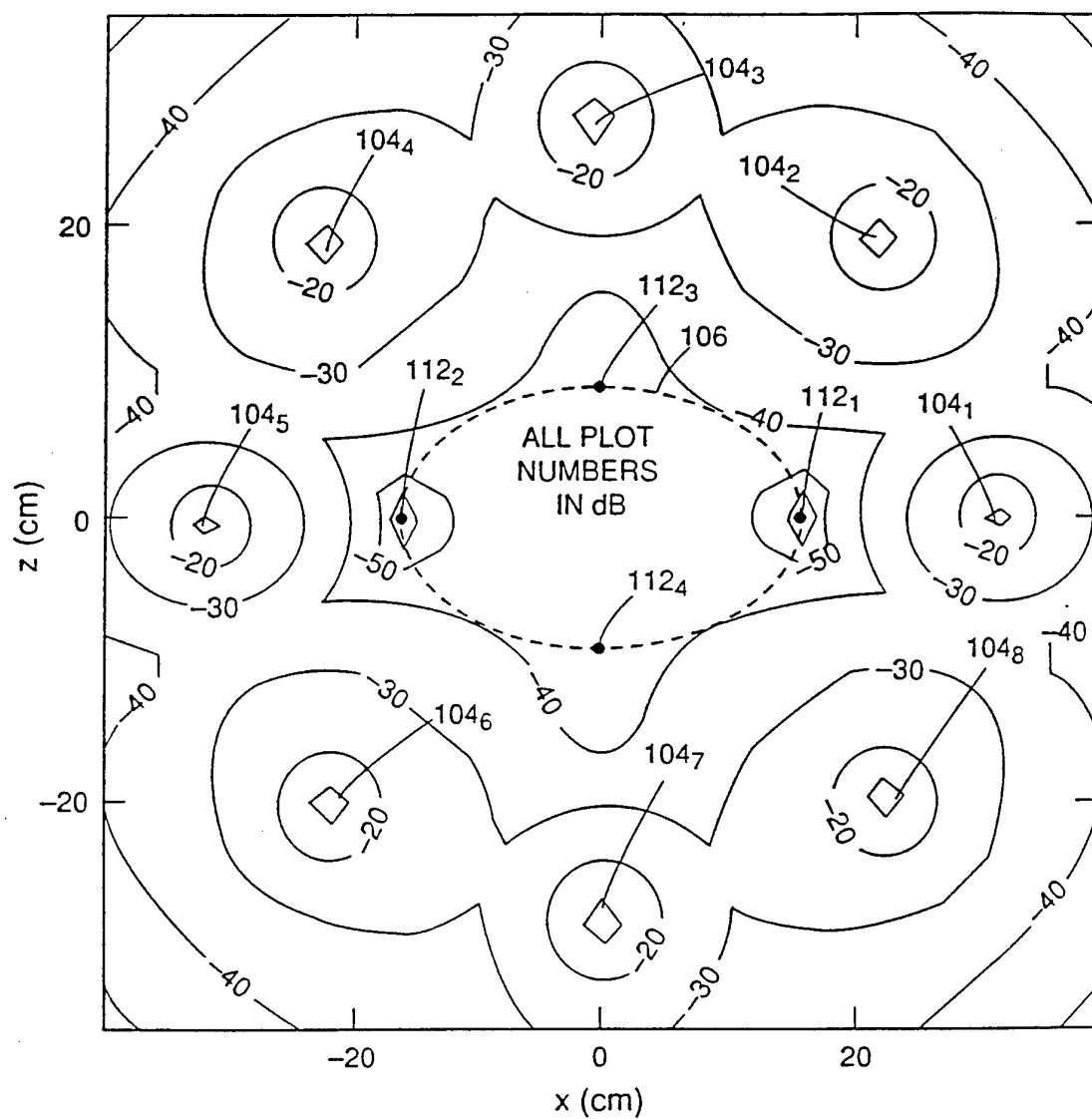


Fig. 22

24/69

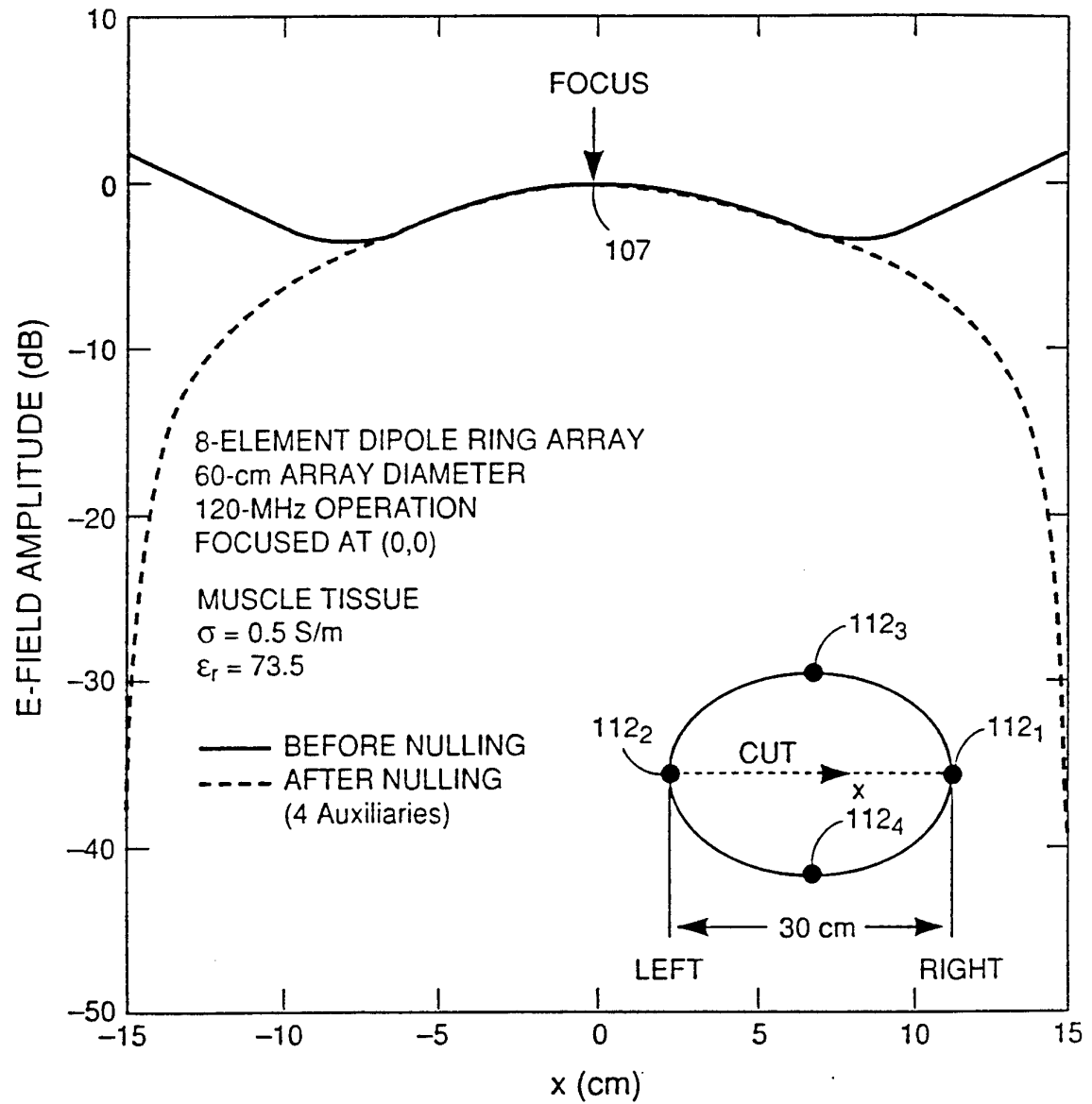


Fig. 23

25/69

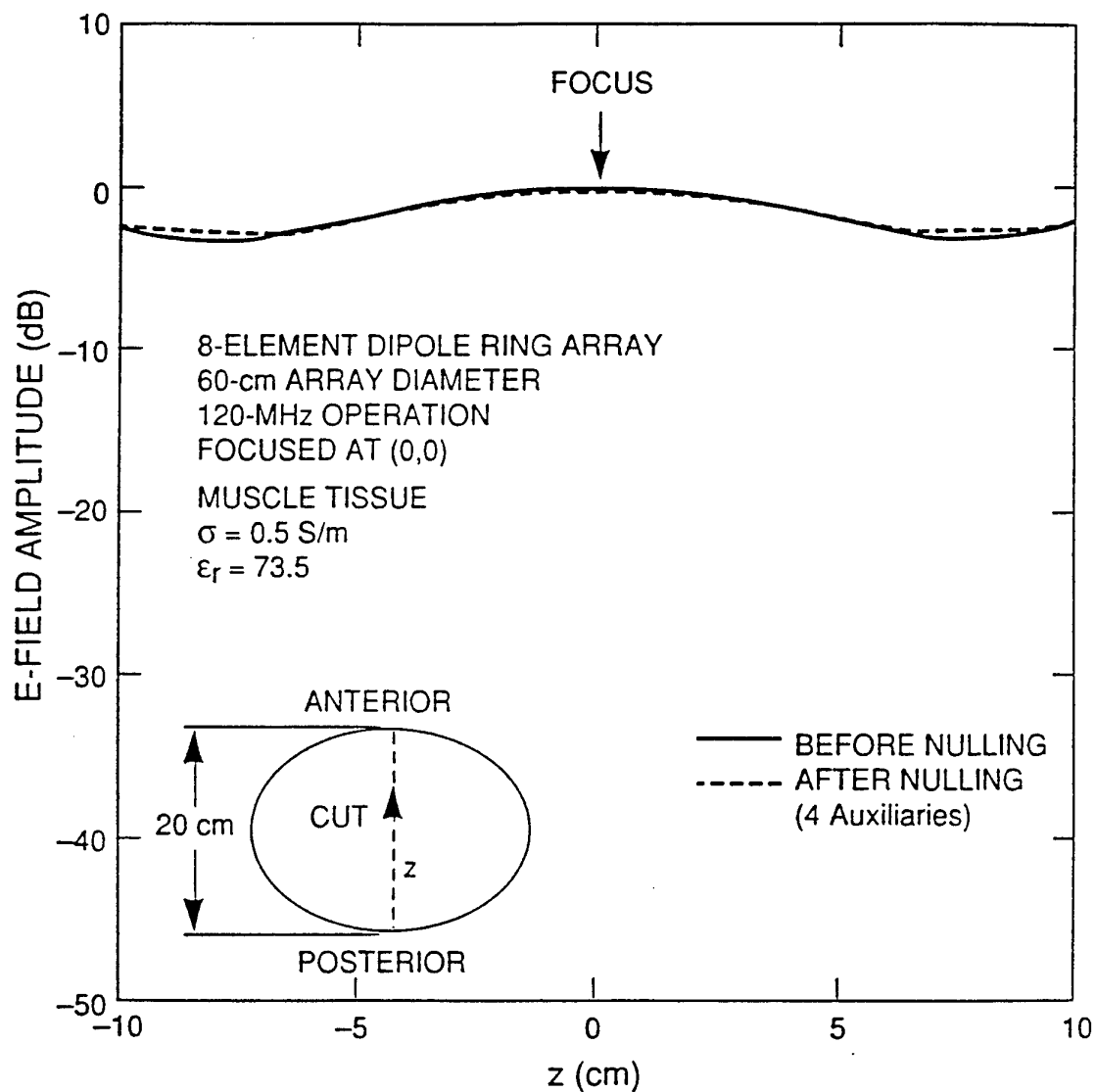


Fig. 24

26/69

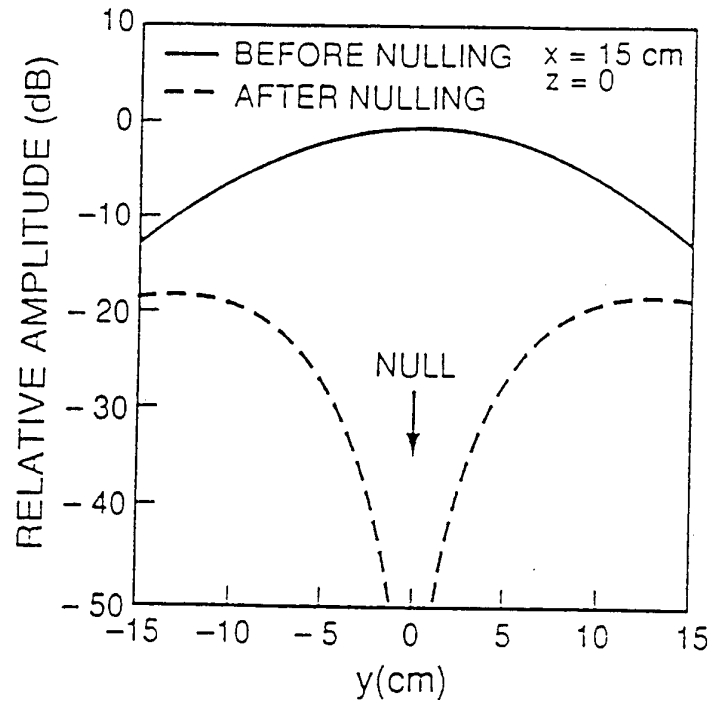


Fig. 25(a)

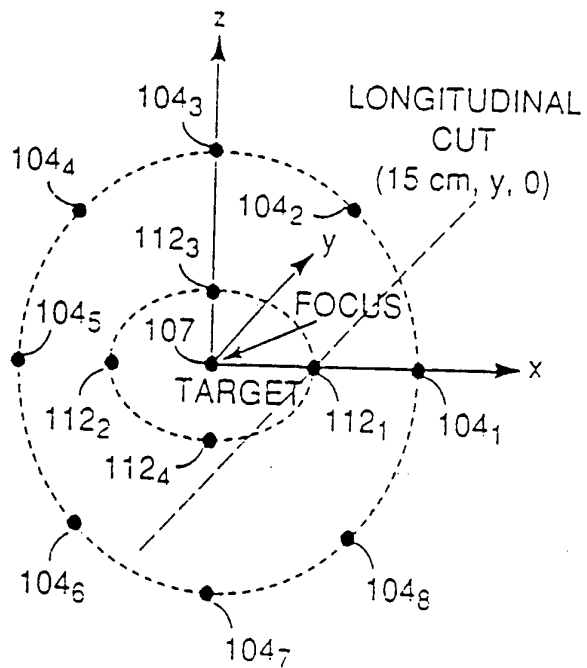


Fig. 25(b)

27/69

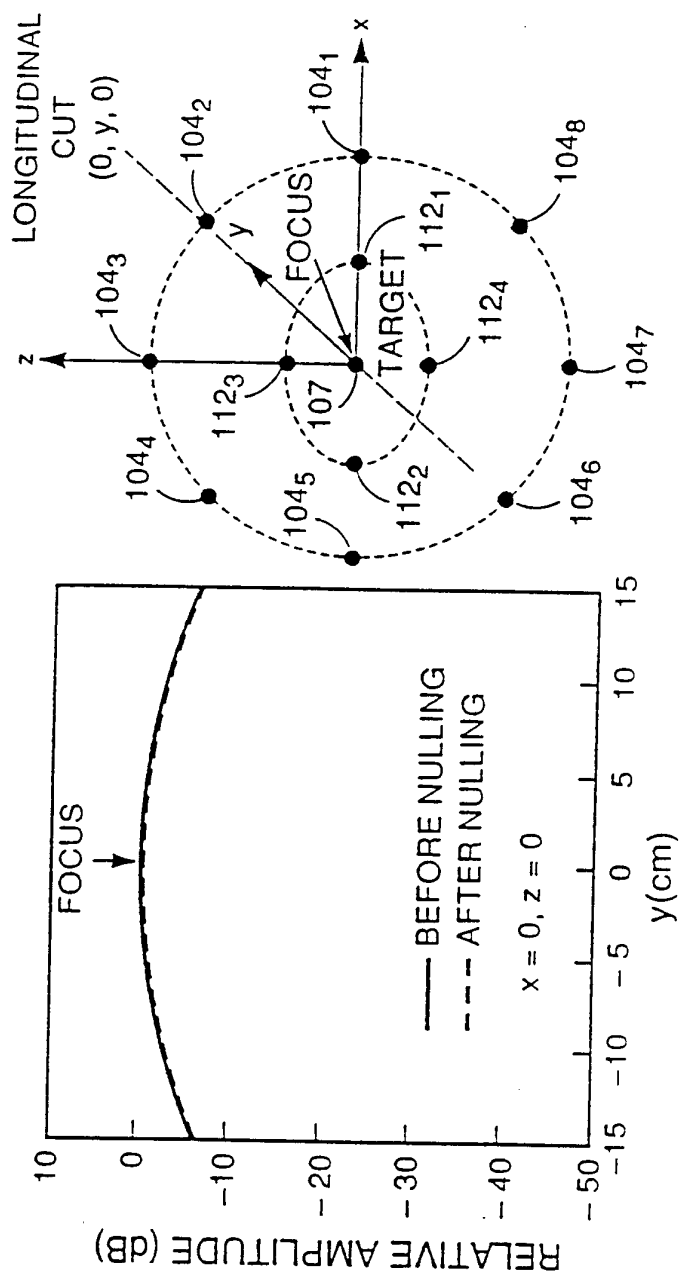


Fig. 26(b)

Fig. 26(a)

28/69

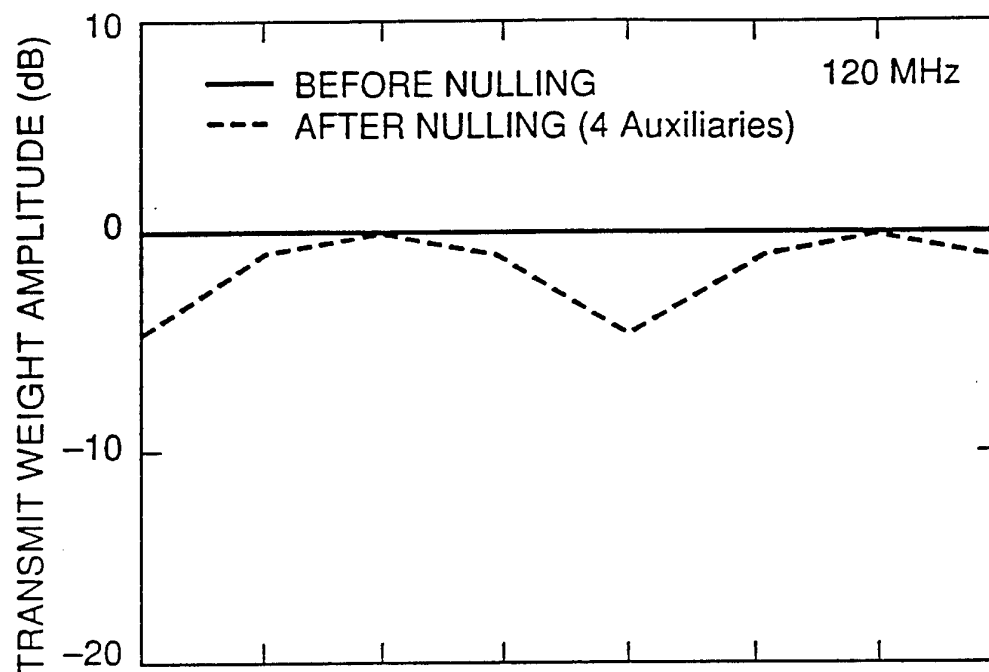


Fig. 27 (a)

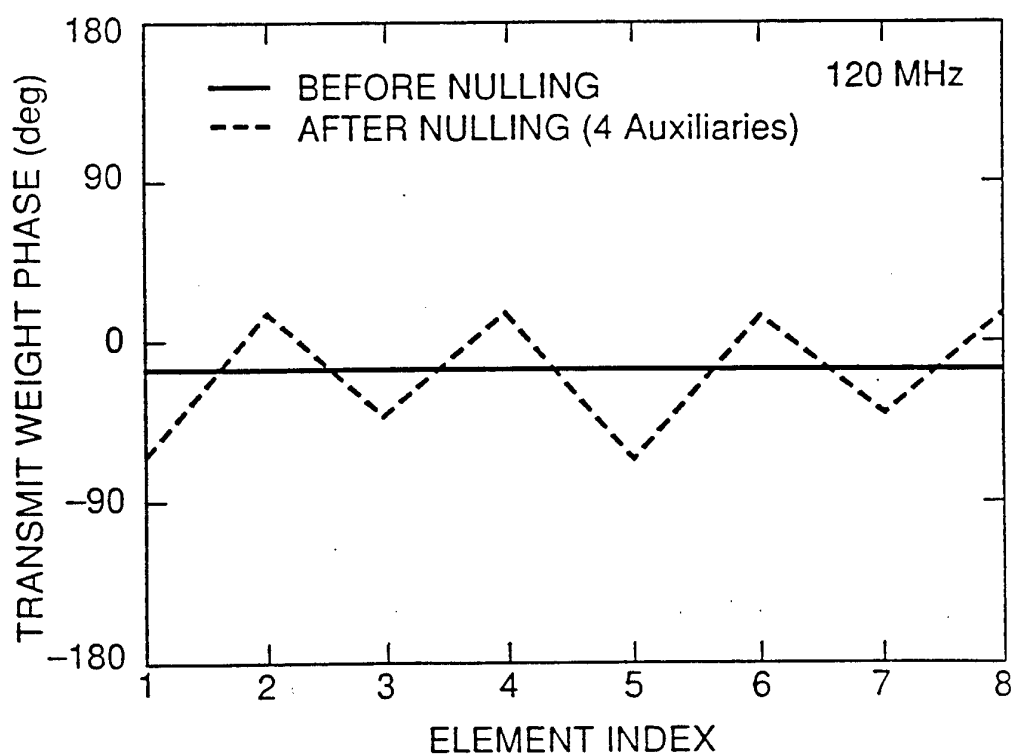


Fig. 27 (b)

29/69

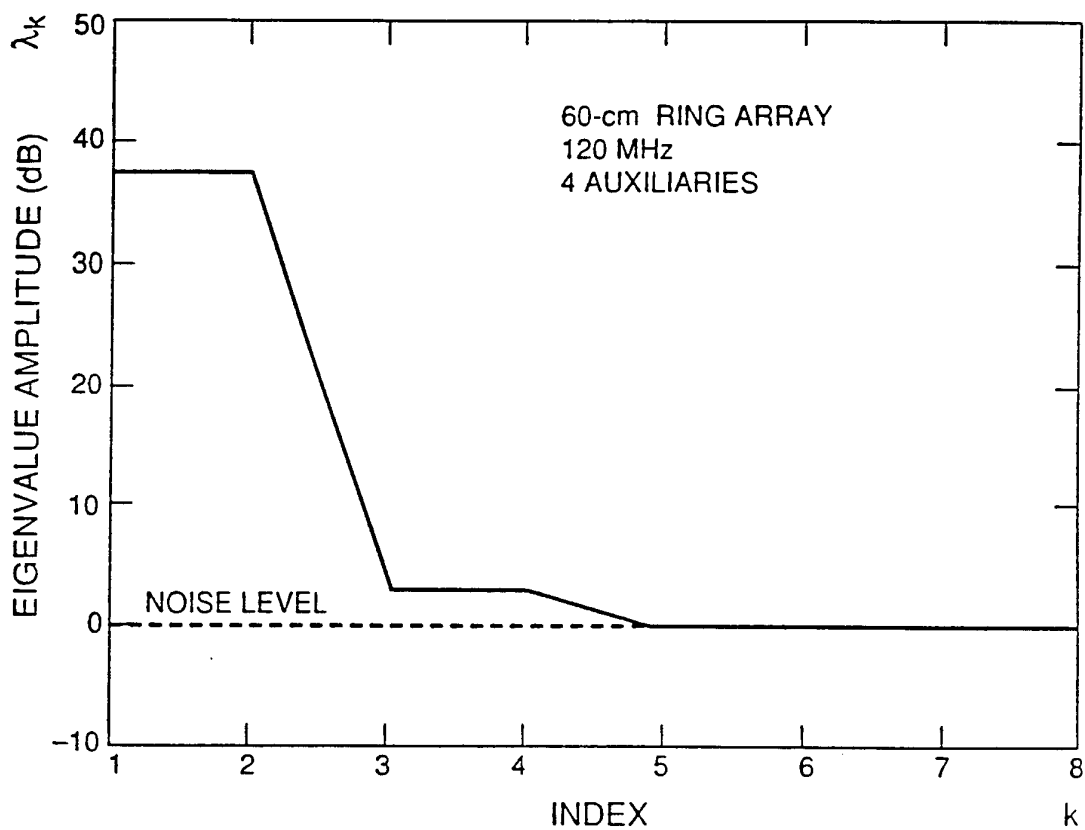


Fig. 28

30/69

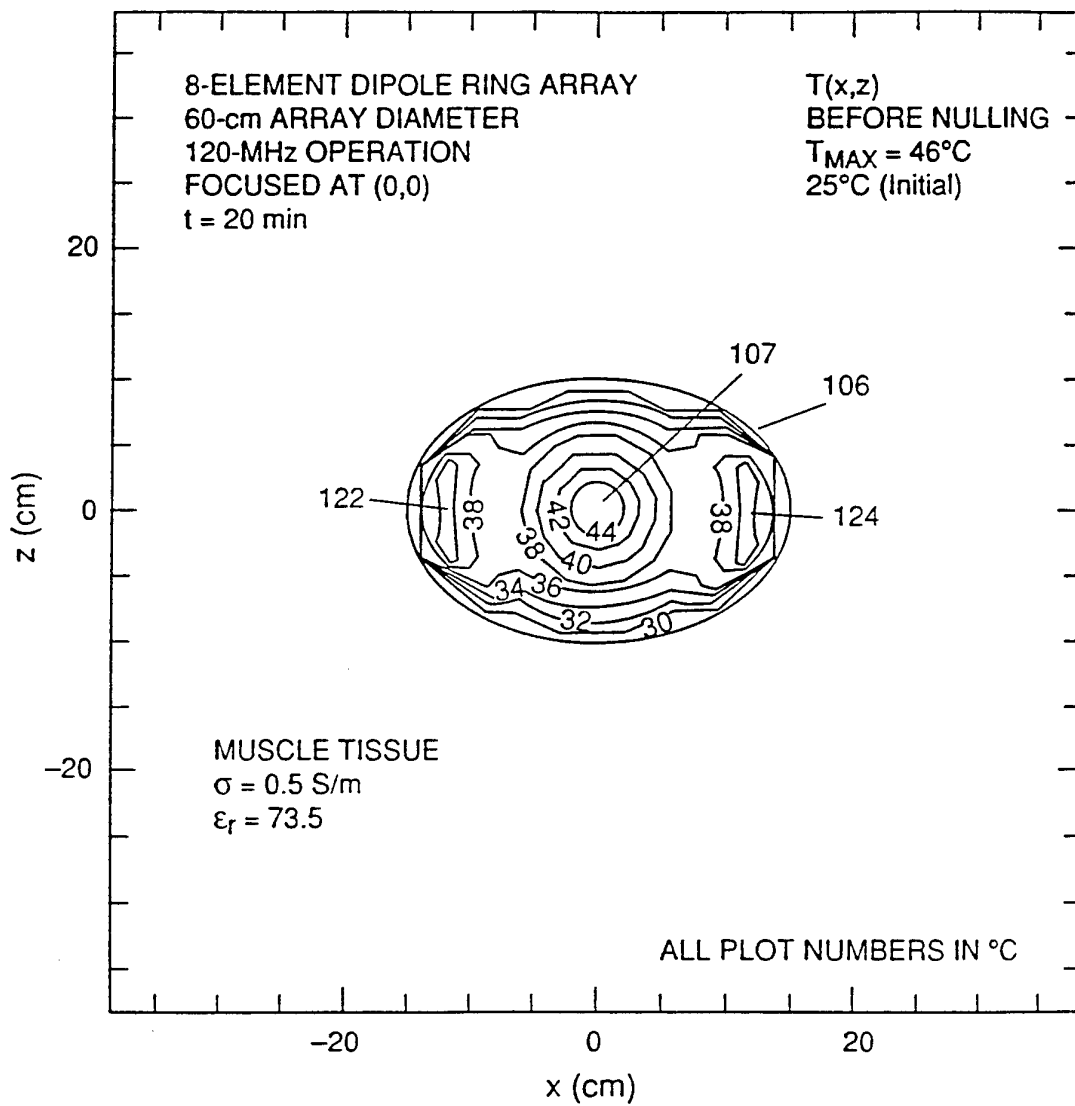


Fig. 29

31/69

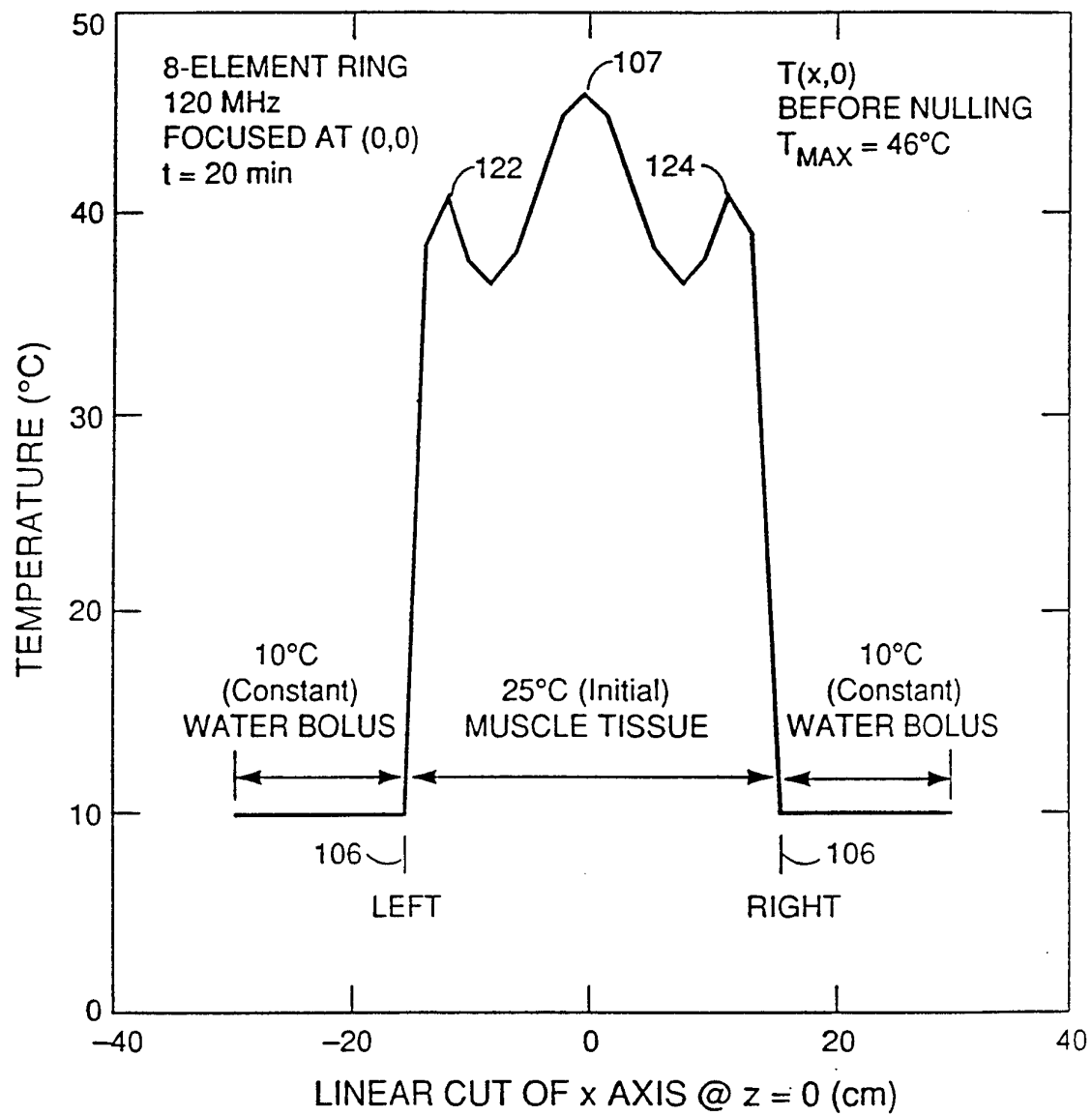


Fig. 30

32/69

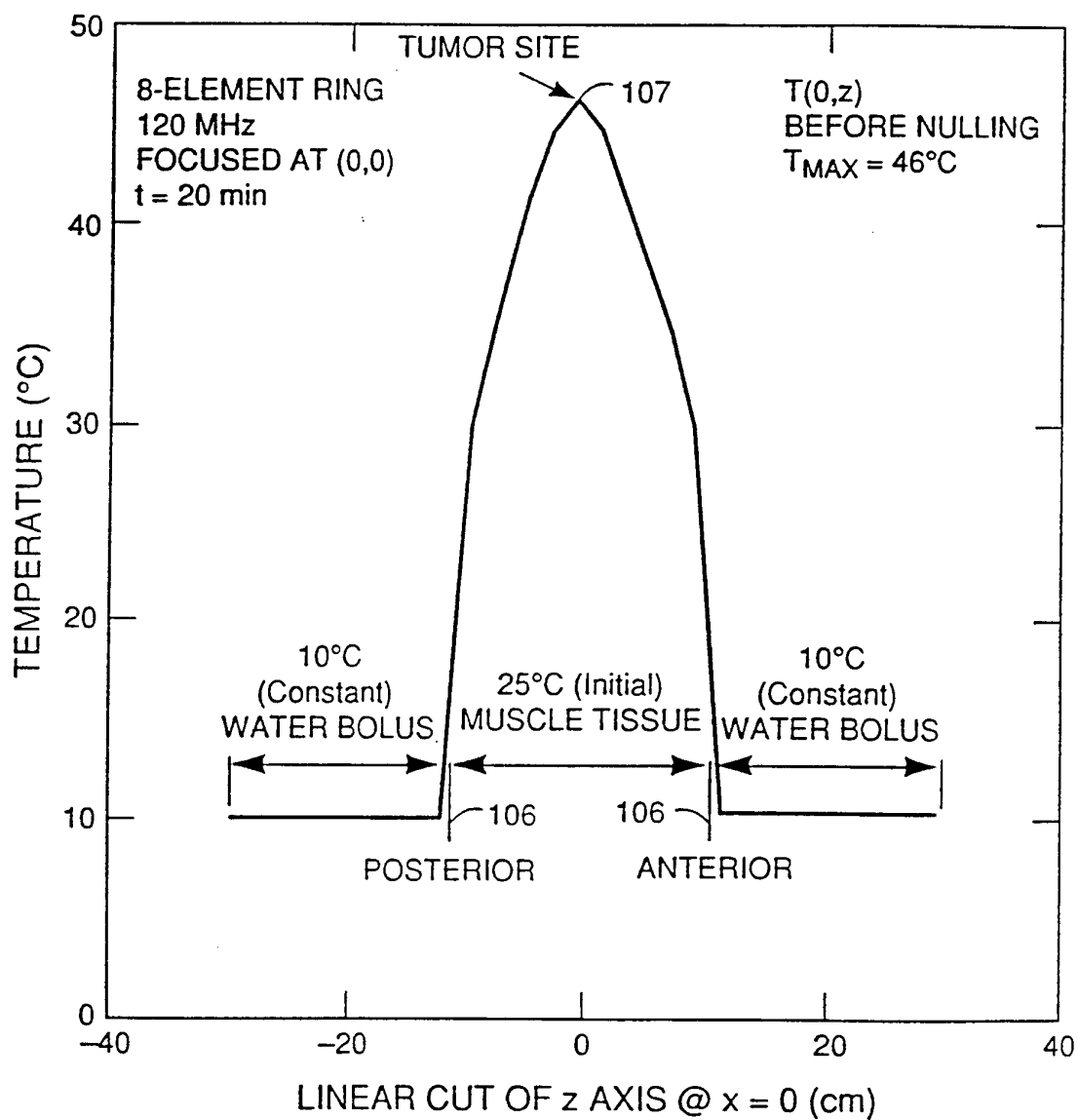


Fig. 31

33/69

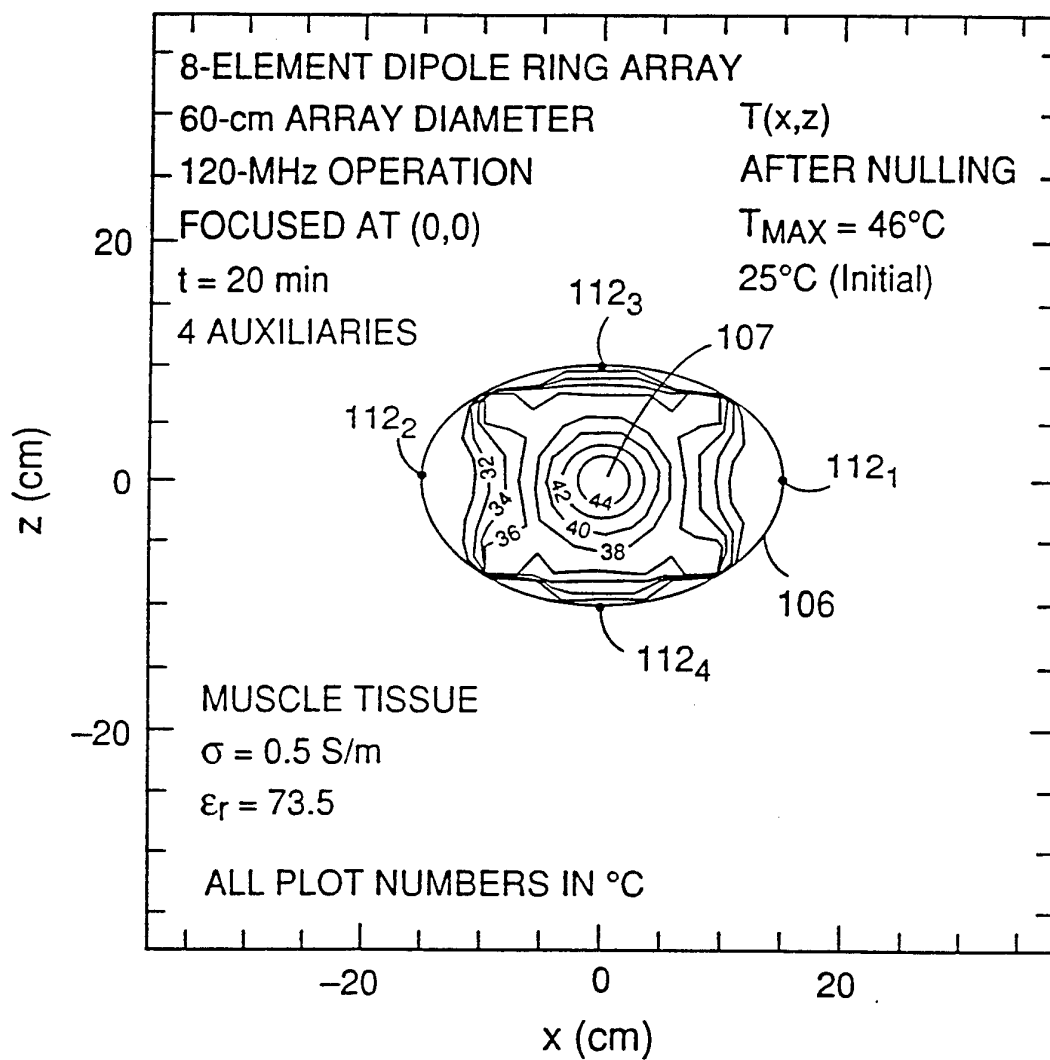


Fig. 32

34/69

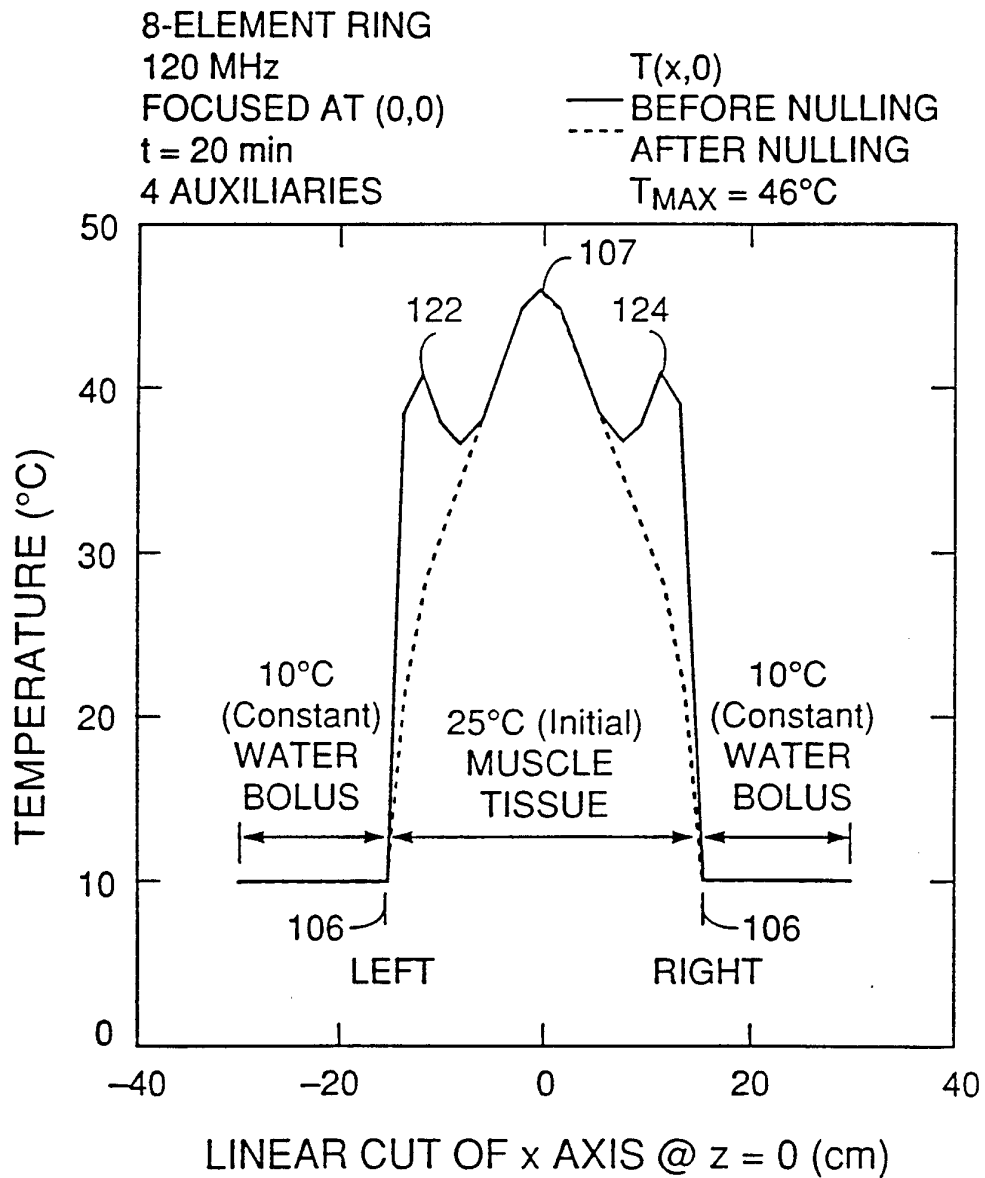


Fig. 33

35/69

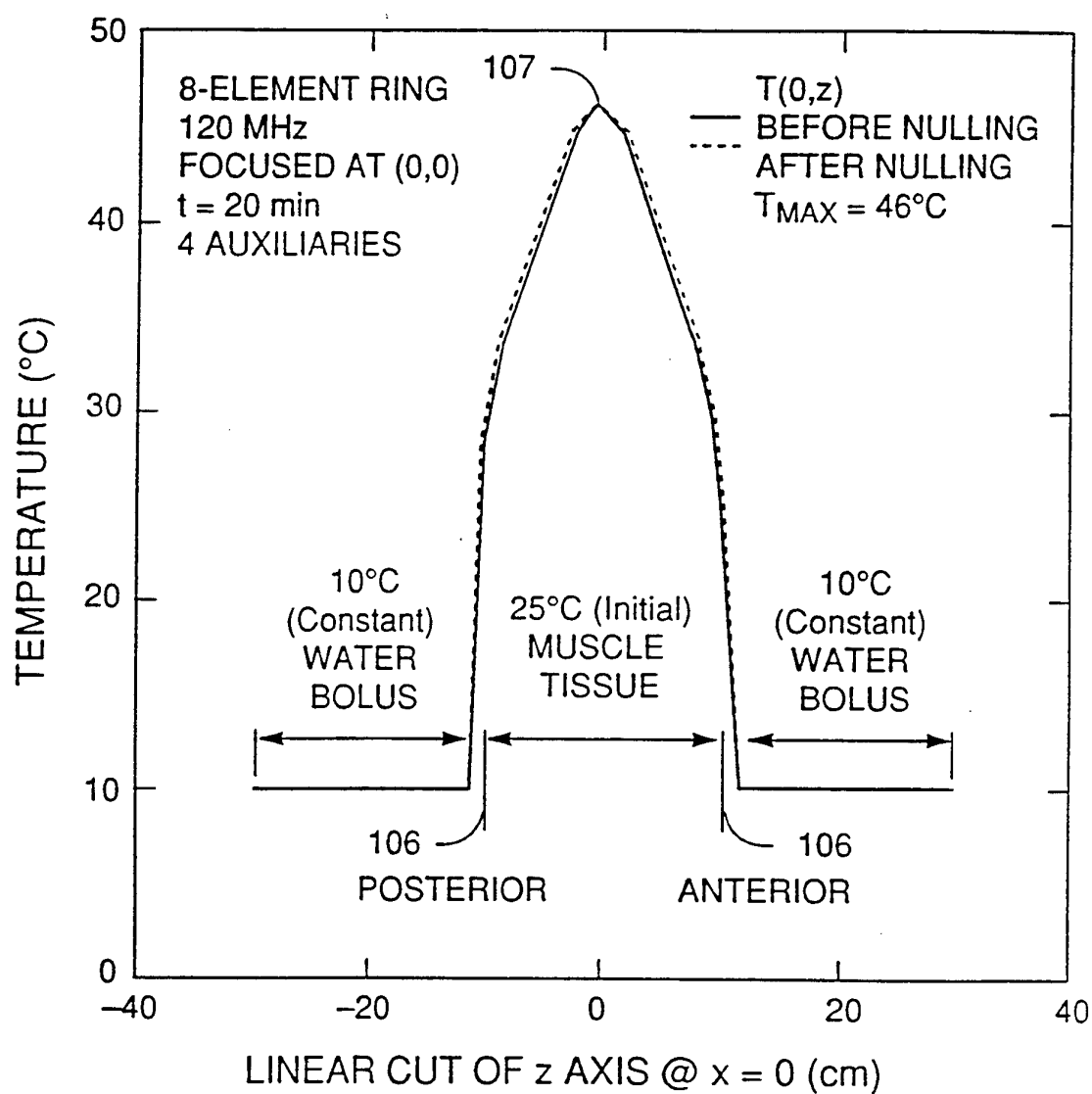


Fig. 34

36/69

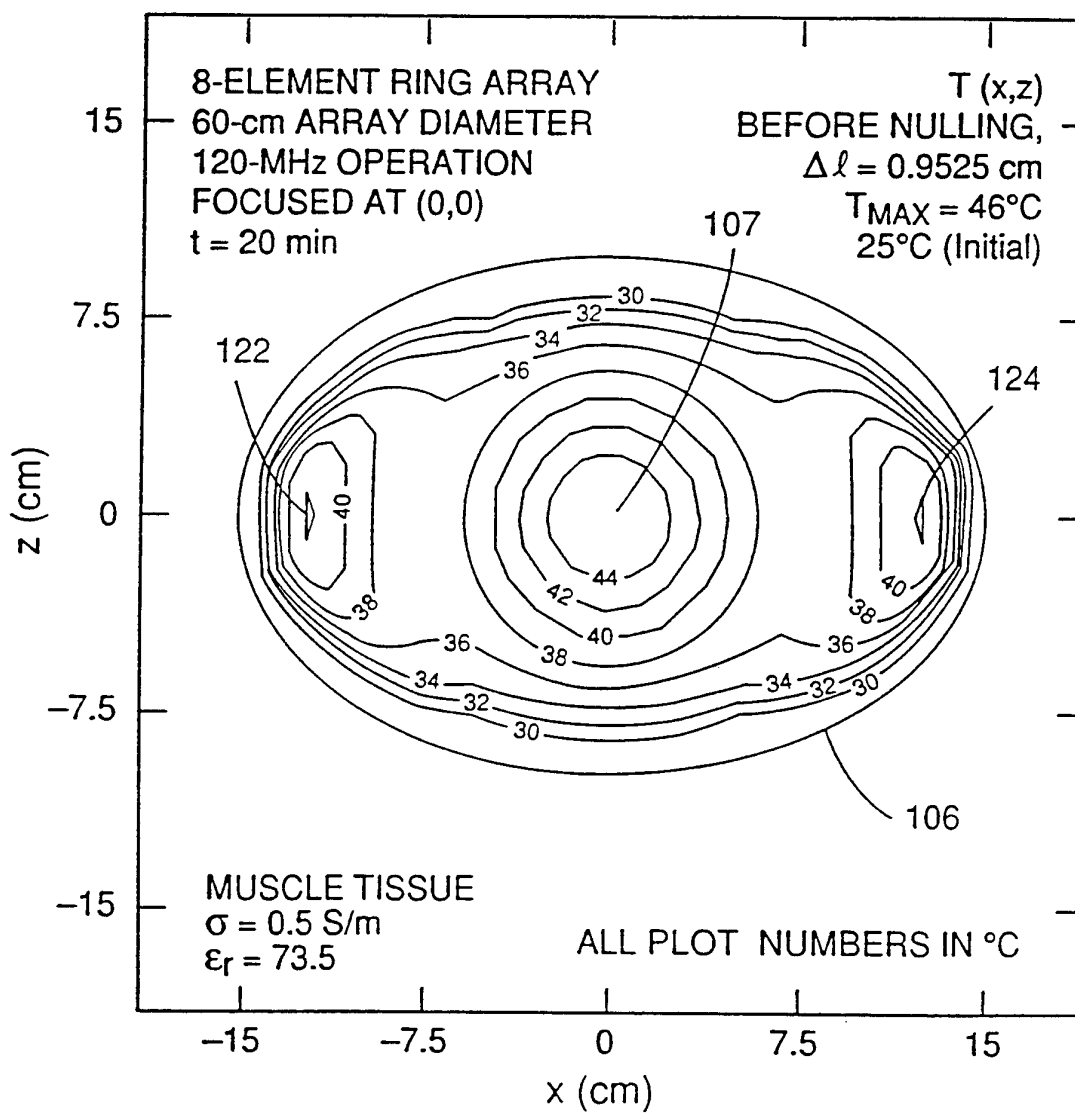


Fig. 35

37/69

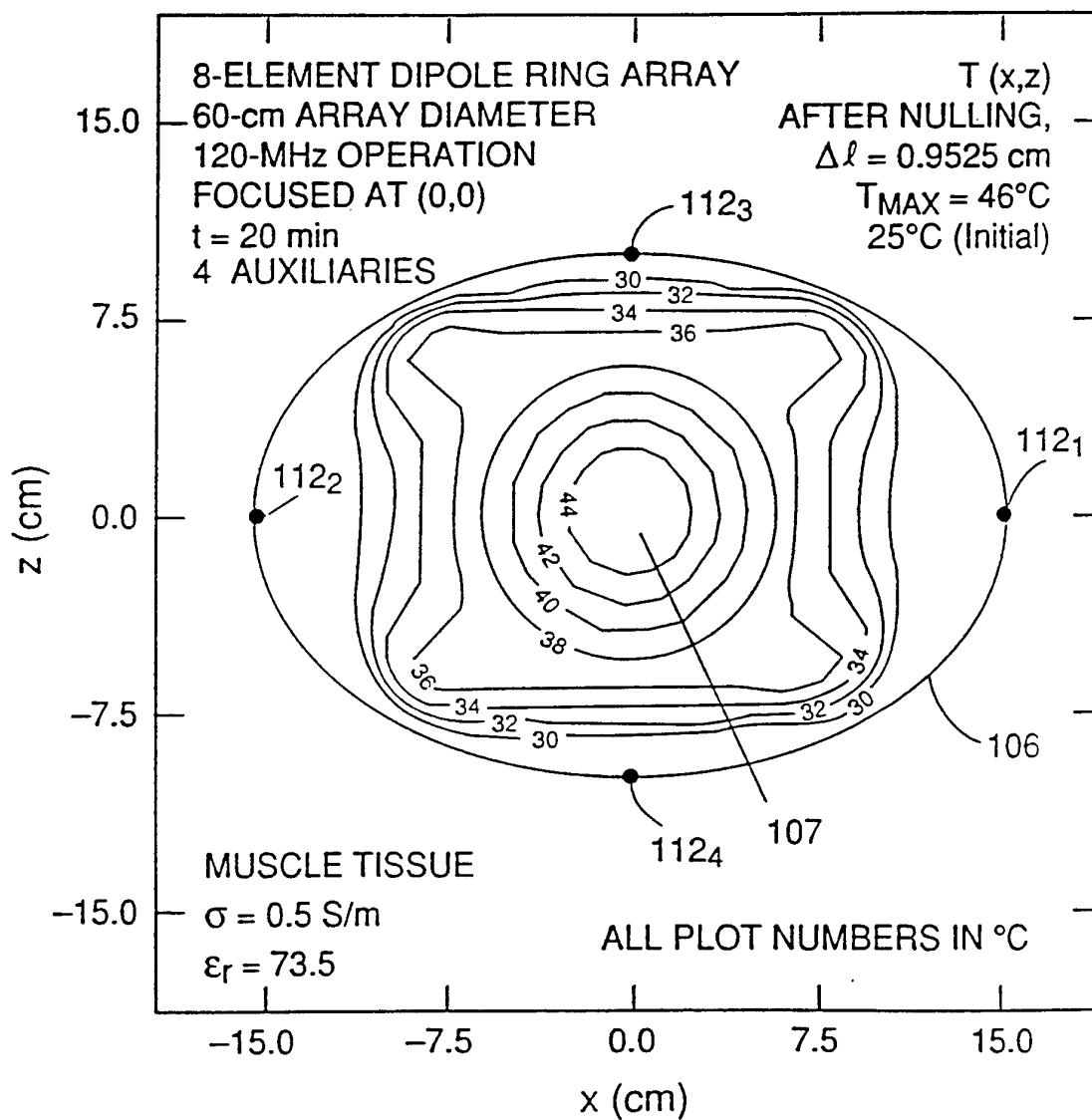


Fig. 36

38/69

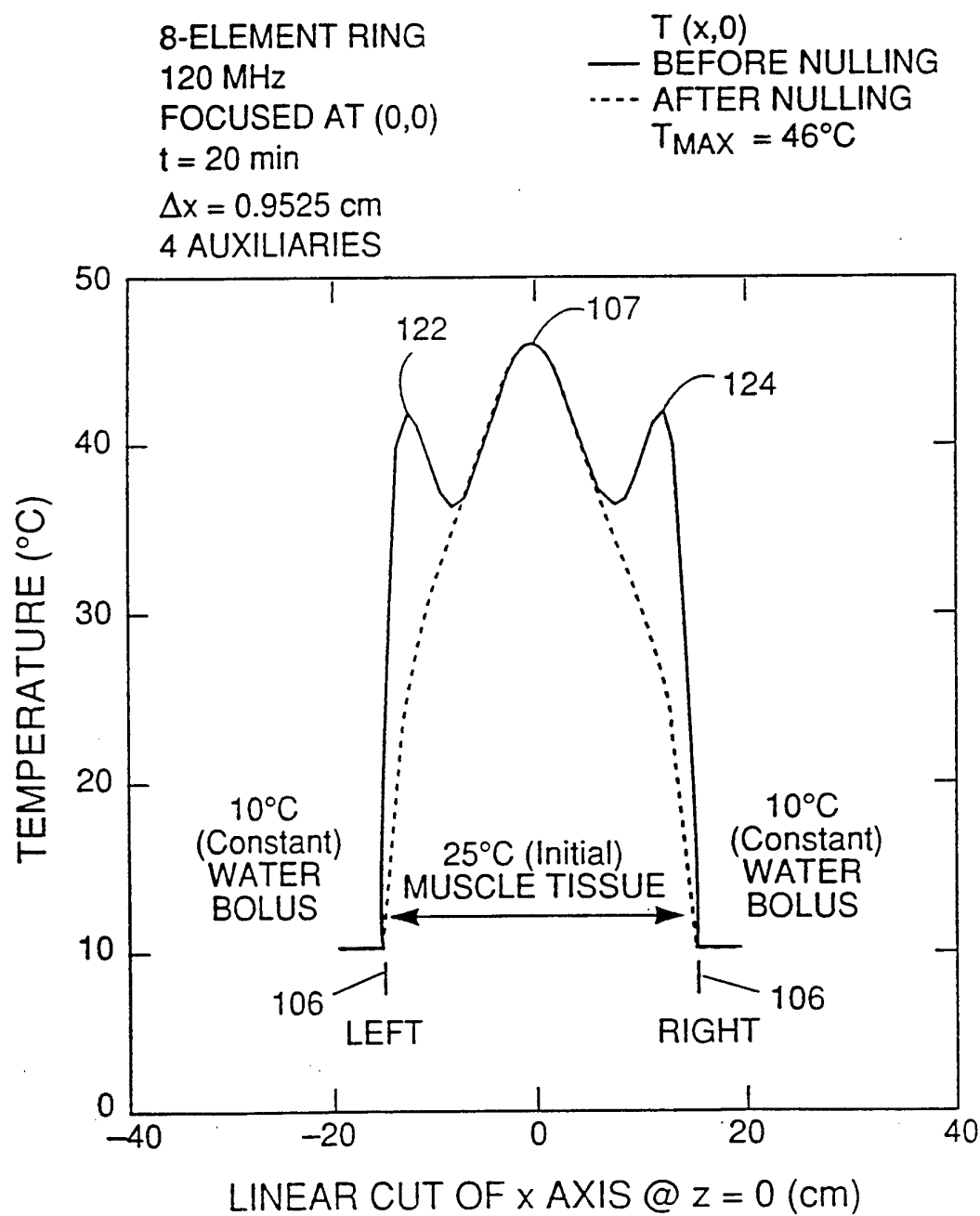


Fig. 37

39/69

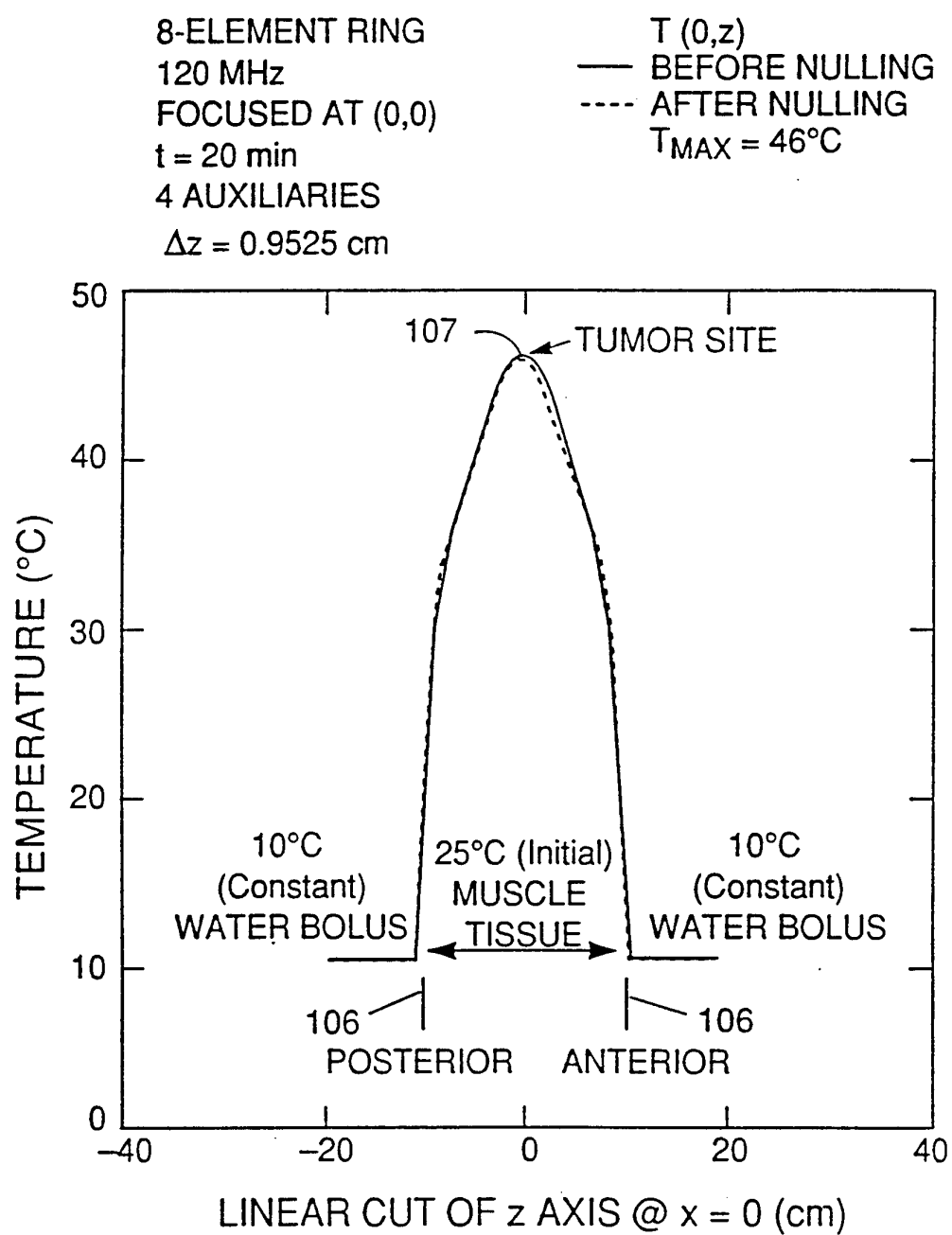


Fig. 38

40/69

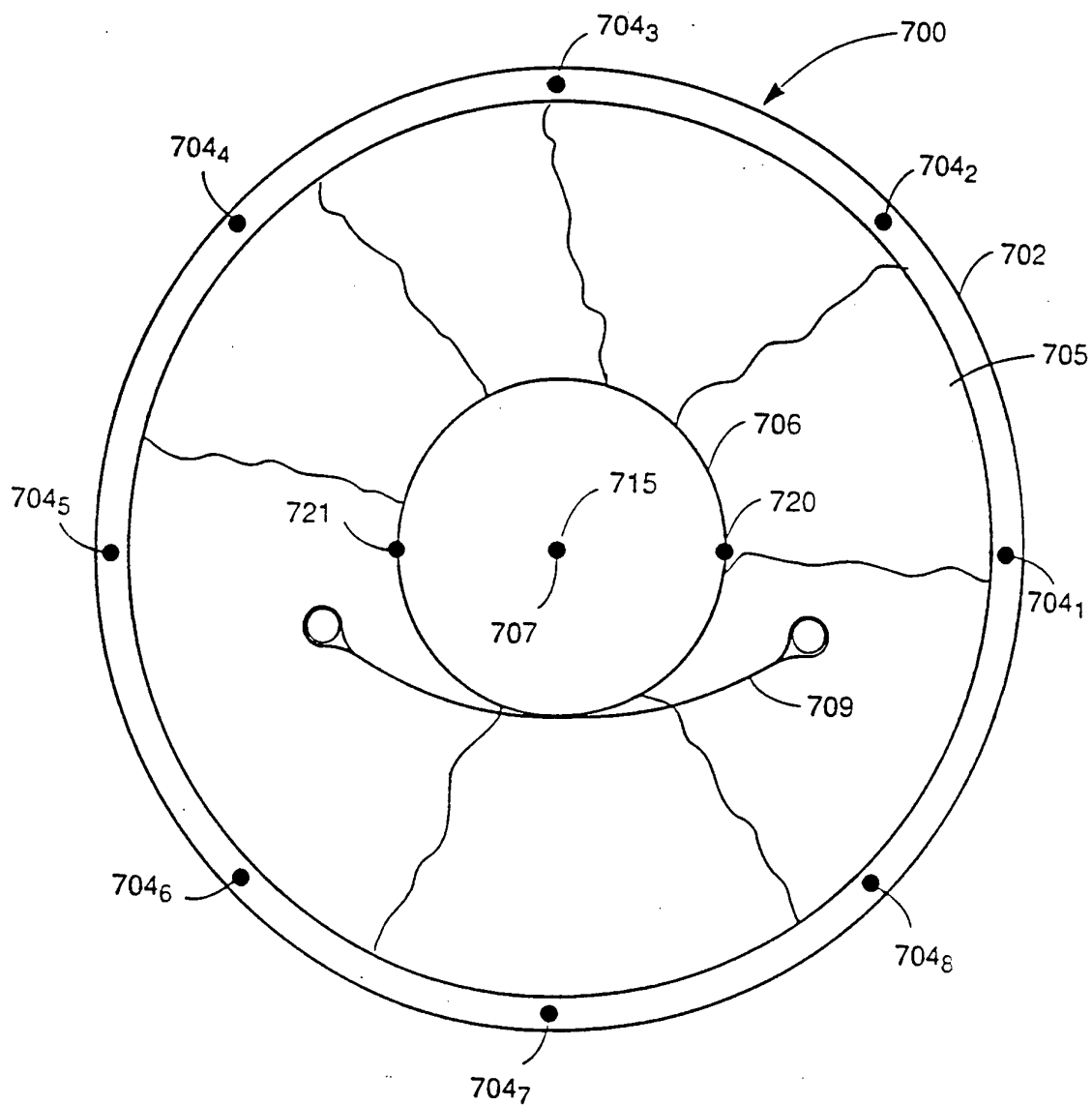
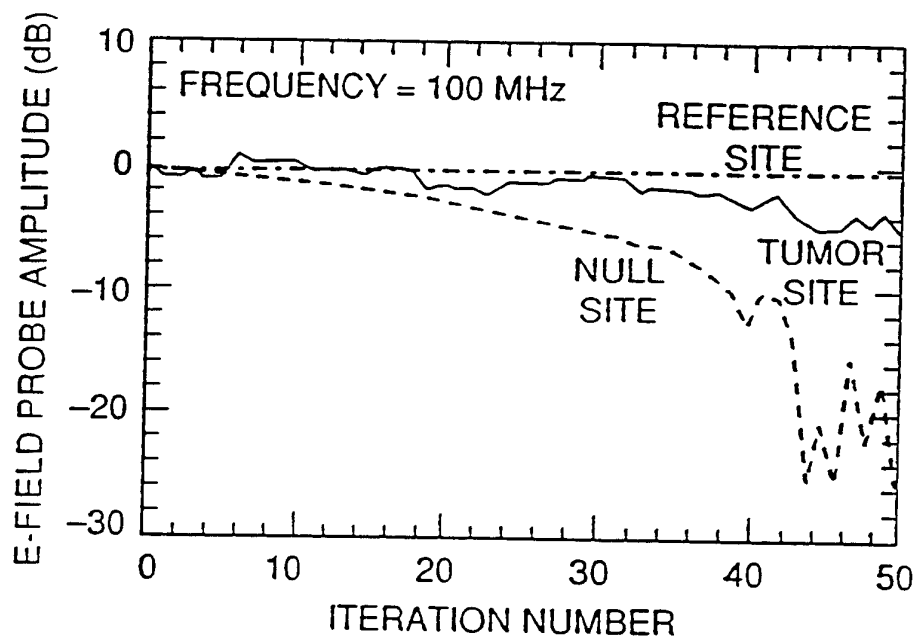
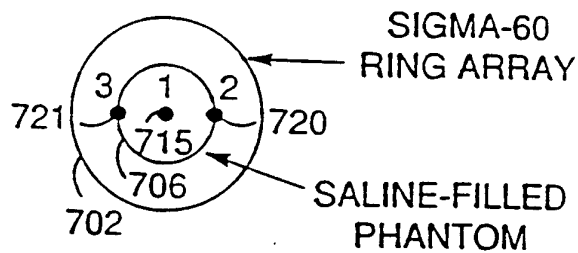


Fig. 39

41/69



EXPERIMENTAL CONFIGURATION



POSITION	COMMENT	PROBE
1	TUMOR SITE	EP-500
2	NULL SITE	EP-100
3	REF. SITE	EP-400

Fig. 40

42/69

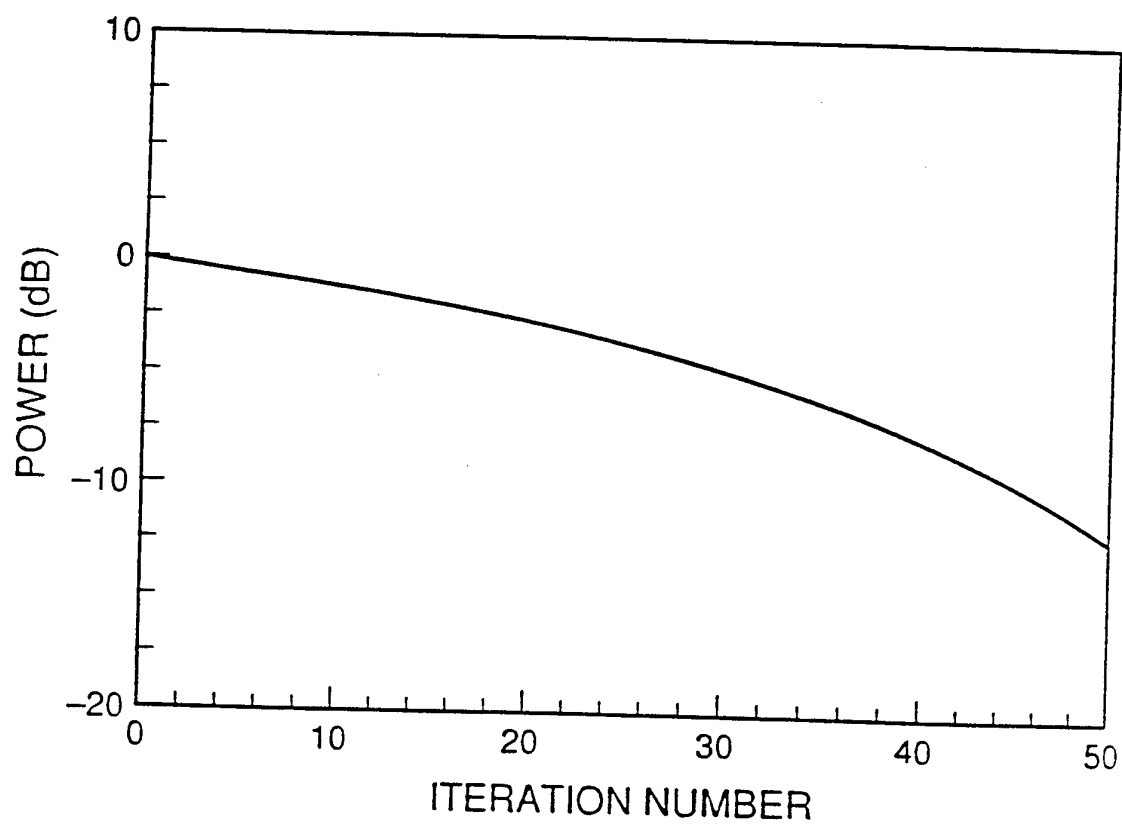


Fig. 41

43/69

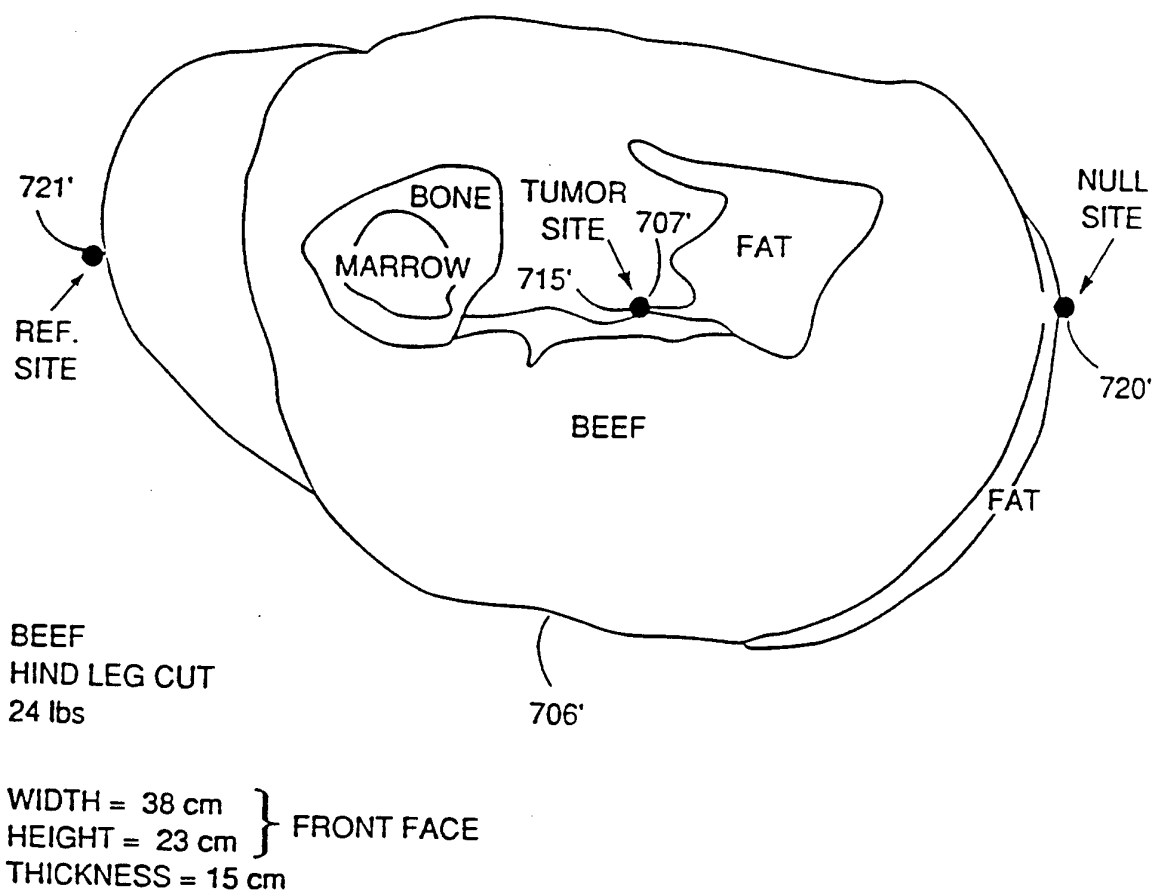
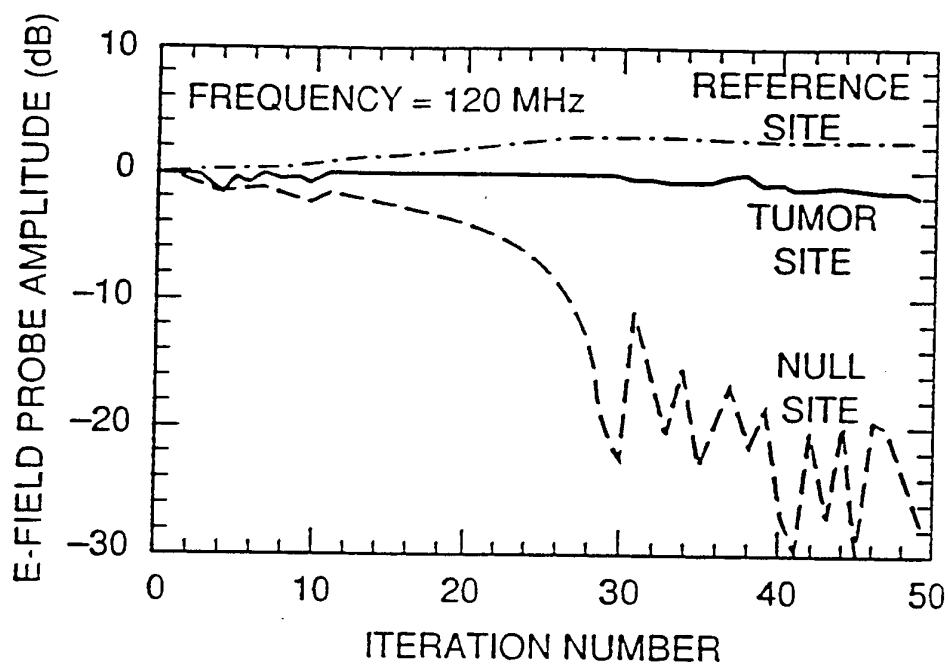
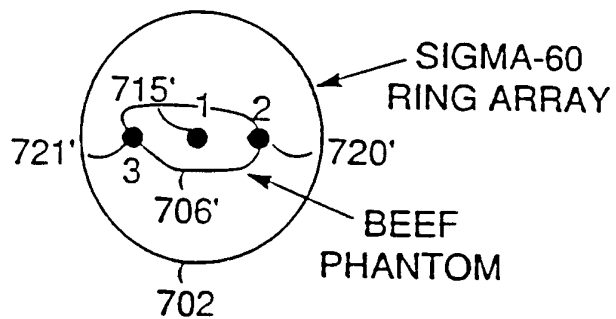


Fig. 42

44/69



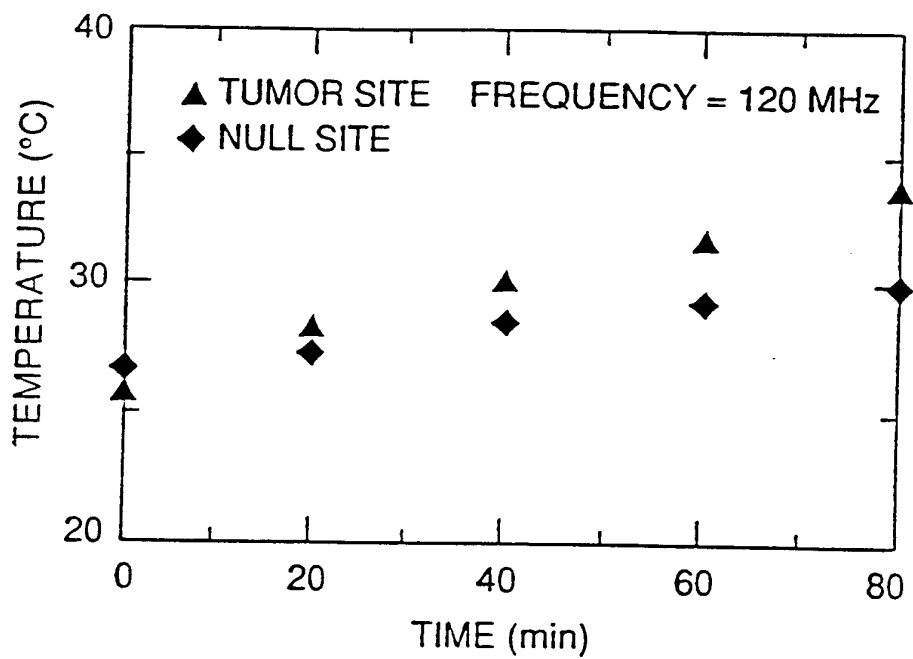
EXPERIMENTAL CONFIGURATION



POSITION	COMMENT	PROBE
1	TUMOR SITE	EP-500
2	NULL SITE	EP-100
3	REF. SITE	EP-400

Fig. 43

45/69



EXPERIMENTAL CONFIGURATION

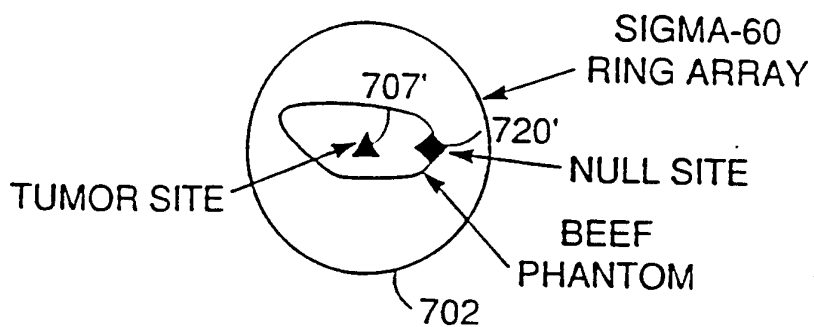
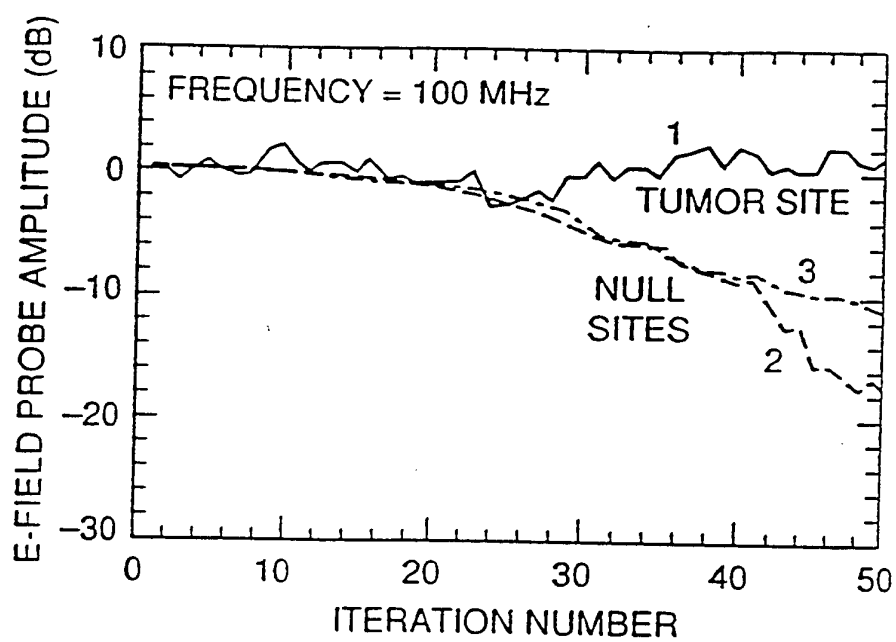
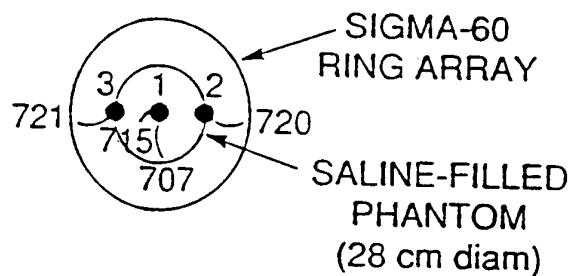


Fig. 44

46/69



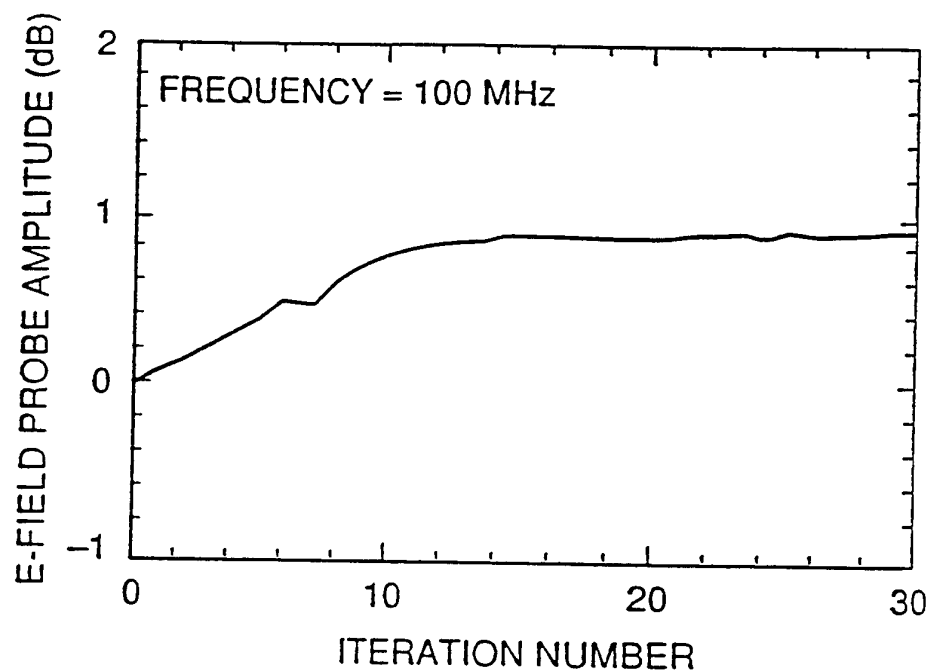
EXPERIMENTAL CONFIGURATION



POSITION	COMMENT	PROBE
1	TUMOR SITE	EP-500
2	NULL SITE	EP-100
3	NULL SITE	EP-100

Fig. 45

47/69



EXPERIMENTAL CONFIGURATION

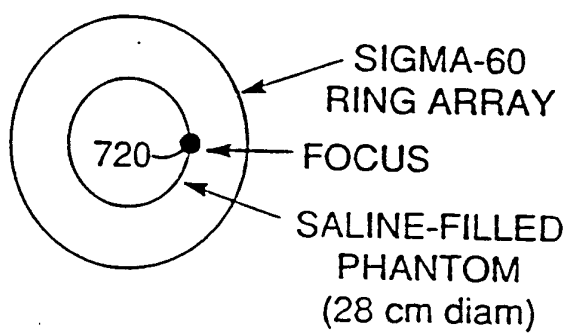


Fig. 46

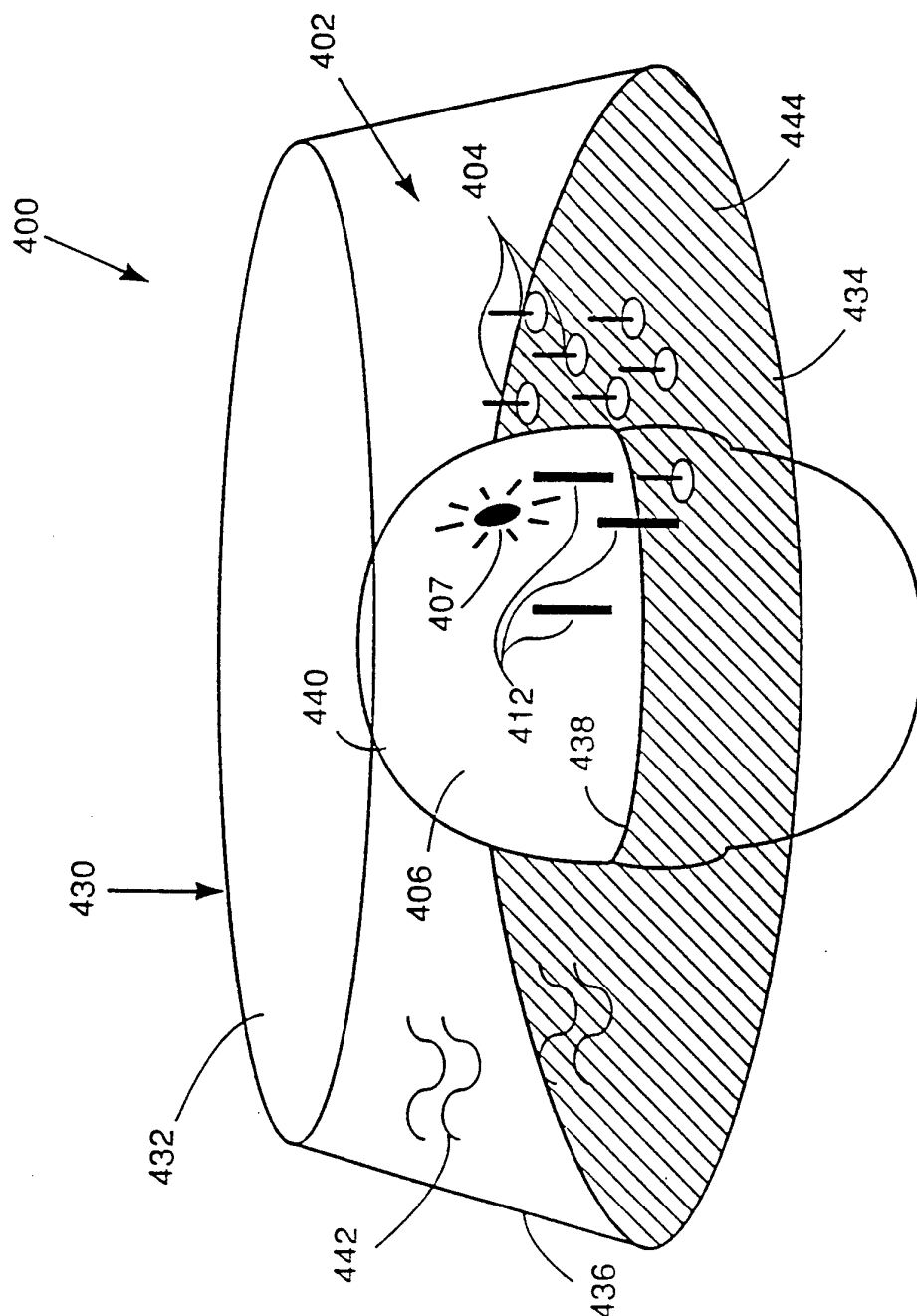


Fig. 47

49/69

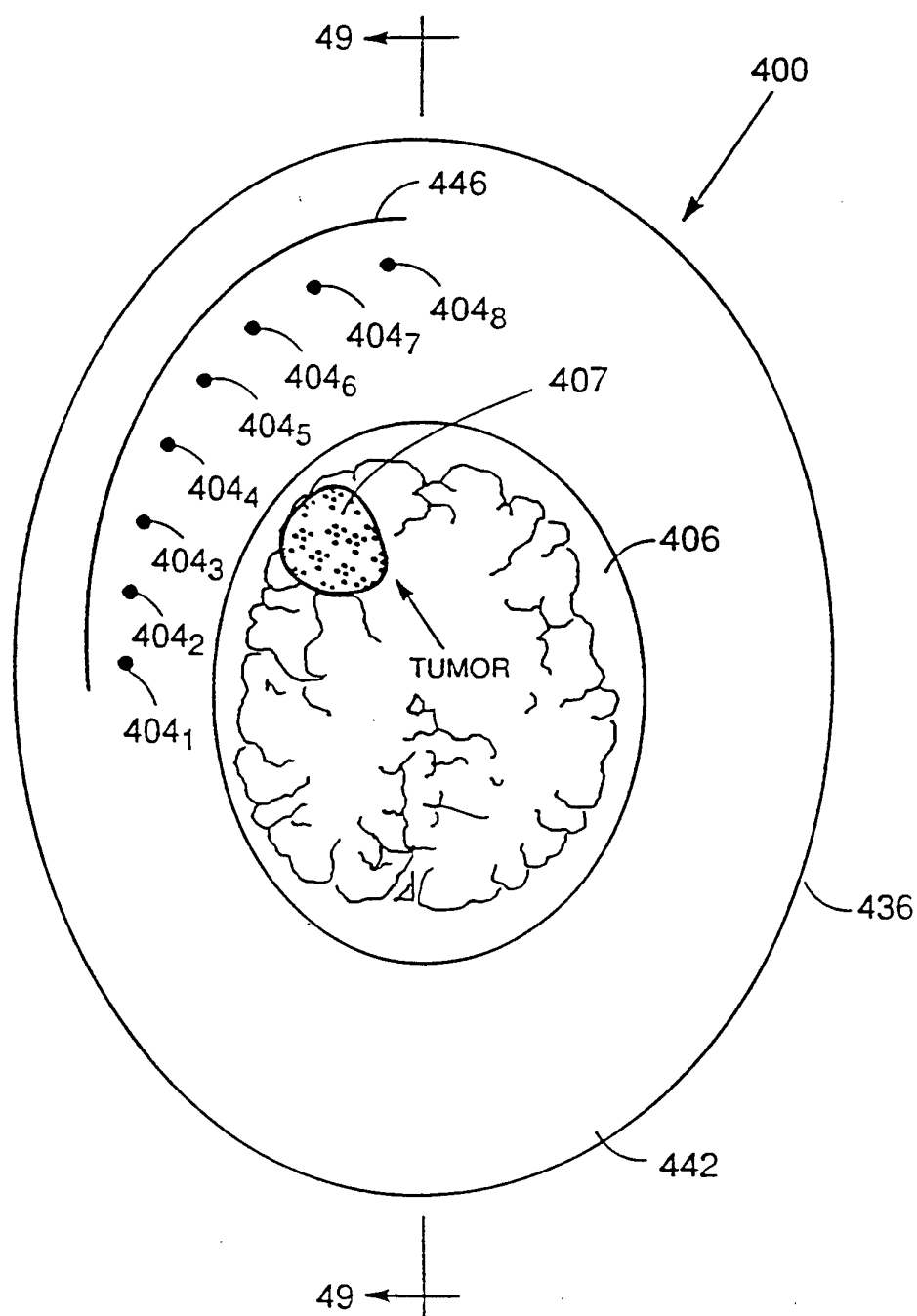


Fig. 48

SUBSTITUTE SHEET (RULE 26)

50/69

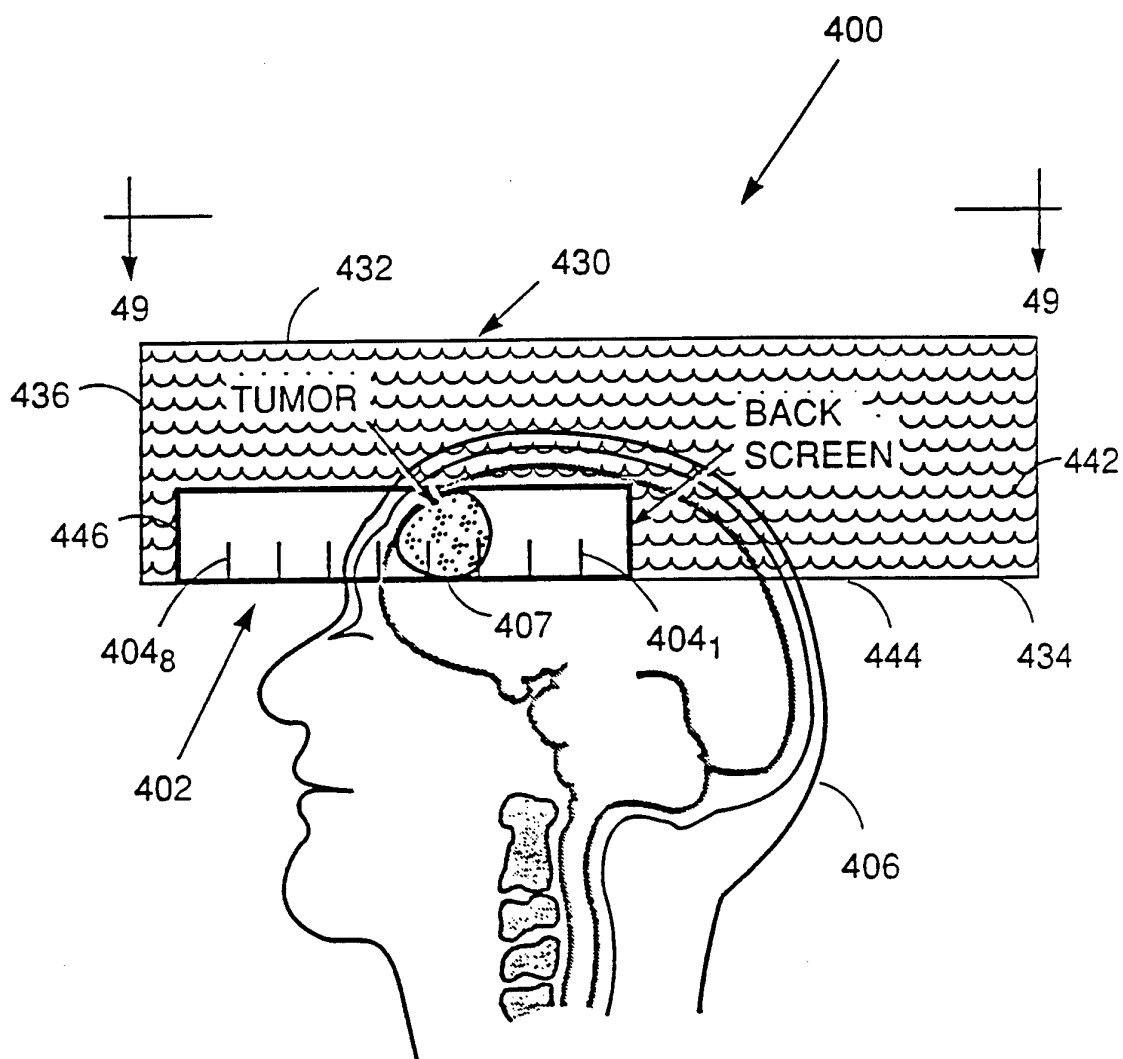


Fig. 49

51/69

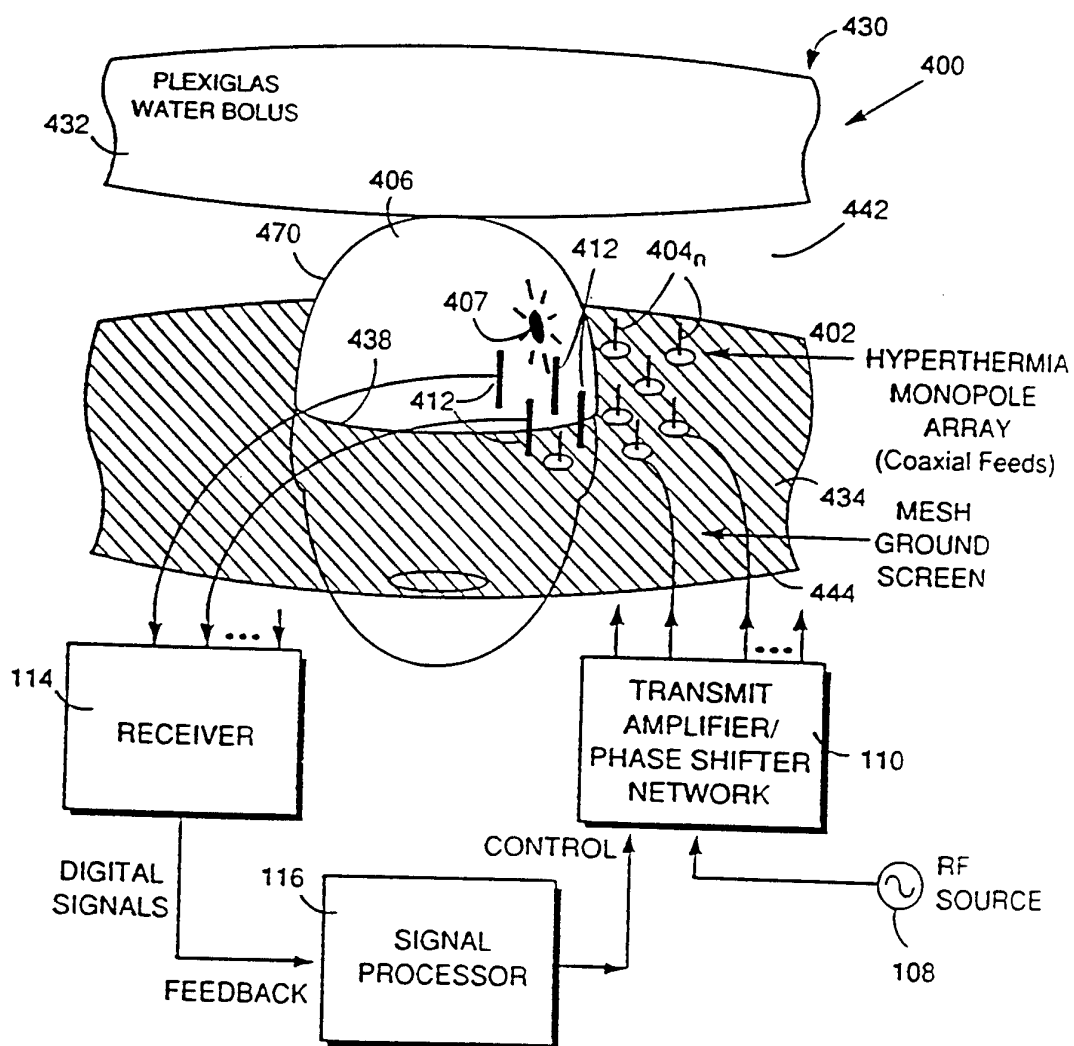


Fig. 50

52/69

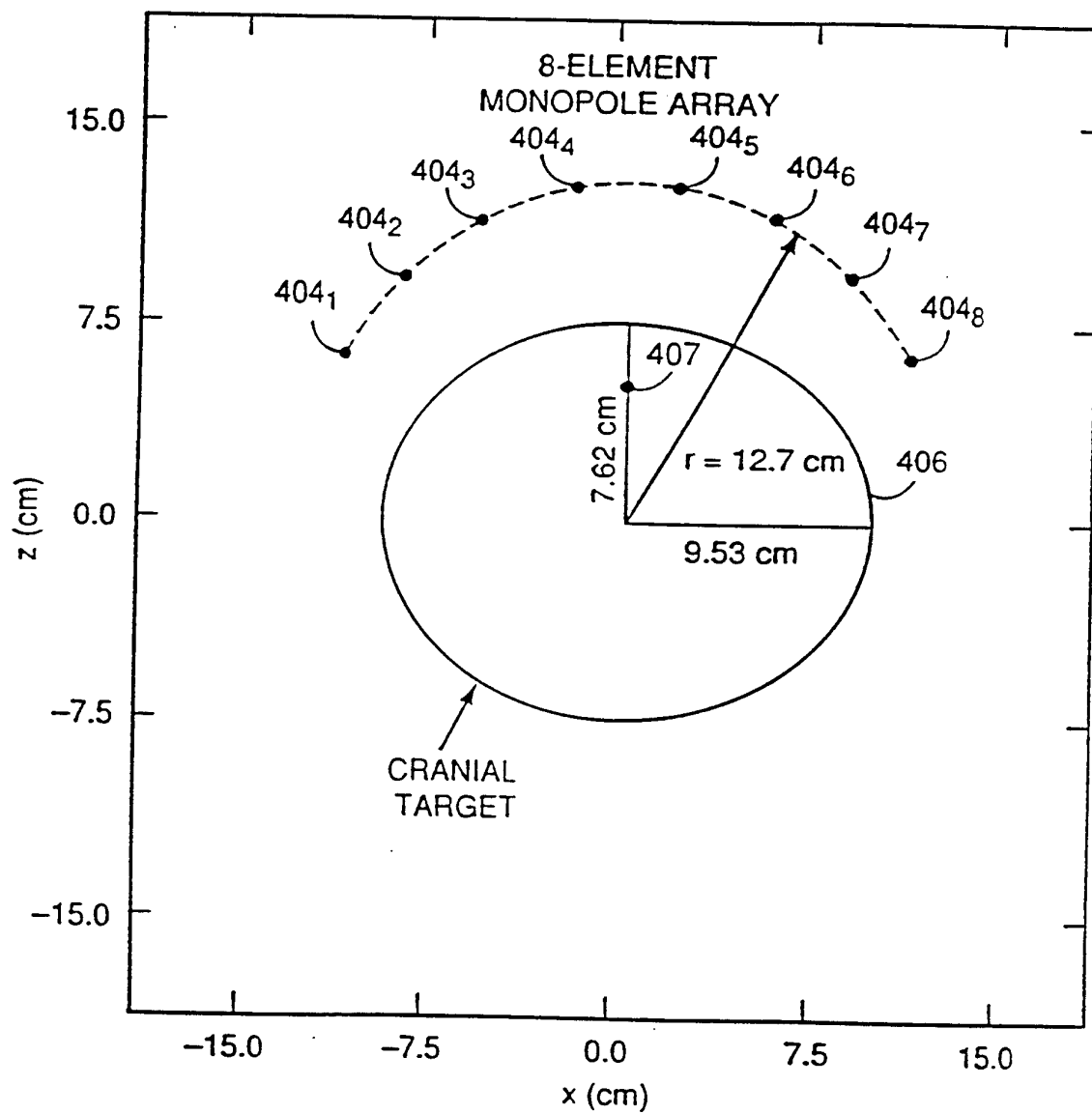


Fig. 51

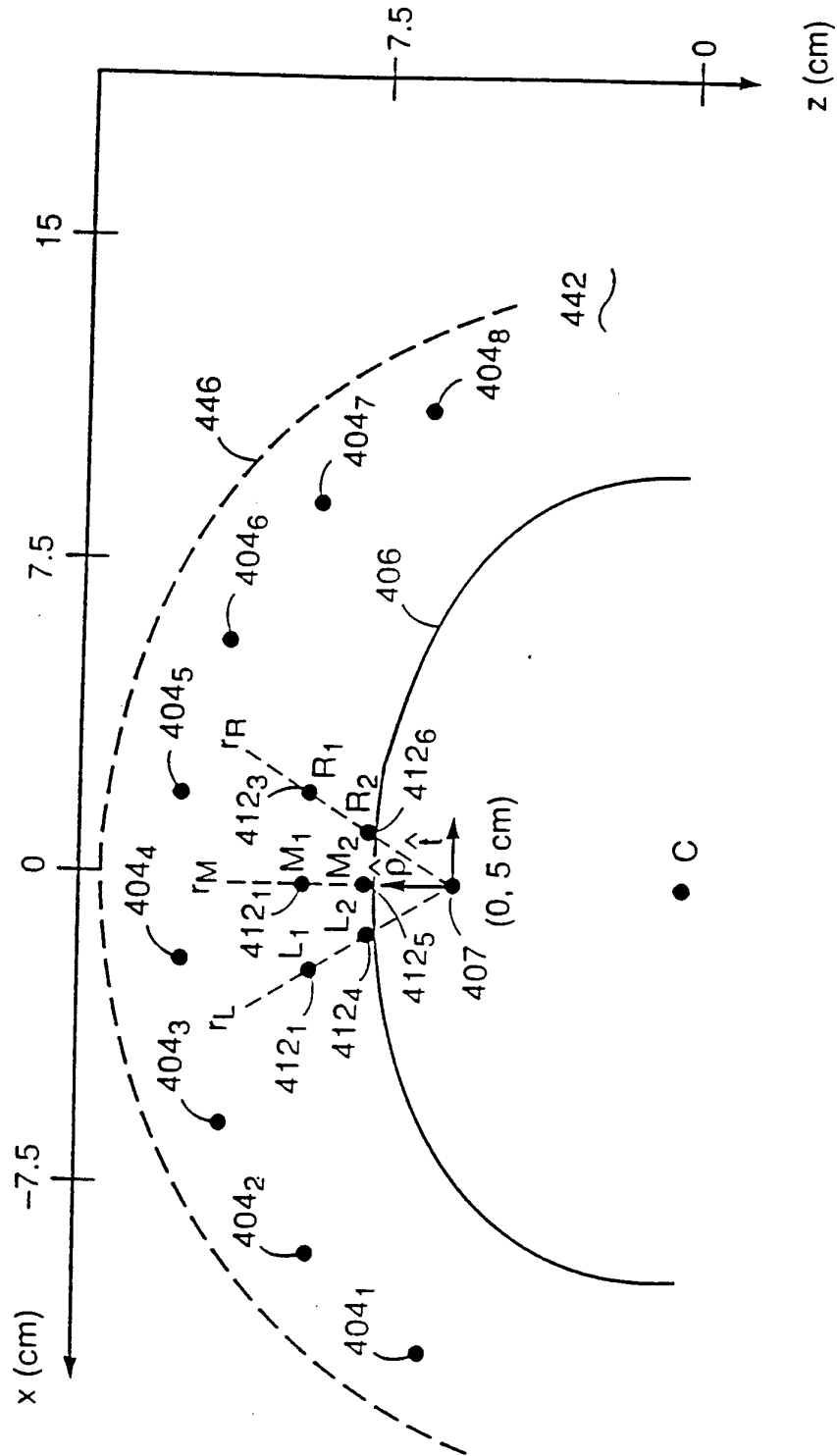


Fig. 52

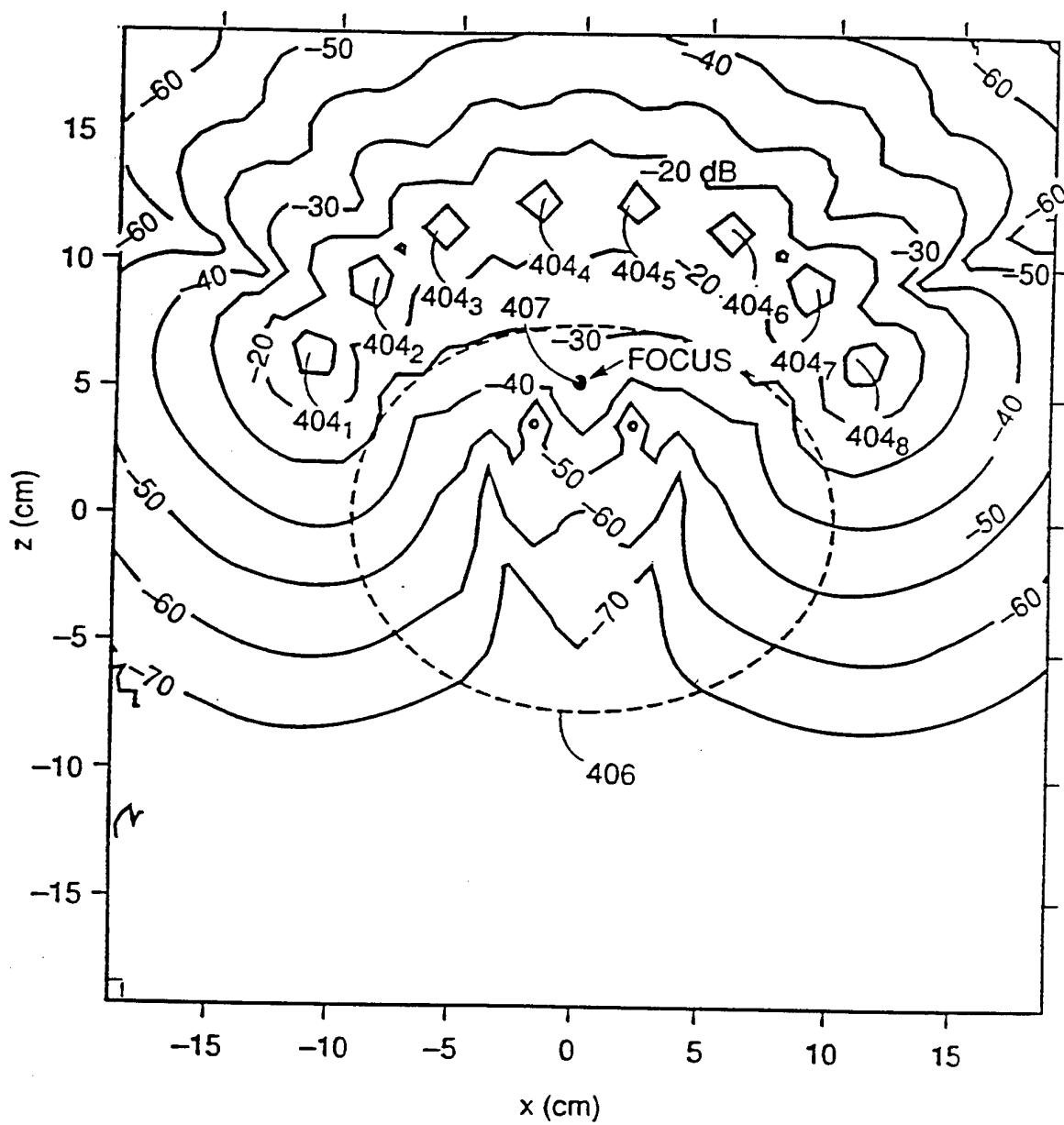


Fig. 53

55/69

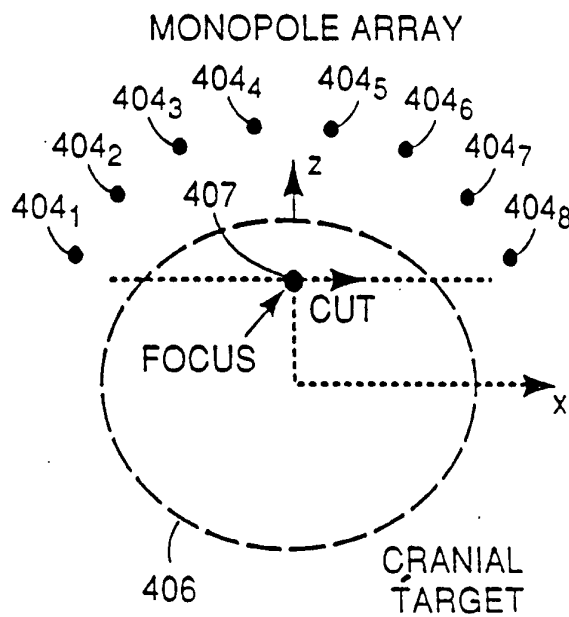
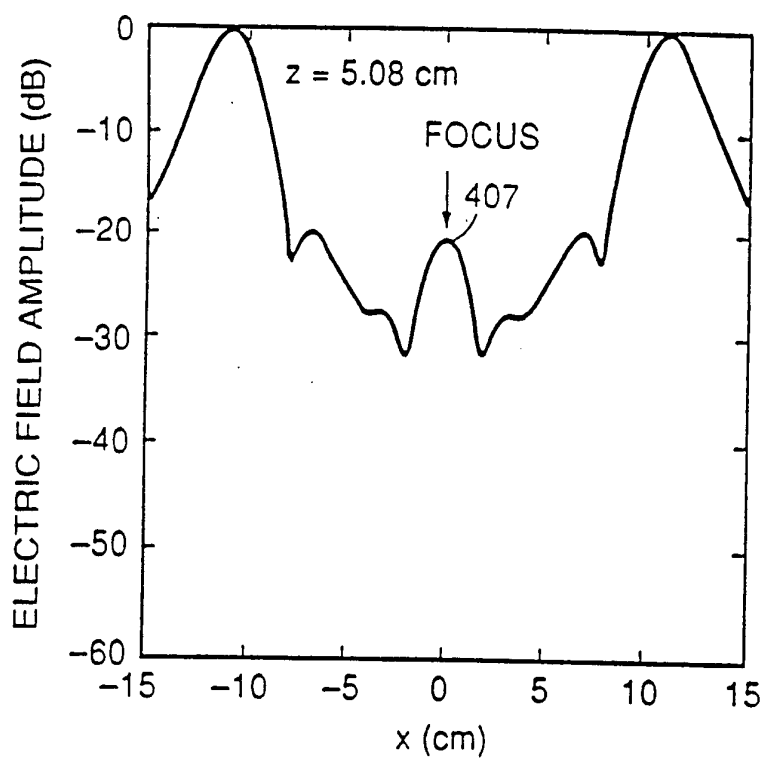
FOCUS AT $z = 5.08$ cm, 915 MHz, $\epsilon_r = 50$, $\sigma = 1.3$ S/m

Fig. 54

56/69

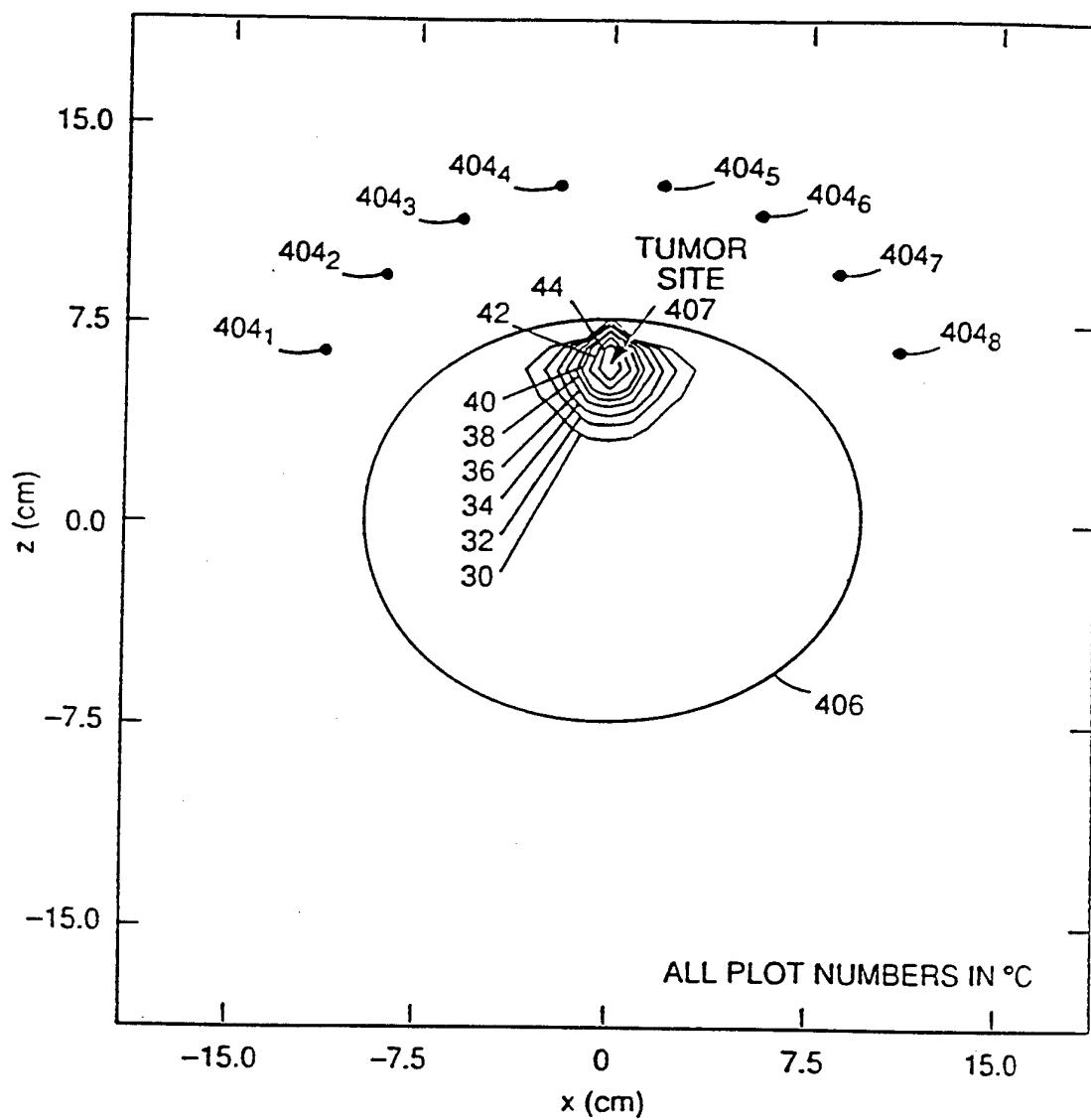


Fig. 55

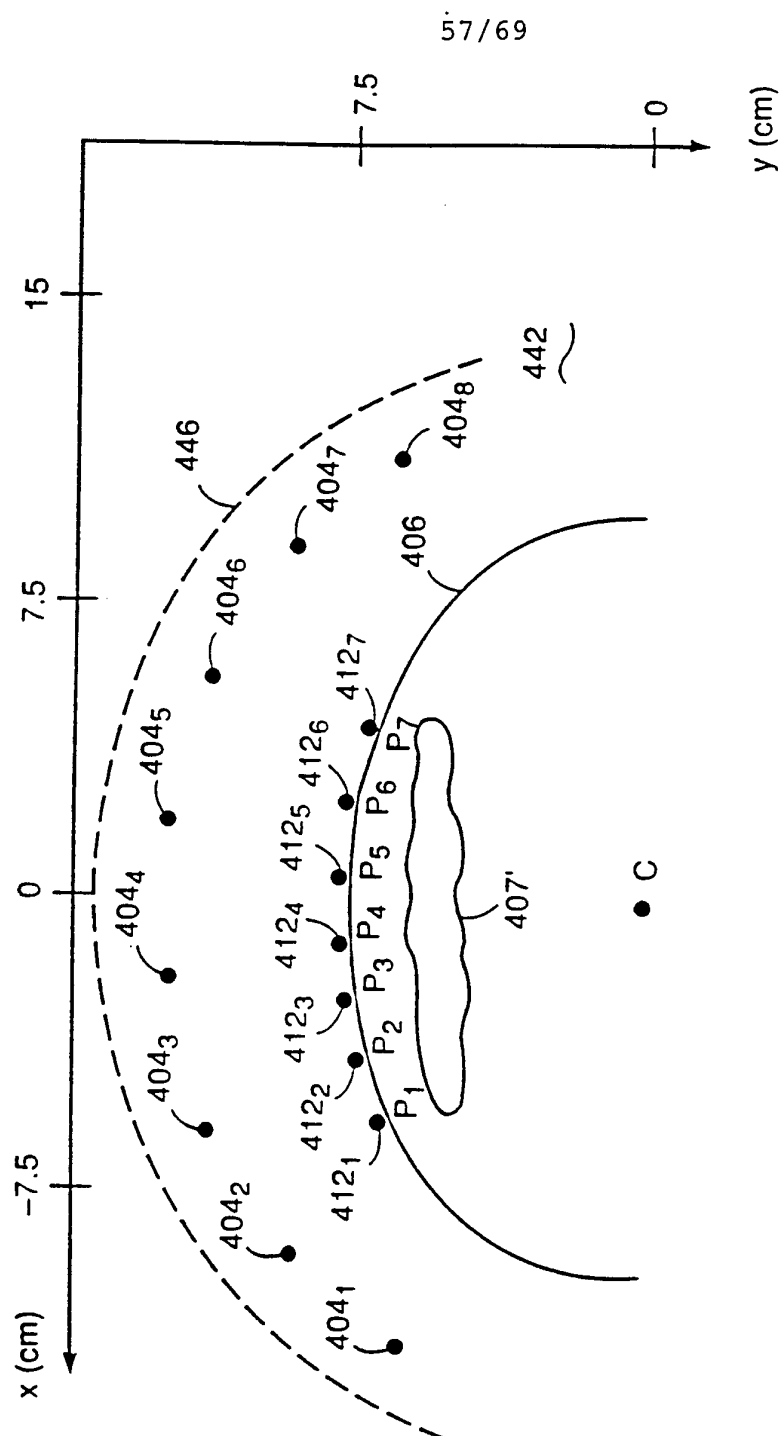


Fig. 56

58/69

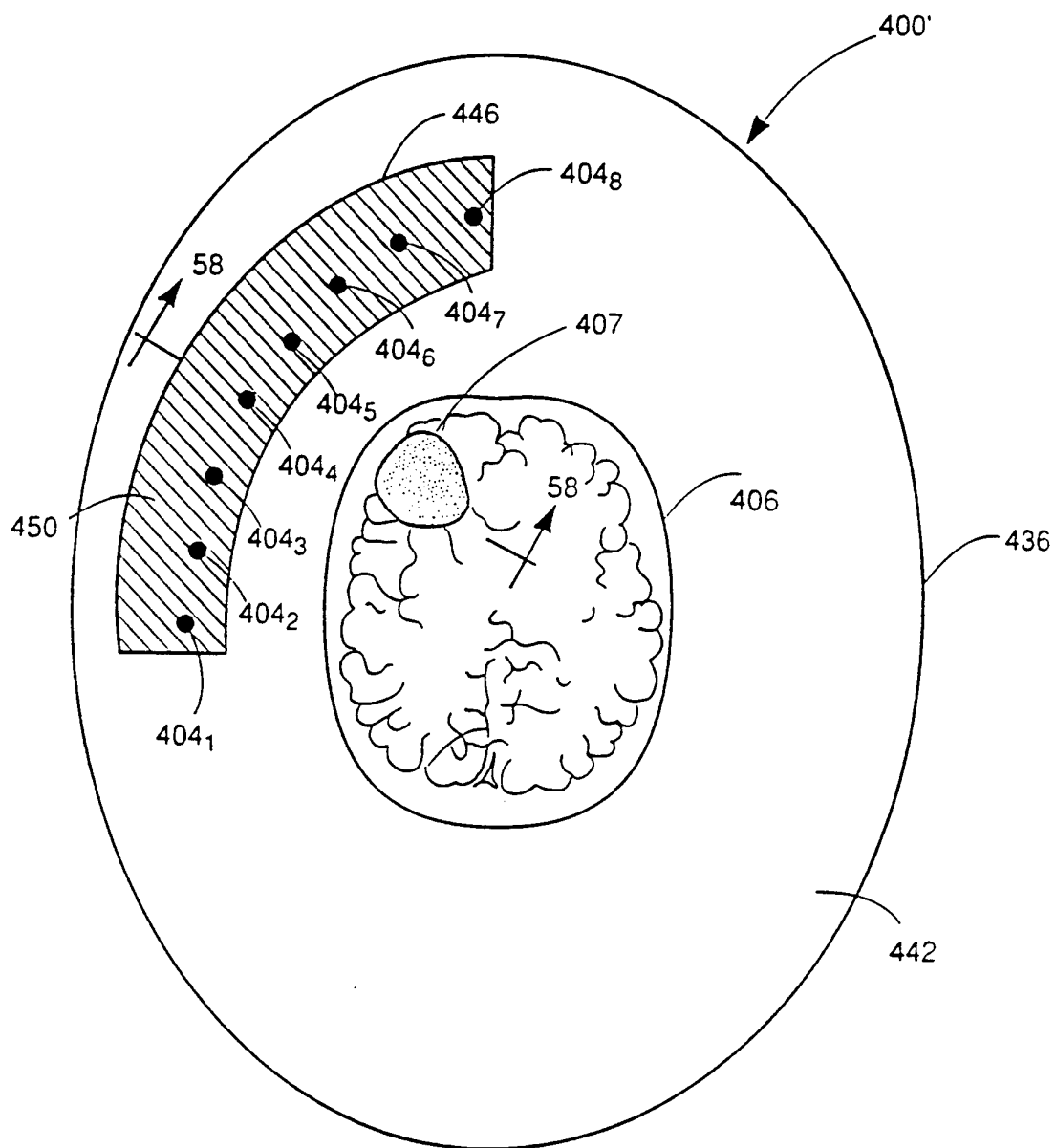


Fig. 57

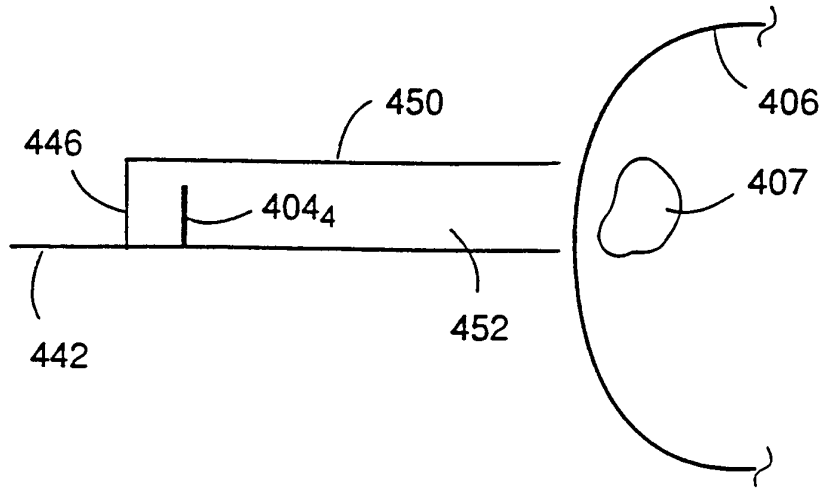


Fig. 58A

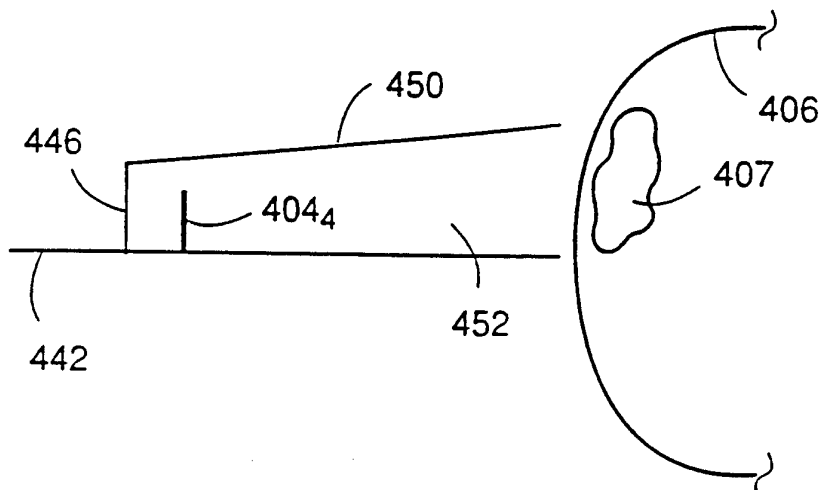


Fig. 58B

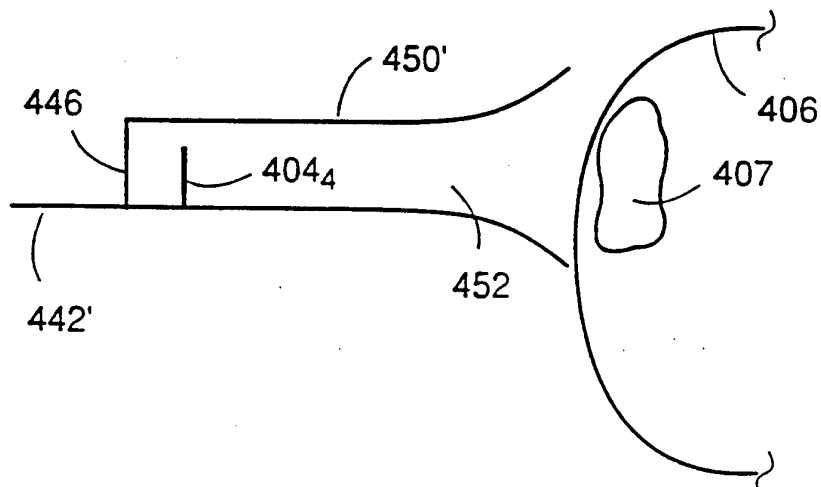


Fig. 58C

60/69

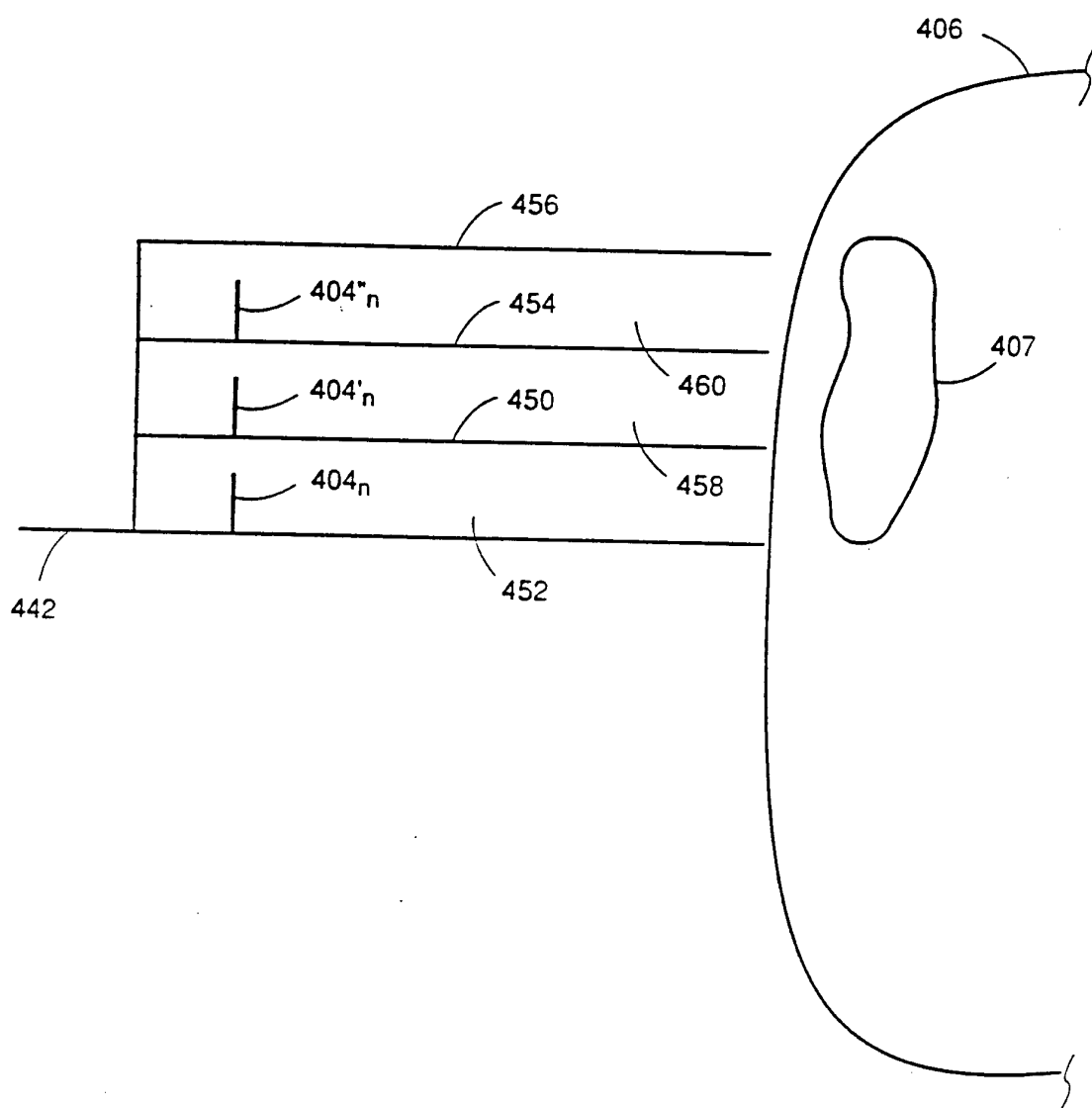


Fig. 59

61/69

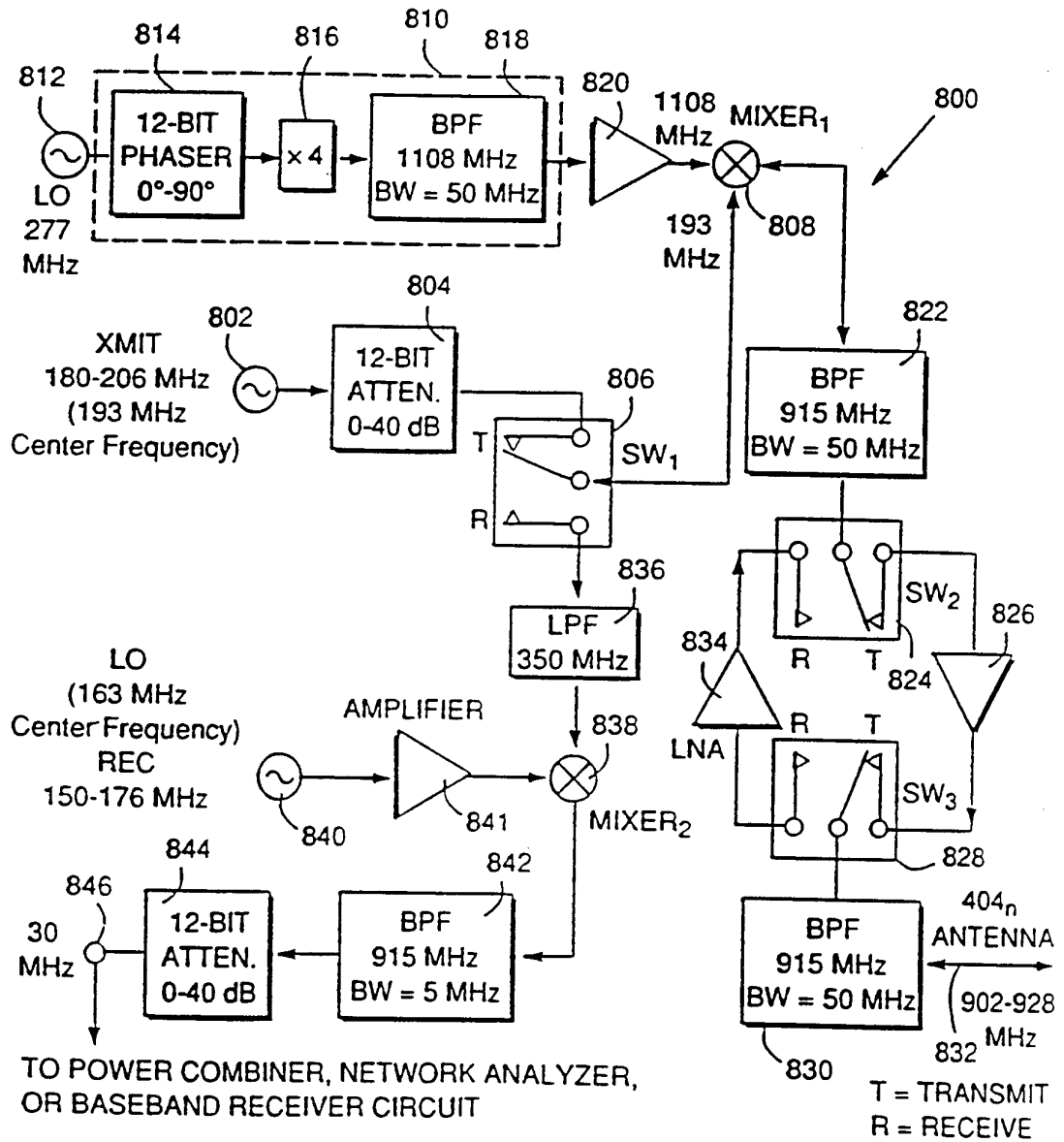


Fig. 60

62/69

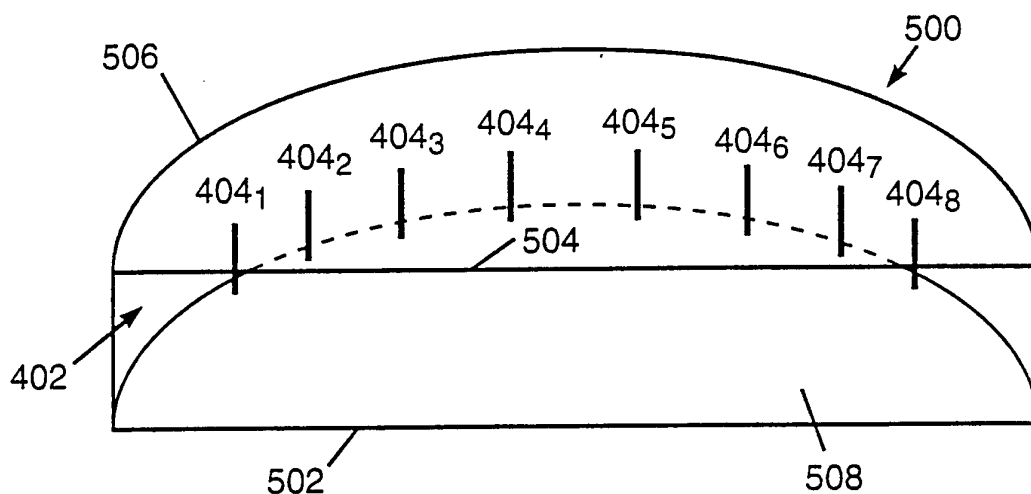


FIG. 61

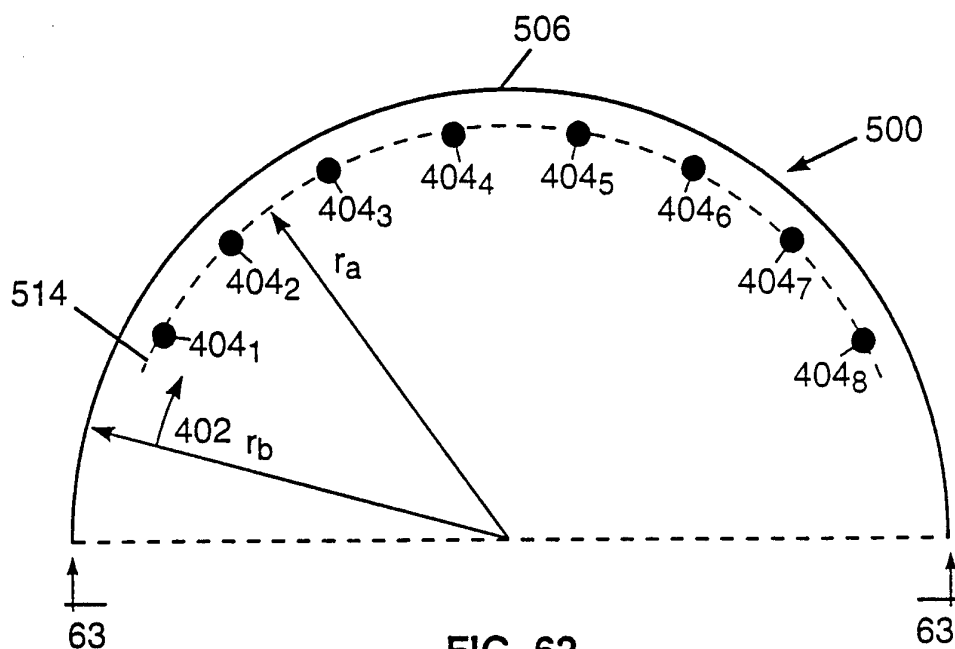


FIG. 62

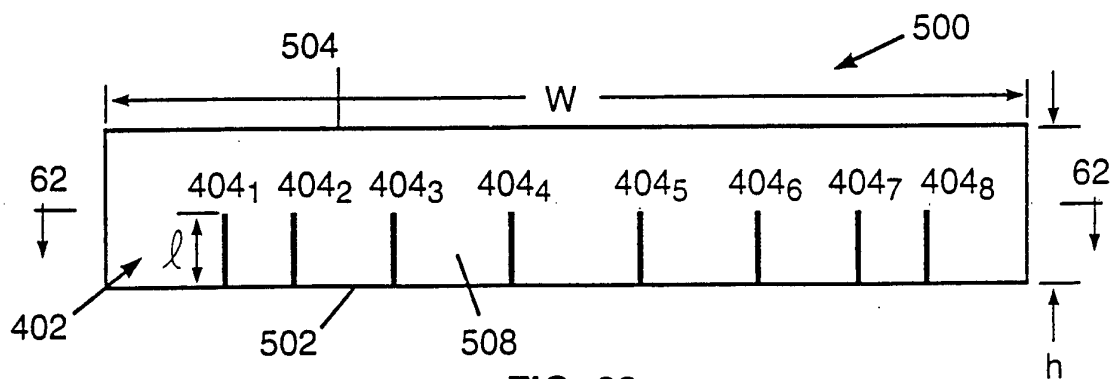


FIG. 63

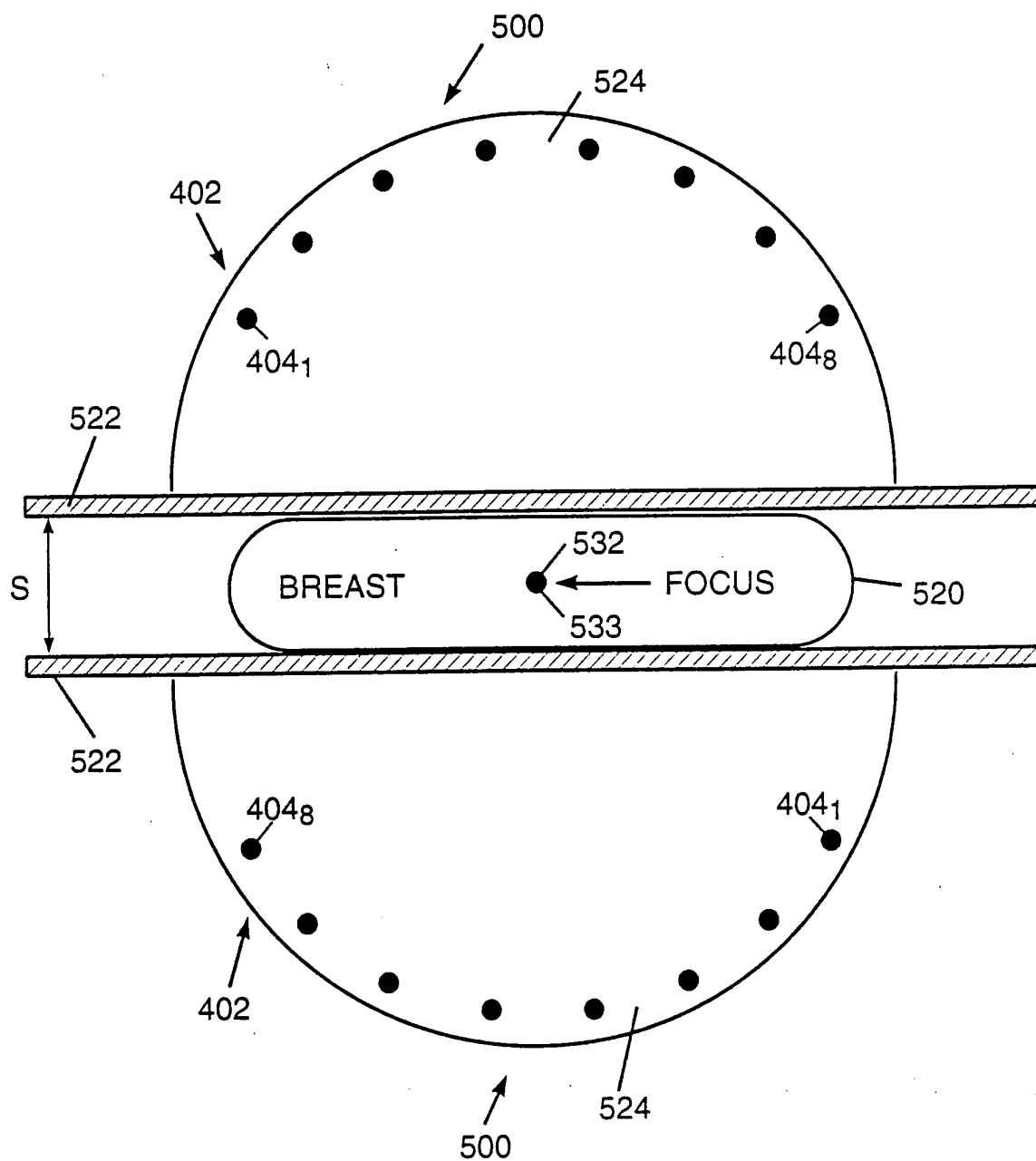


FIG. 64

64/69

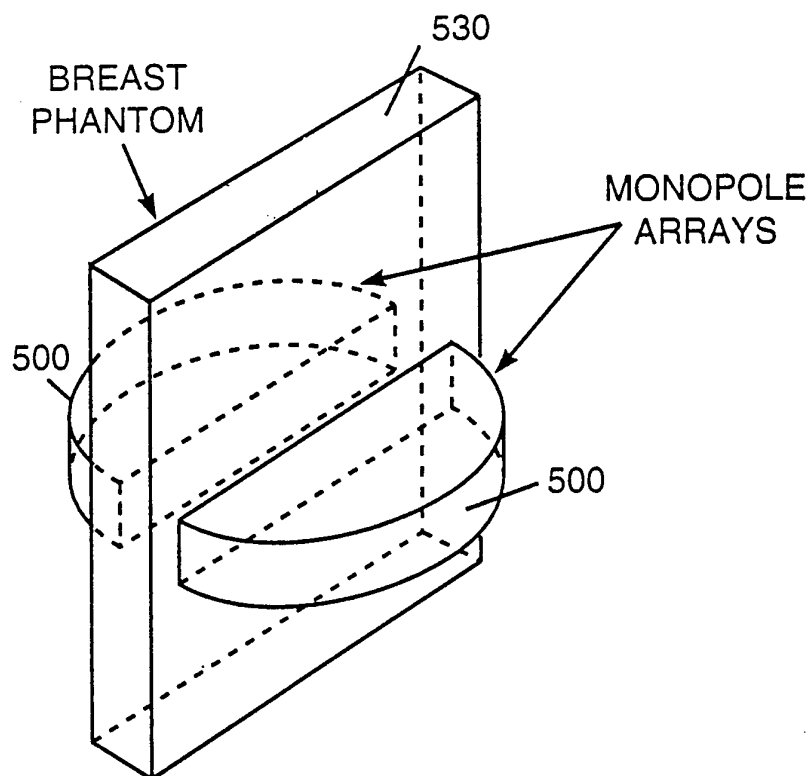


FIG. 65

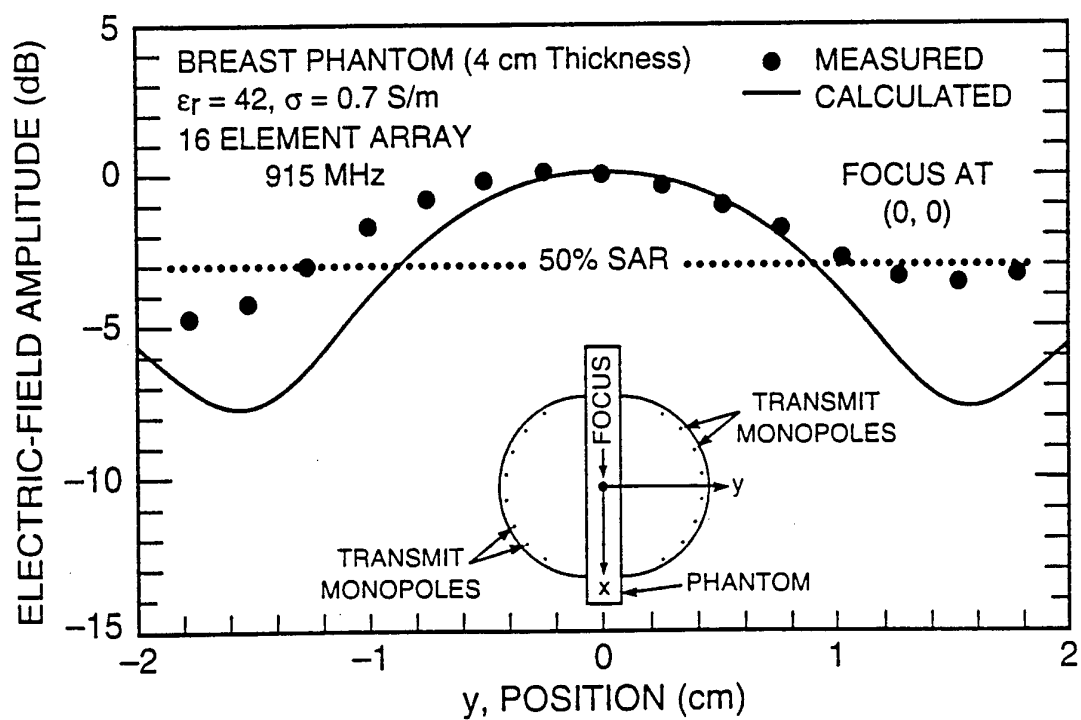


FIG. 67

65/69

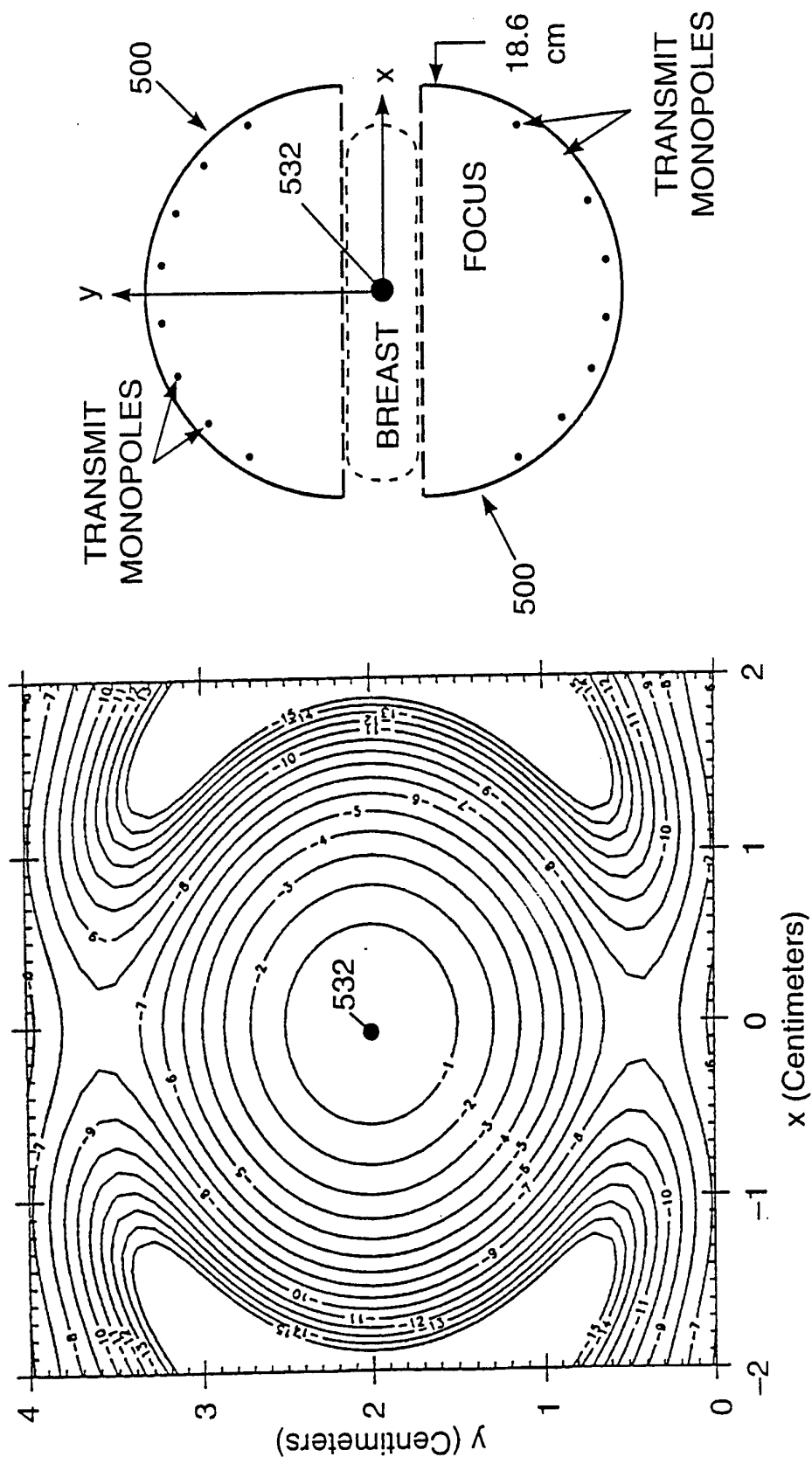


FIG. 66

66/69

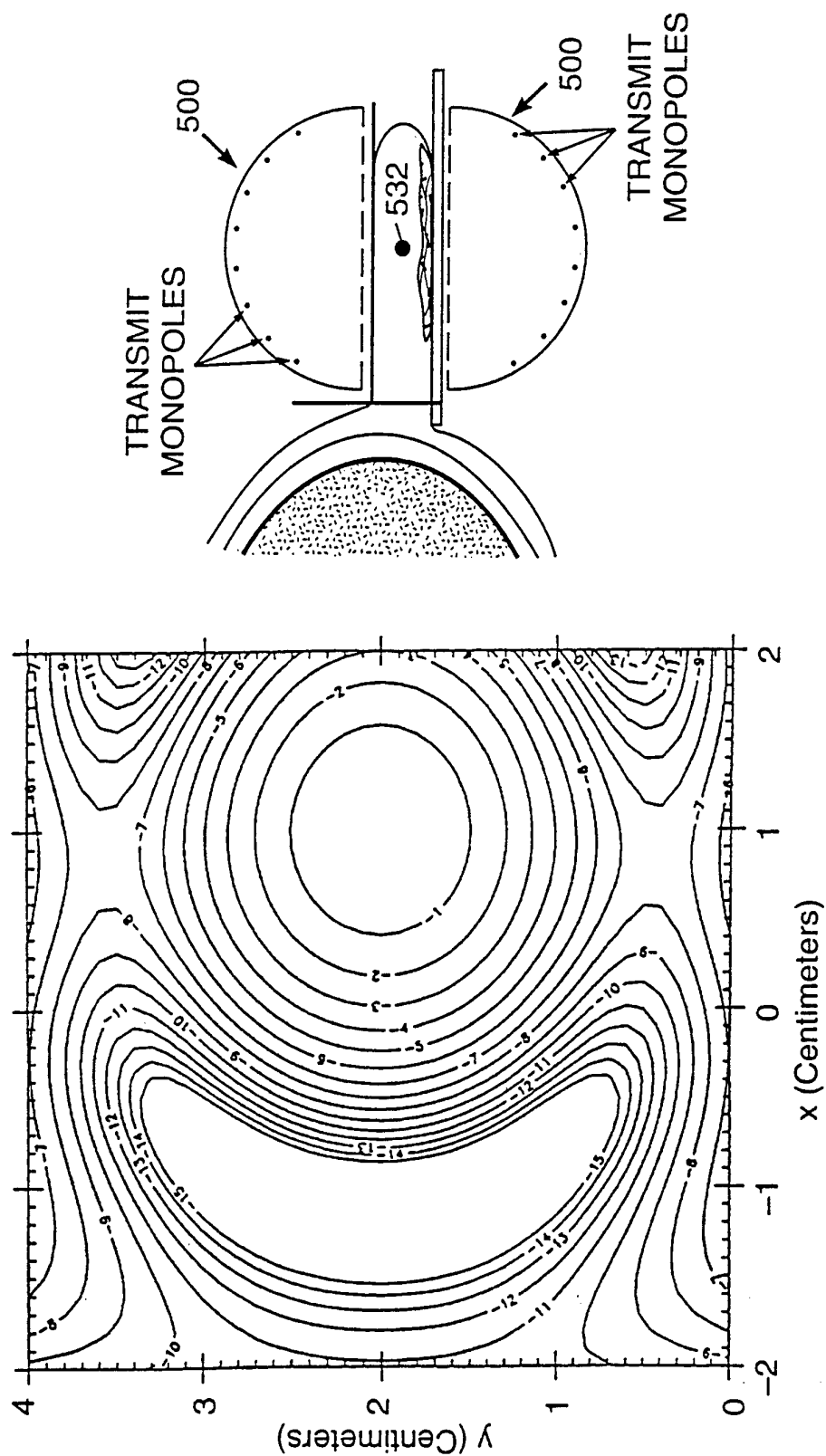


FIG. 68

67/69

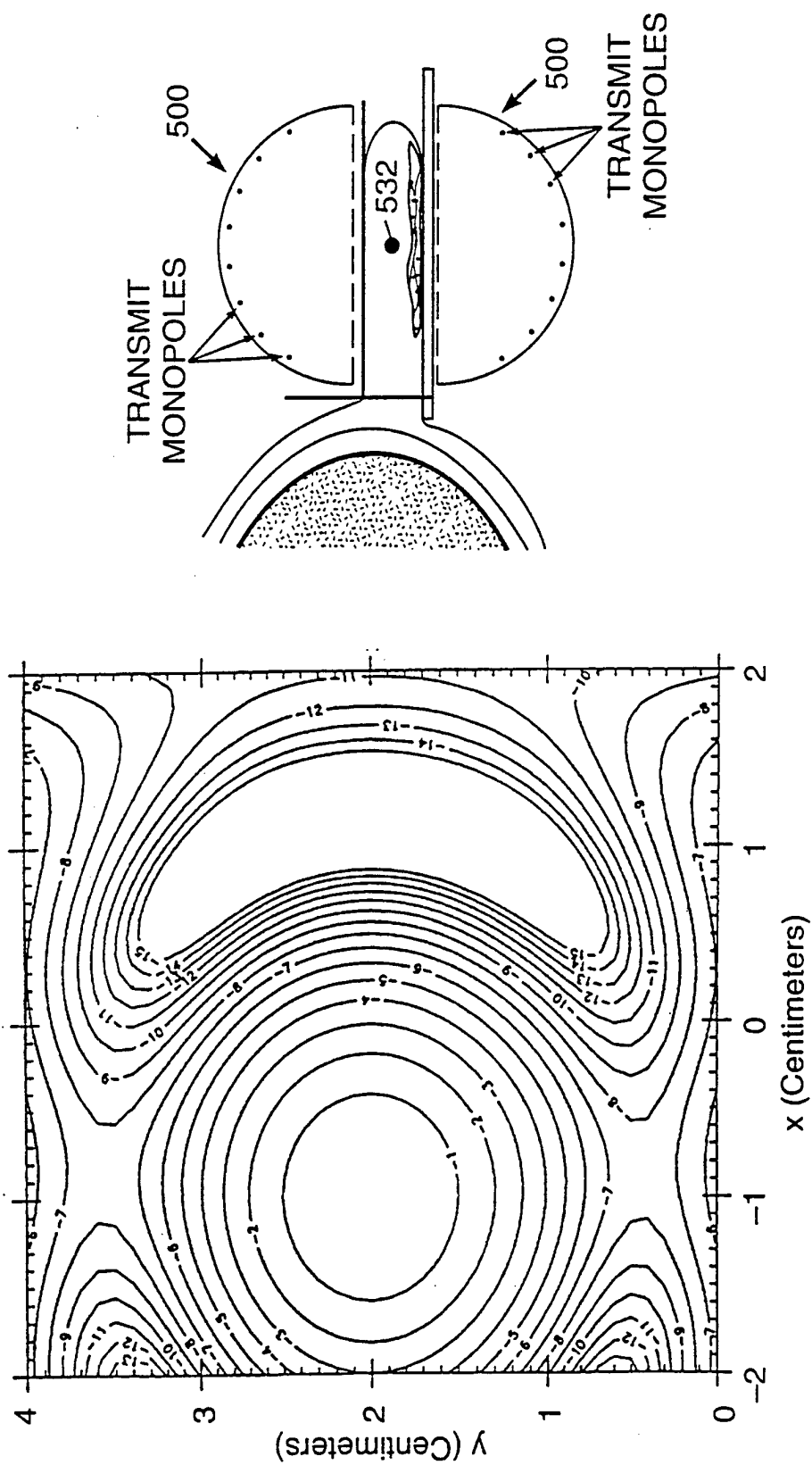


FIG. 69

68/69

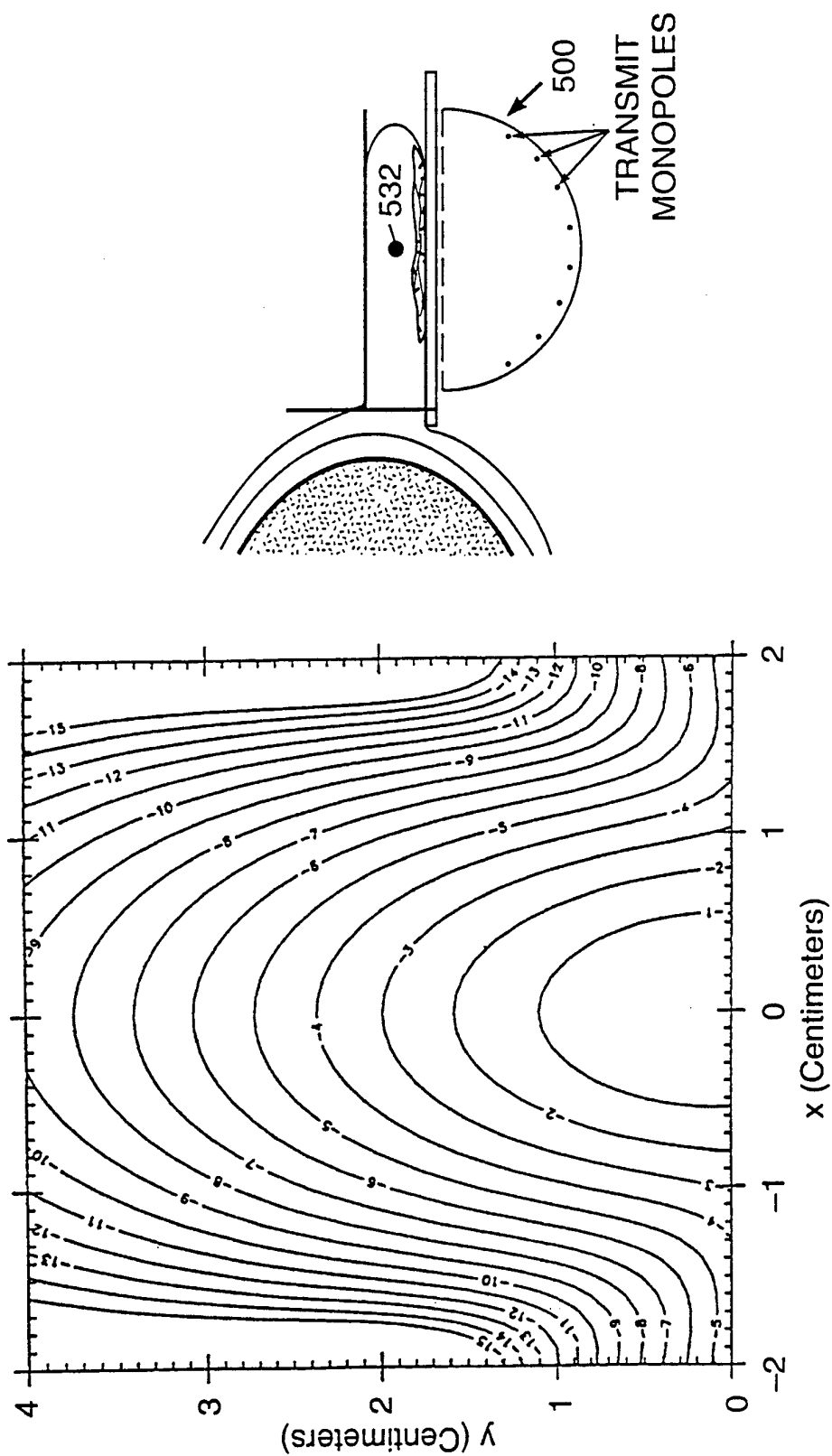


FIG. 70

69/69

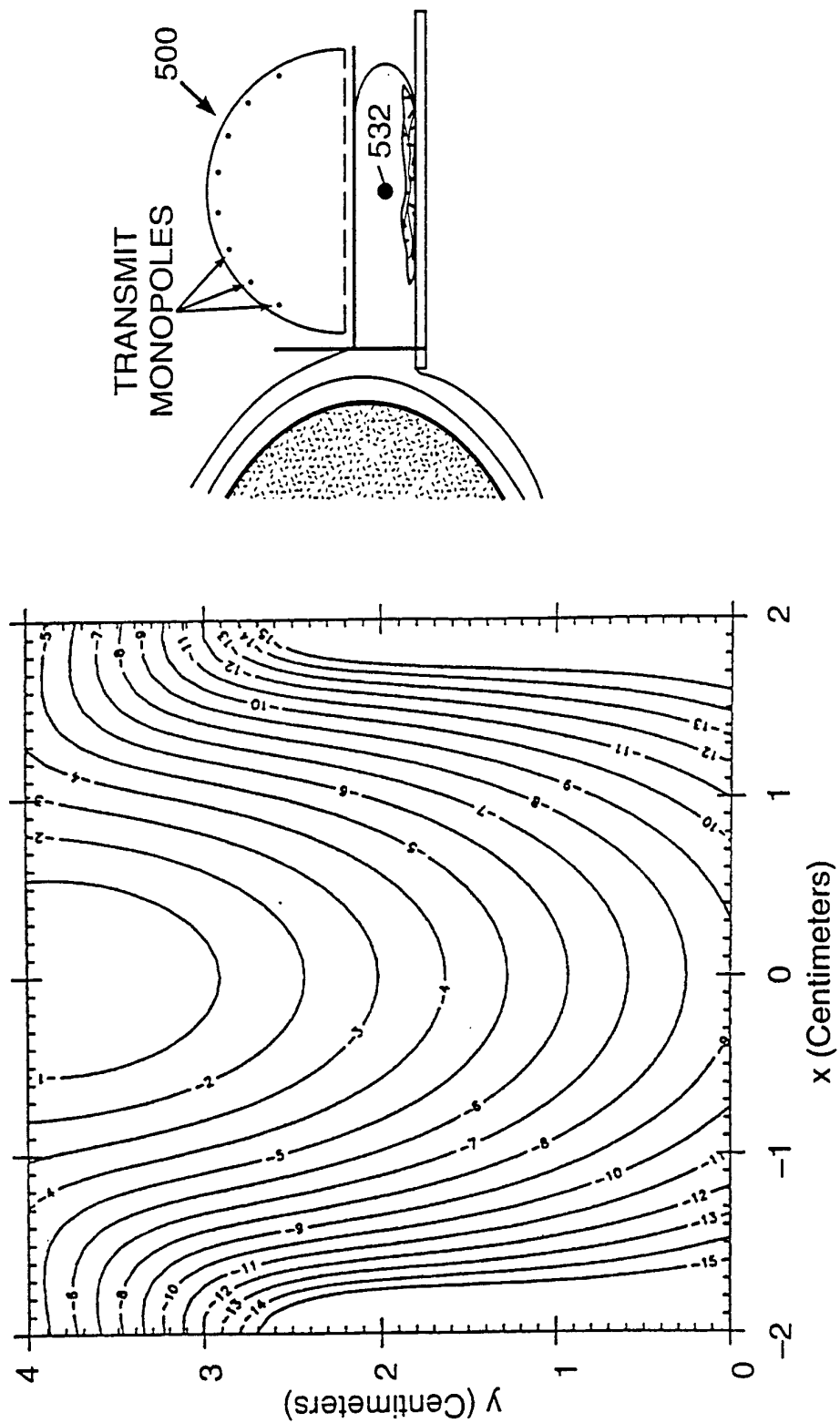


FIG. 71

INTERNATIONAL SEARCH REPORT

Intern: 1 Application No

PCT/US 94/13564

A. CLASSIFICATION OF SUBJECT MATTER
IPC 6 A61N5/02

According to International Patent Classification (IPC) or to both national classification and IPC

B. FIELDS SEARCHED

Minimum documentation searched (classification system followed by classification symbols)

IPC 6 A61N A61B

Documentation searched other than minimum documentation to the extent that such documents are included in the fields searched

Electronic data base consulted during the international search (name of data base and, where practical, search terms used)

C. DOCUMENTS CONSIDERED TO BE RELEVANT

Category *	Citation of document, with indication, where appropriate, of the relevant passages	Relevant to claim No.
A	WO,A,93 00132 (MASSACHUSET INSTITUTE OF TECHNOLOGY) 7 January 1993 see the whole document ---	1,2,12, 15,16, 26,29
A	WO,A,80 01461 (BSD MEDICAL CORPORATION) 24 July 1980 see the whole document ---	1,4,12, 15,18,26
A	US,A,4 397 314 (V. A. VAGUINE) 9 August 1983 see the whole document ---	1,12,13, 15,26, 27,29,30
A	EP,A,0 146 511 (CYTEX MEDICINTEKNIK AB) 26 June 1985 see the whole document ---	1,14,15, 28,29
	--- -/--	

☒ Further documents are listed in the continuation of box C.☒ Patent family members are listed in annex.

* Special categories of cited documents :

- "A" document defining the general state of the art which is not considered to be of particular relevance
- "E" earlier document but published on or after the international filing date
- "L" document which may throw doubts on priority claim(s) or which is cited to establish the publication date of another citation or other special reason (as specified)
- "O" document referring to an oral disclosure, use, exhibition or other means
- "P" document published prior to the international filing date but later than the priority date claimed

"T" later document published after the international filing date or priority date and not in conflict with the application but cited to understand the principle or theory underlying the invention

"X" document of particular relevance; the claimed invention cannot be considered novel or cannot be considered to involve an inventive step when the document is taken alone

"Y" document of particular relevance; the claimed invention cannot be considered to involve an inventive step when the document is combined with one or more other such documents, such combination being obvious to a person skilled in the art.

"&" document member of the same patent family

Date of the actual completion of the international search

27 March 1995

Date of mailing of the international search report

21.04.95

Name and mailing address of the ISA

European Patent Office, P.B. 5818 Patentlaan 2
NL - 2280 HV Rijswijk
Tel. (+31-70) 340-2040, Tx. 31 651 epo nl,
Fax: (+31-70) 340-3016

Authorized officer

Ferrigno, A

INTERNATIONAL SEARCH REPORT

Internat'l Application No
PCT/US 94/13564

C.(Continuation) DOCUMENTS CONSIDERED TO BE RELEVANT		
Category *	Citation of document, with indication, where appropriate, of the relevant passages	Relevant to claim No.
A	<p>US,A,4 884 580 (M. KIKUCHI ET AL.) 5 December 1989 see the whole document -----</p>	1,6,7,12

INTERNATIONAL SEARCH REPORT

Intern: al Application No

PCT/US 94/13564

Patent document cited in search report	Publication date	Patent family member(s)	Publication date
WO-A-9300132	07-01-93	US-A- 5251645	12-10-93
WO-A-8001461	24-07-80	US-A- 4271848	09-06-81
		EP-A- 0022824	28-01-81
		US-A- 4403618	13-09-83
US-A-4397314	09-08-83	NONE	
EP-A-0146511	26-06-85	CA-A- 1238723	28-06-88
		SE-A- 8306243	15-05-85
		US-A- 4727565	23-02-88
US-A-4884580	05-12-89	JP-A- 60190969	28-09-85
		JP-C- 1691308	27-08-92
		JP-B- 3056745	29-08-91
		JP-A- 60190970	28-09-85
		JP-B- 1014795	14-03-89
		JP-C- 1527781	30-10-89
		JP-A- 60190971	28-09-85
		JP-C- 1691309	27-08-92
		JP-B- 3056746	29-08-91
		JP-A- 60190972	28-09-85
		JP-C- 1691310	27-08-92
		JP-B- 3056747	29-08-91
		JP-A- 60190973	28-09-85